

The Impact of a Non-Ideal ILC Helical Undulator on the Photon Beam Parameters and Protection of the Undulator Wall Against Synchrotron Radiation

Dissertation
zur Erlangung des Doktorgrades
an der Fakultät für Mathematik, Informatik und Naturwissenschaften
Fachbereich Physik
der Universität Hamburg

vorgelegt von
Khaled Snad R Alharbi

Hamburg
2024

Gutachter/innen der Dissertation: Prof. Dr. Gudrid Moortgat-Pick
Dr. Sabine Riemann

Zusammensetzung der
Prüfungskommission: Prof. Dr. Arwen R. Pearson
Dr. Ayash Alrashdi
Prof. Dr. Gudrid Moortgat-Pick
Dr. Sabine Riemann
Prof. Dr. Wolfgang Hillert

Vorsitzende/r der Prüfungskommission: Prof. Dr. Arwen R. Pearson

Datum der Disputation: 23.01.2024

Vorsitzender des
Fach-Promotionsausschusses Physik: Prof. Dr. Markus Drescher

Leiter des Fachbereiches Physik: Prof. Dr. Wolfgang J. Parak

Dekan der Fakultät MIN: Prof. Dr.-Ing. Norbert Ritter

Abstract

The helical undulator-based positron source is considered for the International Linear Collider (ILC) baseline design. The scheme works by passing a multi-GeV (> 100 GeV) electron beam through a long superconducting helical undulator to produce a multi-MeV circularly polarized photon beam. It is then directed to a thin target to produce the electron-positron (e^-e^+) pair. The collected positron beam is longitudinally polarized.

Since photons in the undulator are produced with an opening angle, a part of the photon beam will hit the superconducting undulator wall. The acceptable level of the incident power at the wall is 1 W/m. Computer simulations have been performed in order to determine the incident power at the ILC superconducting undulator walls as well as the photon beam distribution and polarization at the target. For the ILC-250 parameters, the maximum incident power at the wall of the ideal undulator is 21 W/m. This thesis proposes a mask system for undulator protection to keep the incident power at the undulator wall below the acceptable level. The proposed mask has a 30 cm length and a 0.44 cm inner diameter. Three various material candidates for masks are studied: iron, copper, and tungsten. The incident power at the undulator walls due to the secondary particles is also studied. This system reduces the maximum incident power at the ideal undulator wall by approximately two orders of magnitude to ≈ 0.22 W/m for the ideal case of ILC-250. This thesis takes into account the non-ideal (realistic) helical undulators and considers all ILC energy options: the ILC-250, ILC-350, ILC-500, and GigaZ options. The realistic study is based on the measured B-fields of the helical undulator prototypes that were demonstrated at Daresbury Laboratory and Rutherford Appleton Laboratory. In the realistic case for ILC-250, the maximum incident power increases to 0.26 W/m with copper material for masks. The proposed mask system with any of the material candidates can keep the incident power at the undulator walls below the acceptable level for both ideal and realistic undulators and for both nominal and luminosity upgrade parameters of all ILC energy options. The incident power at the photon masks is studied. It is shown that the energy deposition, instantaneous temperature rise, and resulting stress in the masks are below the recommended limits even for long cyclic loads in the materials. The effects of placing masks along the undulator line on the power and polarization of the photon beam at the target plane are also studied. Studies show that placing masks will reduce the power of the photon beam by ≈ 8 % and slightly increase the photon beam polarization at the target plane for both ideal and realistic undulator cases. Compared with the photon beam polarization produced by the ideal undulators, the study shows that in the case of non-ideal undulators, the photon beam polarization decreases. Therefore, in order to achieve an efficient polarization upgrade of the positron beam using a photon collimator, the undulator parameters as well as those of the photon collimator should be re-optimized taking into account the realistic undulator as well as the updated OMD performance.

Kurzfassung

Die Standard-Positronenquelle für den International Linear Collider (ILC) basiert auf einem helischen Undulator. Sie funktioniert, indem ein Elektronenstrahl mit mehreren GeV (> 100 GeV) durch einen langen supraleitenden spiralförmigen Undulator geleitet wird, um einen Photonenstrahl mit mehreren MeV zu erzeugen. Der Photonenstrahl ist zirkular polarisiert. Er trifft auf ein dünnes Target, um Elektron-Positron-Paare (e^-e^+) zu erzeugen. Der resultierende Positronenstrahl ist longitudinal polarisiert.

Da Photonen im Undulator mit einem Öffnungswinkel erzeugt werden, trifft ein Teil des Photonenstrahls auf die supraleitende Wand des Undulators. Der akzeptable Wert der auf die Wand einfallenden Leistung beträgt 1 W/m. Es werden Computersimulationen durchgeführt, um die einfallende Leistung an den supraleitenden ILC-Undulatorwänden sowie die Photonenstrahlverteilung und die Polarisation am Target zu bestimmen. Für die ILC-250-Parameter beträgt die simulierte höchste einfallende Leistung an den Wänden eines idealen Undulators 21 W/m. Diese Arbeit schlägt ein Maskensystem als Undulator-Schutz vor, um die auf die Undulatorwand einfallende Leistung unter dem akzeptablen Niveau zu halten. Die vorgeschlagenen Masken haben eine Länge von 30 cm und einen inneren Durchmesser von 0.44 cm. Es werden drei verschiedene Material-Kandidaten für die Masken untersucht; Eisen, Kupfer und Wolfram. Die einfallende Leistung aufgrund der Sekundärteilchen wird ebenfalls untersucht. Dieses Maskensystem reduziert die maximale einfallende Leistung an der idealen Undulatorwand um etwa zwei Größenordnungen auf ca. 0.22 W/m. Diese Arbeit berücksichtigt die nicht-idealen (realistischen) helischen Undulatoren und betrachtet die ILC-Optionen: ILC-250, ILC-350, ILC-500 und GigaZ. Die Studie zum realistischen Undulator basiert auf dem gemessenen B-Feld der Undulator-Prototypen, die im Daresbury Laboratory und im Rutherford Appleton Laboratory gefertigt und getestet wurden. In diesem Fall erhöht sich die maximal einfallende Leistung bei Kupfer-Material für Masken auf 0.26 W/m. Das vorgeschlagene Maskensystem kann mit jedem Materialkandidaten die an den Undulatorwänden einfallende Leistung sowohl für ideale als auch für realistische Undulatoren unter das akzeptable Niveau reduzieren. Das gilt sowohl für die nominale Luminosität als auch für das Luminositäts-Upgrade der ILC-Optionen. Die auf die Photonen-Masken einfallende Leistung wird untersucht. Es zeigt sich, dass die Energiedeposition, der sofortige Temperaturanstieg und die daraus resultierende Spannung in den Masken unter den empfohlenen Grenzwerten für eine lange zyklische Belastung der Materialien liegen. Die Auswirkung der Platzierung von Masken entlang des Undulators auf die Leistung und Polarisation des Photonenstrahls in der Targetebene wird ebenfalls untersucht. Studien zeigen, dass die Leistung des Photonenstrahls sowohl im Fall eines idealen als auch realistischen Undulator um ca. 8% reduziert wird und die Photonenstrahlpolarisation in der Targetebene geringfügig zunimmt. Die Studie zeigt, dass im Fall eines nicht-idealen Undulators die Photonbeampolarisation im Vergleich zum idealen Undulator sinkt. Um das geplante Polarisations-Upgrade des Positronenstrahls zu erreichen, sollten sowohl die Undulatorparameter als auch die des Photon Collimators optimiert werden, dies unter Annahme eines realistischen Undulators und sobald das finale Design des OMD bekannt ist.

List of publications

I already published parts of the results presented in this thesis in the following articles:

1. Khaled Alharbi, Sabine Riemann, Gudrid Moortgat-Pick, and Ayash Alrashdi. "Energy deposition along the helical undulator at ILC-250 GeV." arXiv preprint arXiv: 1902.07755 (2019).
2. Khaled Alharbi, Sabine Riemann, Ayash Alrashdi, Gudrid Moortgat-Pick, and Andriy Ushakov. "Energy deposition due to secondary particles in the helical undulator wall at ILC-250 GeV." arXiv preprint arXiv:2001.08024 (2020).
3. Khaled Alharbi, Sabine Riemann, Ayash Alrashdi, Andriy Ushakov, Peter Sievers, and Gudrid Moortgat-Pick. "JACoW: Design of Photon Masks for the ILC Positron Source." JACoW IPAC 2021 (2021): 3834-3836.
4. Khaled Alharbi, Sabine Riemann, Ayash Alrashdi, Gudrid Moortgat-Pick, Andriy Ushakov, and Peter Sievers. "Photon Masks for the ILC Positron Source with 175 and 250 GeV Electron Drive Beam." arXiv preprint arXiv:2106.00074 (2021).
5. Khaled Alharbi, Sabine Riemann, Gudrid Moortgat-Pick, Ayash Alrashdi, and Andriy Ushakov. "Power Incident on the ILC Helical Undulator Wall." In European Physical Society Conference on High Energy Physics 2021, p. 867. 2021.

In reference 1, the synchrotron radiation power incident along the ideal helical undulator walls of ILC-250 GeV was simulated and studied. Section 8.2 and a part of section 8.3 present the results from this paper. Results in reference 1 show that the heat load at the undulator wall is too great and photon masks must be placed along the undulator line. Therefore, a possible photon mask geometry with a high photon absorption efficiency was proposed in reference 2. In addition, the PEDD at the photon masks and power incident at ideal undulator walls due to secondary particles were studied. The reference 5 studied the incident power at photon masks and undulator walls in the case of the non-ideal undulator. Results are shown in section 8.6, 8.3 and section 8.5. Photon mask effects on the photon beam parameters in the case of ideal and non-ideal helical are studied in reference 3 for ILC-250 and in reference 4 for both ILC-350 and ILC-500. Results are in chapter 9.

Contents

List of Figures	1
List of Tables	5
1 Introduction	7
2 Electron-Positron Colliders	9
2.1 Circular and Linear Colliders	9
2.2 Previous High-Energy Electron-Positron Colliders	10
2.2.1 The Large Electron-Positron Collider	10
2.2.2 The SLAC Linear Collider (SLC)	11
2.3 Future High-Energy Electron-Positron Collider Projects	12
2.3.1 International Linear Collider Project	12
2.3.2 Compact Linear Collider Project	14
2.3.3 FCC-ee Project	15
3 Positron Production	16
3.1 Generation of Positrons	16
3.2 Polarized Positron Beam	20
4 Positron Sources for High-Intensity Future Linear Colliders	22
4.1 Undulator-Based Positron Source	22
4.1.1 Layout of the ILC Helical Undulator Source	24
4.1.2 Parameters of the ILC Helical Undulator	25
4.2 Electron Driven Positron Source	26
4.3 Laser-Compton Positron Source	27
5 Synchrotron Radiation from a Helical Undulator	29
5.1 Synchrotron Radiation	29
5.2 Radiation from a Helical Undulator	31
5.2.1 Photon Number Spectrum	34
5.2.1.1 K Value	34
5.2.1.2 Undulator Period	36
5.2.1.3 Electron Beam Energy	37
5.2.2 Angular Power Distribution	37
5.2.3 Photon Beam Polarization	39
6 The ILC Helical Undulator	44
6.1 The ILC Helical Undulator Prototypes	44

6.2	The Structure of the ILC Undulator Line	45
6.3	Thesis Aims	47
7	Simulating Helical Undulator Photon Spectra	49
7.1	Simulation Methods	49
7.2	HUSR Simulation	51
7.2.1	Tracking an Electron Through an Ideal Field Map	53
7.2.2	Tracking an Electron Through a Realistic Field Map	53
7.3	Simulating the Photon Spectrum	60
7.4	Simulating the Photon Beam Polarization	60
8	Power Incident into the Undulator Vessel	66
8.1	Calculating the Incident Synchrotron Radiation	67
8.2	Incident Power at the ILC Undulator Vessel	68
8.3	Mask System for the Undulator Protection	69
8.3.1	Basic Photon Mask Layout	70
8.3.2	Incident Power at Undulator Walls with Ideal Photon Masks	71
8.3.3	Incident Power at Photon Masks	73
8.4	Material Candidates for Photon Masks	75
8.5	Power Deposition in Realistic Photon Masks	75
8.6	Heat Load at the Photon Masks	81
8.7	Distribution of Secondary Particles at the Undulator Walls	83
8.8	Result	88
8.8.1	Incident Power at Masks	88
8.8.2	Heat Load at Mask Material Candidates	88
8.8.3	Incident Power at Ideal and Realistic Undulator Walls	89
8.9	Power Deposition in Photon Masks of the ILC-350 and ILC-500	93
8.9.1	Result	93
8.10	The Deposited Power at the Undulator Walls in Case of the ILC Luminosity upgrade	98
9	The ILC Photon Beam Power and Polarization	99
9.1	Photon Beam Polarization	99
9.2	The Photon Beam and Polarization Distribution	100
9.3	The Effect of Photon Masks on Photon Beam Power and Polarization	104
9.3.1	$E_{cm} = 250$ GeV Option	104
9.3.2	$E_{cm} = 350$ GeV and 500 GeV Options	104
9.4	HUSR Photon Collimator	105
9.5	Result	106
9.5.1	The Effect of Photon Masks on Photon Beam Parameters	106
9.5.1.1	$E_{cm} = 250$ GeV Option	106
9.5.1.2	$E_{cm} = 350$ GeV and 500 GeV Options	106
9.5.2	The Effect of the Photon Collimator on Photon Beam Parameters	110
9.6	Polarization Upgrade of ILC-500	114
10	Synchrotron Radiation Power Incident on the Undulator Walls of the ILC GigaZ Option	117
10.1	Incident Power at Undulator Walls of the GigaZ Option	117

11 Summary	121
A Electron-Positron Collider	124
A.1 Positron Production	124
A.1.1 Electromagnetic Cascades	124
A.1.1.1 Photon Interactions with Matter	127
A.1.1.2 Electron Interactions	129
A.2 Positron Polarization	132
A.2.1 Polarization	132
A.2.2 Parameterization of Polarization	132
A.2.2.1 The Jones Vector	132
A.2.3 Stokes Parameters from Jones Vector	133
A.2.4 Transfer Matrix	134
A.3 Bremsstrahlung Radiation and Pair Production	135
A.3.1 Polarized Bremsstrahlung	135
A.3.1.1 Polarization Transfer from a Lepton (an Electron or Positron) to a Photon	135
A.3.2 Pair Production	136
A.3.2.1 Polarization Transfer from the Photon to two Leptons (e^- and e^+)	137
A.3.2.2 Transferring the Circular Polarization from the Photon to the Longitudinal Polarization for the two Leptons (e^- and e^+)	138
A.3.2.3 Simulating the Polarization Transfer	138
B The ILC Photon Beam Power and Polarization	140
B.1 The Effect of the Photon Collimator on Photon Beam Parameters	140
Bibliography	144

List of Figures

2.1	Schematic layout of the LEP	10
2.2	Schematic layout of the SLC	11
2.3	Schematic layout of the ILC	13
2.4	Schematic layout of the CLIC	14
3.1	Feynman graphs for the pair production	16
3.2	Cross section of a photon in titanium	17
3.3	The e^+ yield as a function of the target thickness	18
3.4	Feynman graph for the bremsstrahlung process	18
3.5	The longitudinal polarization of the lepton beam	20
3.6	The longitudinal polarization of positron beam	21
4.1	Schematic of a permanent magnet planar undulator	23
4.2	Principle of producing a polarized e^+ beam by a helical undulator	23
4.3	Layout of the ILC positron source	24
4.4	Diagram of a wire wound in double helix	25
4.5	Schematic of the ILC E-driven positron source	27
4.6	Principle of laser-Compton positron source	28
5.1	Photon number spectrum for the first five harmonics	35
5.2	Photon spectrum created by a helical undulator with different K	36
5.3	Photon spectrum created by a helical undulator with different λ_u	37
5.4	Photon spectrum created by a undulator with different E_e	38
5.5	Angular power distribution in the first five harmonics	38
5.6	Angular power distribution produced by a helical undulator	39
5.7	Photon beam spectrum and polarization created by a helical undulator	41
5.8	Spectrum and circular polarization of the photon beam	42
5.9	Photon beam polarization produced by a undulator with different K	43

6.1	The four short undulator prototypes	45
6.2	K value per period measured from undulator prototypes.	46
6.3	Schematic layout of the ILC undulator line	46
7.1	Comparison between three codes	51
7.2	flowchart shows the steps of the process in the HUSR	52
7.3	Ideal magnetic field of the helical undulator	53
7.4	Displacement of a 125 GeV electron through first 3 periods of the undulator	54
7.5	Realistic magnetic field of the undulator	55
7.6	K value with errors along the realistic undulator	56
7.7	Trajectory and deviation of a 125 GeV electron traveling through a undulator	57
7.8	Trajectory and deviation a 175 GeV electron traveling through a undulator	58
7.9	Trajectory and deviation a 250 GeV electron traveling through a undulator	59
7.10	Deviation of a 125 GeV electron beam traveling through different undulator lengths	61
7.11	Deviation of a 125 GeV electron beam through the whole ILC undulator length	62
7.12	Photon spectrum	63
7.13	Ideal spectrum and polarization of the photon beam	64
7.14	Ideal distribution of the photon beam and polarization	65
8.1	Incident power per meter in the undulator walls	68
8.2	The incident power per meter along the undulator walls simulated by HUSR	69
8.3	Schematic layout of the undulator line with a photon mask	69
8.4	A longitudinal section of the photon mask	70
8.5	A drawing of the photon mask cross-section along the z direction	71
8.6	Incident power at the undulator walls due the primary photons	72
8.7	Power incident on photon masks	73
8.8	Average incident photon energy on photon masks	73
8.9	The deposited energy along the Mask-21	76
8.10	The deposited energy along the Mask-22	76
8.11	The maximum deposited energy along Mask-21	77
8.12	The maximum deposited energy along Mask-22	78
8.13	PEDD along Z-direction of Mask-22 for both ILC-250 ideal and realistic undulators	79
8.14	The deposited energy along Z-direction of the realistic Fe , Cu and W Mask-22	82
8.15	A drawing of all possible directions of secondary particles around the photon mask	83
8.16	The density of secondary particles along Mask-21 for both ideal and realistic undulators of the ILC-250	85

8.17	The density of secondary particles along Mask-22 for both ideal and realistic undulators of the ILC-250	86
8.18	Spectrum of photons escaping Fe and Cu photon masks to the undulator	87
8.19	Incident power at undulator walls by the full active ILC-250 ideal undulator length .	90
8.20	Incident power at undulator walls by the full active ILC-250 realistic length	91
8.21	The deposited energy along Mask-22 for the ILC-350	94
8.22	The deposited energy along Mask-22 for the ILC-500	94
8.23	The maximum deposited energy along Mask-22 for both ideal and realistic undulators of the ILC-350	95
8.24	The maximum deposited energy along Mask-22 for both ideal and realistic undulators of the ILC-500	96
9.1	Ideal (realistic) distribution of the photon number and photon beam polarization . .	101
9.2	Ideal (realistic) distributions of the photons and polarization produced by the full active length of ILC-250 undulator	102
9.3	Ideal (Realistic) distributions of the photons and polarization produced by the full active length of ILC-250 undulator	103
9.4	Ideal (Realistic) spectrum and circular polarization of the photon beam.	107
9.5	Ideal (Realistic) spectrum and circular polarization of the photon beam of ILC-350 .	108
9.6	Ideal (Realistic) spectrum (and circular polarization) of the photon beam of ILC-500	109
9.7	Ideal (Realistic) spectrum and circular polarization of the photon beam of ILC-250 undulator	110
9.8	Ideal (Realistic) spectrum and circular polarization of the photon beam of ILC-350 undulator	111
9.9	Ideal (Realistic) spectrum and circular polarization of the photon beam of ILC-500 .	111
9.10	Photon beam spectrum and polarization produced by 253 GeV electron beam	114
9.11	Photon beam spectrum and polarization produced by 253 GeV electron beam	115
10.1	Synchrotron radiation power incident per meter on the GigaZ undulator walls	119
10.2	Synchrotron radiation power incident per meter on the undulator walls of the GigaZ and ILC-250	120
A.1	Electromagnetic shower	125
A.2	Mass radiation stopping power for electrons in tungsten	125
A.3	Feynman graphs for pair production and bremsstrahlung	126
A.4	Cross section of photon in titanium	128
A.5	Schematic of the electron shower passing a material	131

A.6	The electric field vector in the x-y plan	133
A.7	The energy and polarization of positron beam produced by photon beam	139
B.1	Ideal (Realistic) spectrum and circular polarization of the photon beam produced by ILC-250 undulators using different photon collimator apertures	141
B.2	Ideal (Realistic) spectrum and circular polarization of the photon beam produced by ILC-350 undulators using different photon collimator apertures	142
B.3	Ideal (Realistic) spectrum and circular polarization of the photon beam produced by ILC-500 undulators using different photon collimator apertures	143

List of Tables

4.1	Nominal beam parameters of the ILC TDR	26
5.1	N_γ , E_{ave}^γ , P_γ of the photon beam with different θ_{Max}	42
6.1	The parameters of the ILC helical undulator structure line	47
7.1	Undulator parameters used in the comparison between FluxCalc, HUSR and SPECTRA	50
8.1	Incident power, average incident photon energy and incident photon number at masks for both ideal and realistic ILC-250 undulators	74
8.2	Properties of the material candidates for masks	75
8.3	E_{ave}^γ , P_{mask} , N_{mask}^γ , E_{max} , PEDD at Mask-21 and Mask-22	80
8.4	Y_m , α_h , and F_{tu} of the material candidates	82
8.5	P_{wall} into the first meter of the undulator wall downstream Mask-20, Mask-21 and Mask-22 for both ideal and realistic ILC-250 undulators	92
8.6	E_{ave}^γ , P_{mask} , N_{mask}^γ , E_{max} , PEDD at Mask-22 for the ILC-350 and ILC-500	97
8.7	ILC undulator parameters	98
8.8	The deposited power at the first meter of the realistic undulator module downstream the Mask-21 in the ILC-250	98
9.1	P_{target} , E_{ave}^γ and P_γ of the photon beam at the ILC-250 target plane	101
9.2	P_{target} , E_{ave}^γ and P_γ of the photon beam at the ILC-250 target plane without and with masks	106
9.3	P_{target} , E_{ave}^γ and P_γ of the photon beam at target plane for ideal (realistic) ILC-350 undulators without and with masks	108
9.4	P_{target} , E_{ave}^γ and P_γ of the photon beam at target plane for ideal (realistic) ILC-500 undulators without and with masks	109
9.5	P_{target} , E_{ave}^γ and P_γ of the photon beam at target plane with different photon collimator radii	112

9.6	P_{target} , E_{ave}^γ and P_γ of the photon beam at target plane with small photon collimator radii	113
9.7	E_{1st} , E_{ave} , P_{target} and P_γ of the photon beam at the target plane produced by a 253 GeV electron beam with different K values	115
10.1	The proposed parameters of the RF system for alternating operation of 125 GeV and 45.6 GeV for the GigaZ option	118

Chapter 1

Introduction

The Standard Model (SM) of the particle physics represents our current knowledge of particles and their interactions. It successfully describes the electromagnetic, weak, and strong interactions of elementary particles. The theoretical framework was already proposed at the beginning of the 1970s. The discovery of particles proposed by the SM is currently in concordance with its predictions. With the discovery of one Higgs boson in 2012, the exploration of one decisive basic component of the SM was started. The Higgs boson has often been considered as the last missing piece in the SM, but with the discovery of a Higgs-like particle, a new chapter started, and many questions had to be answered. The phenomenon of the interaction of elementary particles can be studied with high precision in particle collisions at high energies. In order to consolidate and go beyond the current knowledge, new particle colliders will be necessary that allow the observation of processes at desired higher energies.

So far, the Large Hadron Collider (LHC) at CERN, which has been operating since 2011, operates with the highest centre-of-mass energy ever ($E_{cm} \approx 14$ TeV). It uses two proton beams for the collision. Currently, the LHC is upgraded and will allow measurements with even higher precision. Since it is a proton-proton collider, and protons are composite particles consisting of quarks and gluons, not all phenomena can be studied at the LHC with the desired precision.

Running an electron-positron (e^-e^+) collider at very high energies would provide such high precision and perfectly complement the knowledge of particle interactions. Several e^-e^+ collider projects are currently under discussion. The most promising linear e^-e^+ collider projects are the International Linear Collider (ILC) and the Compact Linear Collider (CLIC). They allow us to study particle interactions in collisions of e^- and e^+ beams over a large and tunable energy range. It is a big advantage of e^-e^+ colliders that the parameters of the initial states are precisely known, so that the observed processes can be analyzed with high precision. However, from a technical point of view, it is still a challenge to design and build colliders that smash electrons and positrons with

a high colliding rate at very high centre-of-mass energies from 250 GeV to up to 1 TeV and even higher, as in CLIC.

This thesis focuses on the ILC design and, in particular, on the production of an intensely polarized positron beam using a helical undulator. The big advantage of using the helical undulator-based positron source is to get a precisely polarized positron beam, which enhances physics studies. More details about the benefits of polarized positron beams can be found in the references [1, 2, 3]. The helical undulator-based positron source method works as follows: the helical undulator is passed by the high-energy electron beam in order to produce a circularly polarized photon beam; the photon beam generates an even polarized positron beam in a thin conversion target via the pair production process. The spectrum, distribution, power, and polarization of the photon beam are studied at the ILC target plane for an undulator with an ideal magnetic field as well as an undulator with a realistic field distribution. An important task is the protection of the undulator wall against synchrotron radiation. All studies are performed for three stages of ILC operations: ILC-250, ILC-350, and ILC-500, with e^-e^+ collisions at energies of 250 GeV, 350 GeV, and 500 GeV, respectively. In addition, the power incident on the undulator walls of the GigaZ option is studied.

The thesis is organized as follows: in chapter 2 an overview of previous and future e^-e^+ collider projects is given. In the nineties of the last century, the e^-e^+ LEP and SLC colliders were operated and performed measurements of the SM parameters with very high precision. To extend such measurements to even higher energies and with even higher precision, machines that allow a high rate of collisions are required. The advantages and limitations of future projects are briefly discussed. In chapter 3, the generation of positrons is introduced, and chapter 4 presents e^+ source options for future ILC and CLIC projects. For the ILC, a helical undulator-based scheme for the positron production is favored. Therefore, in chapter 5, the physics of the helical undulator is presented, and chapter 6 introduces in detail the helical undulator as a photon source to generate positrons at the ILC. In chapter 7, the HUSR code, which is used to simulate the photon spectrum for the helical undulator, is introduced. Furthermore, the methods to obtain the power incident on the undulator walls and the integration of masks into the undulator line to protect the walls are presented. In chapter 8, the results are discussed: the power deposition in the wall and in the photon masks, and the efficiency of different mask materials to stop the primary photons and secondary particles. In chapter 9, the distributions of the photon beam polarization and power at the target plane are analyzed. In addition, the possibility of a polarization upgrade at the ILC-500 is discussed. In chapter 10, the power incident on the undulator walls of the GigaZ option is studied. Chapter 11 summarizes the results.

Chapter 2

Electron-Positron Colliders

Electron-positron (e^-e^+) colliders have played a really important role in the development of the Standard Model (SM). The history of e^-e^+ colliders started from the beginning of the 1960's, when the first ever e^-e^+ collider project, Anello di Accumulazione (AdA), was proposed by the Austrian physicist Bruno Touschek and built at the Frascati National Laboratory (LNF) in Italy [4]. Following the AdA, many e^-e^+ collider projects were built over the last 60 years, and each one of these colliders was built in order to answer specific opened questions. In addition, there will be future e^-e^+ projects that are currently under discussion.

This chapter will briefly introduce some important previous and future high-energy e^-e^+ collider projects, whether they are linear or circular colliders.

2.1 Circular and Linear Colliders

In a circular collider, beams are accelerated, and the magnetic field is used to bend particles into a circular orbit. In contrast, beams in the linear accelerator (linac) are accelerated in a straight line. One of the most significant disadvantages of circular accelerators compared with linear ones is the emitted Synchrotron Radiation (SR), first recorded in 1965 by Maury Tigner [5]. So, when charged particles pass through a circular path, they emit the SR. As a consequence, they lose energy. The energy loss per turn is proportional to $\frac{E^4}{m_0^4} \frac{1}{r}$, where r is the effective bending radius of the collider, and m_0 is the rest mass of the particle. The Large Electron Positron Collider (LEP), which was a circular collider, reached a centre-of-mass energy of 208 GeV. Due to synchrotron radiation, running LEP at higher beam energies was inefficient. Therefore, to operate e^-e^+ circular colliders at high energies, the radius of the circular colliders must be very large, which is a decisive cost factor. As an alternative, linear colliders are used to achieve high energies. By using high accelerating gradients, linear colliders with reasonable tunnel lengths can reach the desired energy. It is more difficult for

linear colliders to achieve high luminosity, since the beams in linear colliders are dumped after the collision, while the beams in circular colliders are used repeatedly. To overcome this issue, extremely small beam sizes are required in linear colliders, which is also a challenge.

2.2 Previous High-Energy Electron-Positron Colliders

In this section, two important previous high-energy electron-positron (e^-e^+) colliders are briefly introduced, including the large electron-positron collider (LEP) and the SLAC Linear Collider (SLC).

2.2.1 The Large Electron-Positron Collider

The Large Electron Positron (e^-e^+) (LEP) collider in CERN, Geneva, began operation in the summer of 1989 and stopped running in 2000 [6]. The LEP was a circular collider with a circumference of 27 km. So far, it is the largest circular e^-e^+ collider ever built. Figure 2.1 shows the schematic view of the LEP collider.

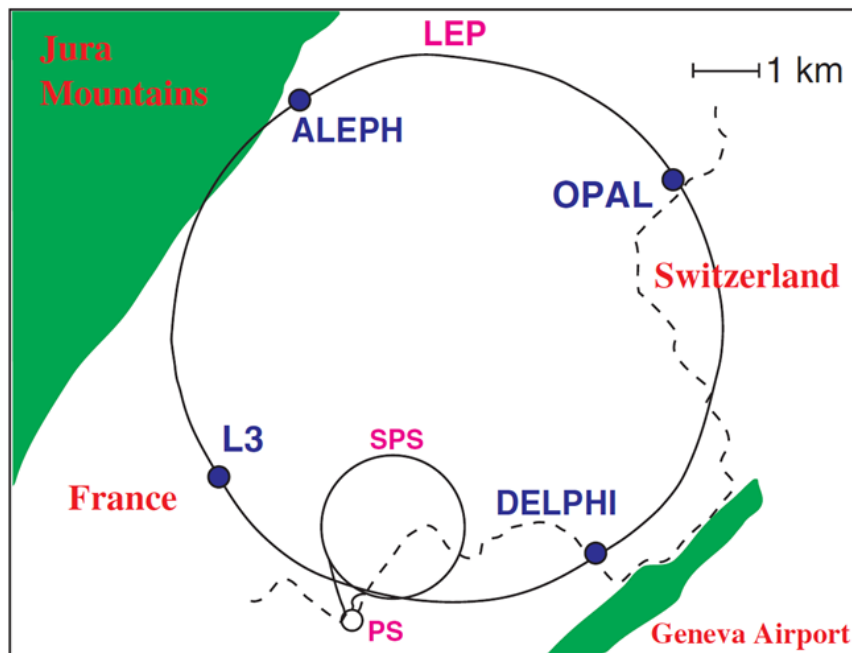


Figure 2.1: Schematic layout of the LEP collider showing the location of the four experiments ALEPH, DELPHI, L3 and OPAL [6].

The LEP was designed to study with high precision measurements of both Z and W bosons and also to search for new particles. From 1989 to 1995, the LEP was running on the Z boson resonance. From 1996 to 2000, operators worked hard to significantly increase the energy and luminosity of the

LEP. The centre-of-mass energy of the LEP was increased to 161 GeV in order to produce the pairs of W bosons. In several steps, the LEP reached the maximum centre-of-mass energy, which was 209 GeV. Due to the emission of the SR, it was highly inefficient to operate it at higher energies. More details about LEP can be found in [6].

2.2.2 The SLAC Linear Collider (SLC)

The Stanford Linear Collider (SLC), which was the first e^-e^+ linear collider, was designed and constructed during the 1980s and started running in 1989 [7]. It was designed to operate, complementary to LEP, with a centre-of-mass energy of 91 GeV and also to demonstrate linear collider feasibility. Figure 2.2 shows the schematic view of the SLC.

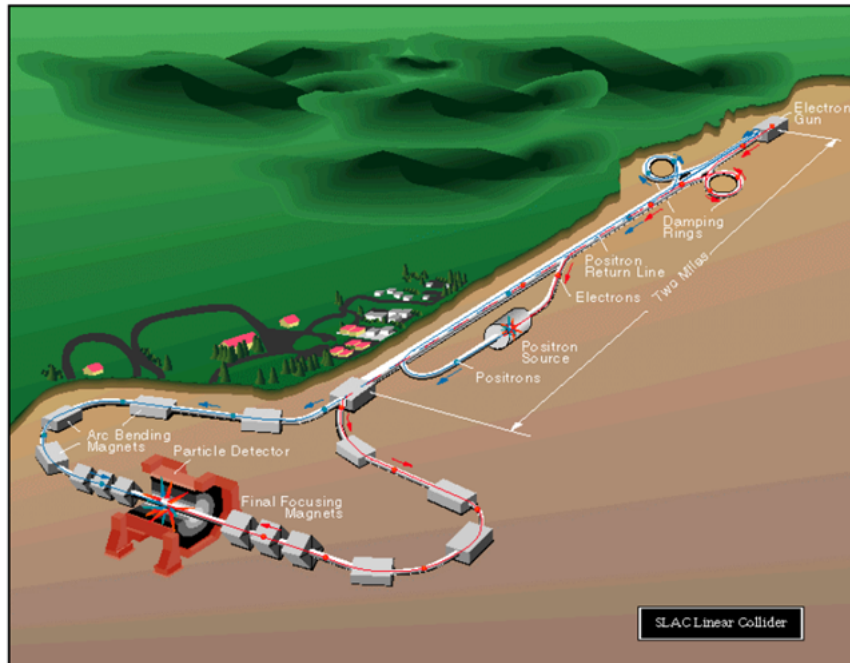


Figure 2.2: Schematic layout of the SLC collider [6] .

Both e^- and e^+ beams were accelerated in linacs to the final centre-of-mass energy of 93 GeV (46.5 GeV for each). After that, the positron beam and the longitudinal polarized electron beam were sent to the interaction point (IP) for collision, and after the collision, the beams were dumped. Since the e^- beam of SLC was polarized, using only 5×10^5 Z bosons in SLC allowed measurements of certain SM parameters with a precision that was reached by LEP with at least 16×10^6 Z bosons. More details about SLC can be found in [8, 9].

SLC provided an essential experience to design the "second" generation of the e^-e^+ linear collider, such as the future ILC and CLIC projects. The future e^-e^+ colliders are planned to be designed not only with higher centre-of-mass energies but also with higher luminosity.

2.3 Future High-Energy Electron-Positron Collider Projects

The future high-energy e^-e^+ colliders should work with a centre-of-mass energy above 200 GeV to give comprehensive information to the LHC results. There are several e^-e^+ collider projects under discussion. Two terascale e^-e^+ linear colliders are being proposed: the International Linear Collider (ILC) and the Compact Linear Collider (CLIC). Both are still unfunded projects, but they are the focus of extensive global research and development. The most mature is the ILC, compared with the CLIC, which has the greatest energy reach. The initial stage of the ILC is at a centre-of-mass energy of 0.25 TeV, and the later stages could reach a centre-of-mass energy of 0.35 TeV, 0.5 TeV, and maybe up to 1 TeV. In contrast, the centre-of-mass energy range proposed in the CLIC is planned from 0.38 TeV up to 3 TeV.

In addition, there are proposed circular collider projects, such as the Future Circular Collider (FCC). The ultimate goal of the FCC is proton–proton collisions (FCC-hh) at 100 TeV in a ring of about 100 km circumference. A first step could be to operate in the tunnel an e^-e^+ collider with very high luminosity at energies between 90 GeV and 400 GeV (FCC-ee). Another project is the Chinese Electron Positron Collider (CEPC). It is almost similar to the FCC-ee, which is on advanced steps compared with the CEPC. More details about CEPC can be found in [10]. The current situation of the ILC, CLIC, and FCC-ee is different and is introduced here.

2.3.1 International Linear Collider Project

The international linear collider (ILC) project, which is under consideration to be hosted in Japan, has been under development since more than 20 years. It is an e^- and e^+ collider. It is designed for precise measurements of Higgs boson and for studying exciting processes of the Standard Model and beyond [11]. Figure 2.3 shows the schematic layout of the ILC baseline configuration. The first stage of the ILC is to collide electrons and positrons at a centre-of-mass energy of 250 GeV, with the possibility to upgrade up to 1000 GeV (1 TeV). Also, it is possible to run the ILC at the GigaZ option [12]. The ILC consists of two sources for electrons and positrons, and two separated linacs for electrons and positrons, and two separated damping rings for electrons and positrons, and one interaction point (IP). In the ILC, a photocathode DC gun is used to produce an electron beam with polarization of more than 80% and energy of 0.2 MeV. This beam is accelerated up to 5 GeV before being sent to the electron damping ring (DR). There are two possible methods that can be used to produce positrons in the ILC including an undulator-based positron source and an electron driven (E-driven) source as will be discussed with more details later in chapter 4. In both

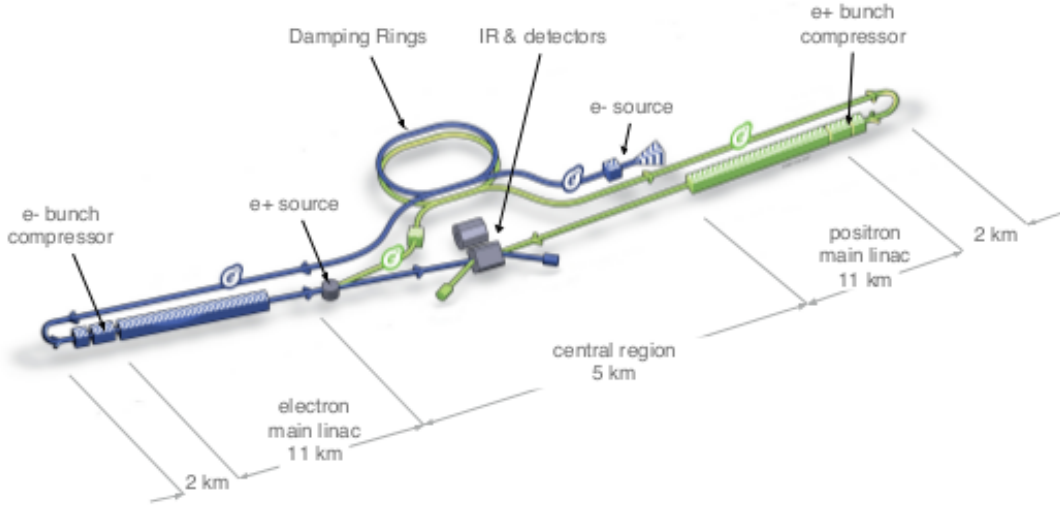


Figure 2.3: Schematic layout of the international linear collider baseline configuration [11].

methods, produced positrons will be captured and accelerated up to 5 GeV before being sent to the positron DR. The ILC has two separated main linacs, one is for the electron beam and the other is for the positron beam. The electron and positron beams will be accelerated in two separated superconducting linacs up to the required energies before being directed to the interaction point (IP) for collision. The ILC 9-cells cavity, which was developed for TESLA and is currently used for the XFEL, works at a resonant frequency of 1.3 GHz and the average gradient in the ILC can reach 35 MV/m. The ILC time structure is 0.727 millisecond bunch trains at 5 Hz. As mentioned, this project is currently under consideration as the future global project in particle physics. Over many years, the physics user community has discussed and updated the ILC parameters. The physics parameters were set by physics requirements first in 2003, updated in 2006, and then in 2013 when the Technical Design Report (TDR) was published [11]. The last updated parameters were presented in 2019 [13]. In the TDR, the nominal parameters of the ILC Linac beam were 500 GeV centre-of-mass-energy (possibility upgraded to a 1 TeV). In 2012, physicists at the Large Hadron Collider (LHC) at CERN discovered Higgs boson [14]. Following this discovery, the ILC has chosen 250 GeV centre-of-mass energy as the first stage. The later stages are to upgrade the centre-of-mass energy to 350 GeV for studying the threshold of top-pair production and to 500 GeV for studying exciting processes of the Standard Model and beyond. It is also considered to run the ILC at the GigaZ and to improve the precision of the results of LEP and SLC by at least one order of magnitude (see chapter 10). Table 2.1 summarizes the nominal beam parameters of the ILC TDR taken from [15].

Table 2.1: Nominal beam parameters of the ILC TDR [15].

Parameters	Symbol	Unit	Values		
Centre-of-mass energy	E_{cm}	GeV	250	350	500
Number of electron per bunch	N_e	10^{10}	2.0	2.0	2.0
Number of bunches per pulse	n_b		1312	1312	1312
Bunch separation	Δt_b	ns	554	554	554
Pulse repetition rate	f_{rep}	Hz	5.0	5.0	5.0
Beam current	I_{beam}	mA	5.8	5.8	5.8
Main linac average gradient	G_a	MVm^{-1}	14.7	21.4	31.5
RMS bunch length	σ_z	mm	0.3	0.3	0.3
RMS horizontal beam size at IP	σ_x	nm	729	684	474
RMS vertical beam size at IP	σ_y	nm	7.7	5.9	5.9
Electron beam polarization	P_-	%	80	80	80
Positron beam polarization	P_+	%	30	30	30
Luminosity	L	$10^{34}cm^{-2}s^{-1}$	0.75	1.0	1.8

2.3.2 Compact Linear Collider Project

The Compact Linear Collider (CLIC) is a future $e^- e^+$ linear collider that will be hosted in CERN. CLIC is still under development at CERN and being carried out by a global collaboration. In principle, the CLIC is similar to the ILC, but it can go to higher energy (> 1 TeV). Figure 2.4 shows all the major systems and subsystems of CLIC.

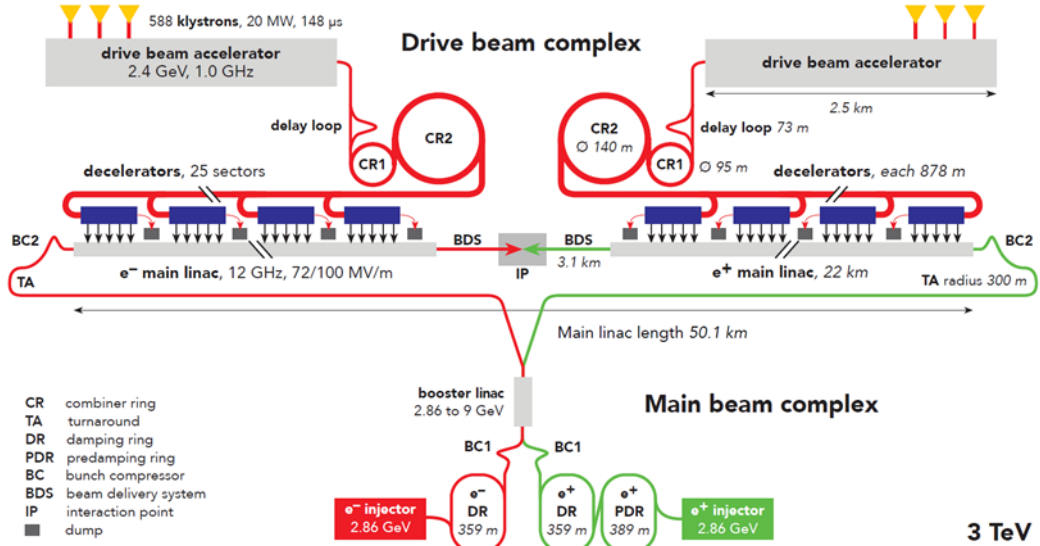


Figure 2.4: Schematic layout of the Compact Linear Collider (CLIC) baseline configuration [16].

The proposed stages of the CLIC are to operate in stages at 380 GeV, 1.5 TeV, and 3 TeV centre-of-mass energies, respectively [16]. The CLIC length would be between 11 km for the first energy stage at 380 GeV and 50 km long for the energy stage at 3 TeV. It is almost ten times longer than SLAC. The CLIC would use a novel two-beam acceleration technique with a high accelerating

gradient in the range of 70 MV/m to 100 MV/m. For 380 GeV centre-of-mass energy, the number of particles per bunch is 5.2×10^9 , with 352 bunch per train with 50 Hz. The accelerating gradient is 72 MV/m. CLIC has one interaction point with two detectors. More details about the CLIC project can be found in [16, 17].

2.3.3 FCC-ee Project

The Future Circular Collider (FCC) is being studied to operate at a centre-of-mass energy of up to 100 TeV for proton–proton collisions with a circumference of ≈ 100 km (FCC-hh), which is the ultimate stage of the FCC [18]. In the first stages, it is considered to operate an e^-e^+ collider (FCC-ee) with very high luminosity at energies up to 365 GeV. In addition, there are other possible options, such as a proton–electron collider (LHeC and FCC-he). For the comparison with the ILC, mainly the FCC-ee option is important here.

The main point of the FCC-ee is to operate at the Z boson resonance and to improve the results of LEP and SLC by more than one order of magnitude. The FCC-ee will be run in stages with energies between 88 GeV and 365 GeV to study with unprecedented precision the Z and W bosons, the Higgs boson, and the top quark. More details can be found in references [18, 19, 20].

Chapter 3

Positron Production

Positrons, which are the antiparticles of electrons, are produced through the electron-positron (e^-e^+) production process. The principle of generating positrons for high-energy colliders is introduced here.

3.1 Generation of Positrons

The most effective process to generate positrons is the e^-e^+ pair production. The pair production happens by sending a high-energy photon to interact with matter.

The pair production process is written as follows:



Feynman graphs are shown in figure 3.1.

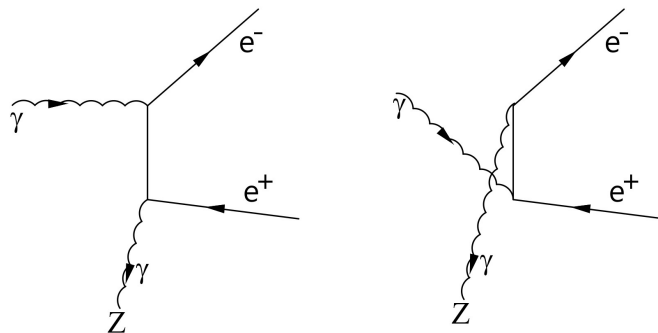


Figure 3.1: Feynman graphs for the pair production process.

For the pair production process, the probability, or cross section (σ_{pair}), is approximately proportional to the square of the atomic number (Z) of the target nucleus [21]. Figure 3.2 shows the

cross section of the photon as a function of the photon energy in titanium. The data in this figure was obtained from XCOM [22]. As shown in figure 3.2, the probability of producing an e^-e^+ pair increases with the energy of the photons. The pair production process is dominant at high energy, although the particles from the Compton scattering process, which may only increase the stress on the target, are there.

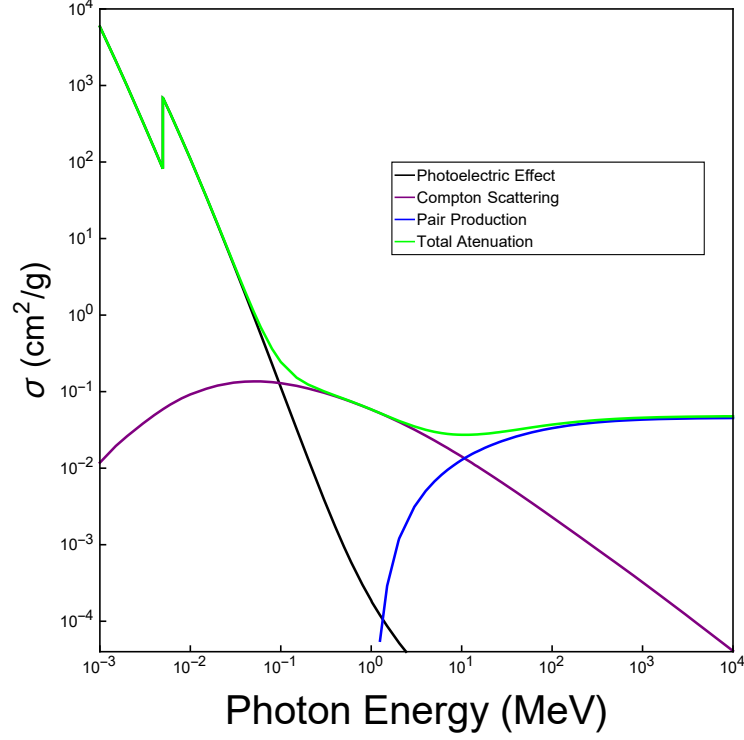


Figure 3.2: The cross section of a photon as a function of the photon energy in titanium. Data were obtained from XCOM [22] and plotted by Mathematica.

The probability (P) of the e^-e^+ pair production by a photon with high energy passing through a material with a thickness of x is given by:

$$P = 1 - e^{(-x n_{atom} \sigma_{pair})} \quad (3.2)$$

Where, n_{atom} is the number of atoms per unit volume, $n_{atom} = \frac{\rho N_A}{A}$, and σ_{pair} is the cross section of the pair production process.

The probability that a photon can produce an electron-positron pair is correlated to the cross section. Therefore, only few percentage of the incident photons on the target will produce positrons, while the rest will pass through the target and be dumped. Assuming photons of 7.6 MeV passing a titanium with a thickness of 0.2 radiation length, more than 1×10^{16} photons per second are required in order to generate 2×10^{14} positrons per second, which is the required positron number for the ILC positron beam. However, taking into account all processes in the target as well as the efficiency to capture and accelerate the generated e^+ , substantially more photons are necessary to

produce the necessary amount of e^+ (see also section 4.1).

Figure 3.3 shows how the positron yield per photon with an energy of 7.6 MeV differs with increasing the thickness of the material; here titanium is used.

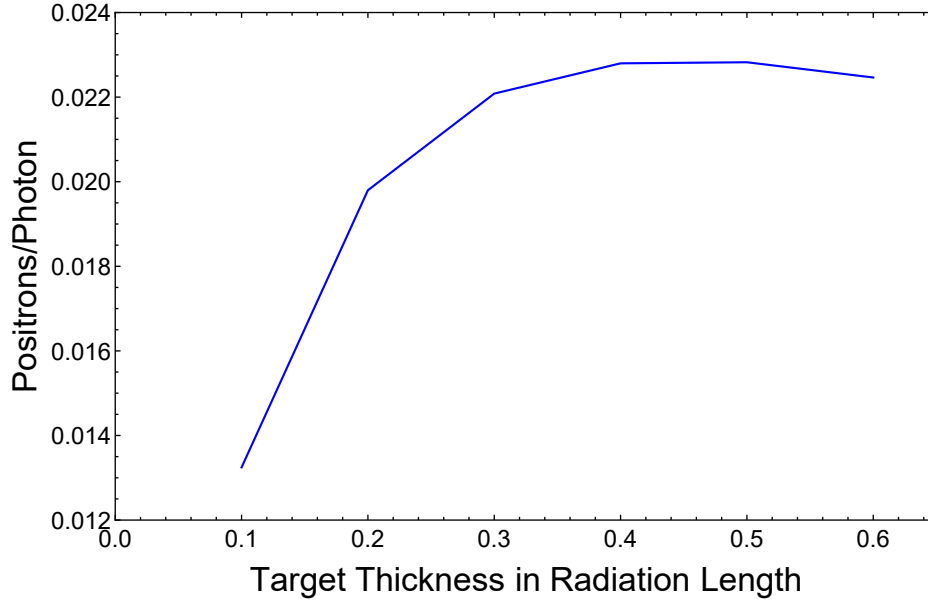


Figure 3.3: The positron yield as a function of the target thickness. The target material is titanium and the photon energy is 7.6 MeV. FLUKA is used for this simulation.

If such a high-energy photon is not "available", the photon for the pair production can be produced by the bremsstrahlung of electrons in matter. When a high-energy electron (or positron) passes through matter, it loses energy by emitting a photon (bremsstrahlung). The bremsstrahlung process is written as follows:



The Feynman graphs for the bremsstrahlung process are shown in figure 3.4:

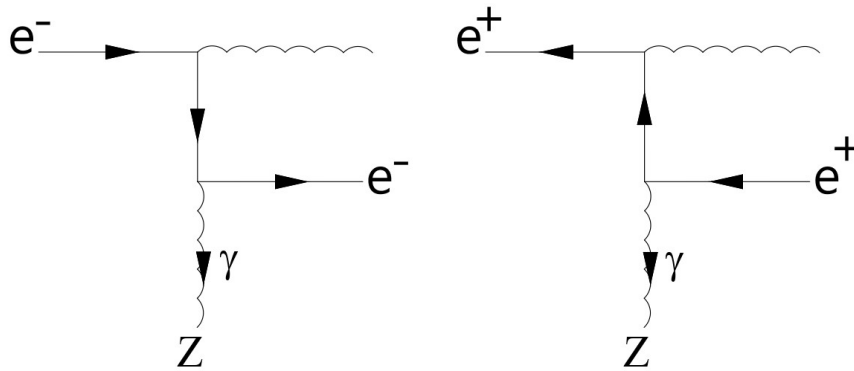


Figure 3.4: Feynman graph for the bremsstrahlung processes.

The photon produced by the bremsstrahlung process must have, at least, few MeV and interact

with a material to produce an electron-positron pair. This pair, with enough energy, will emit two photons, which will produce another pair. Within few radiation lengths of material, this sequence continues to create an electromagnetic shower (for more details about the electromagnetic shower, see Appendix A). In the ILC, an electron beam with an energy of a few GeV and a material with a high atomic number with a thickness of a few radiation lengths are necessary to produce the required e^+ yield (see also section 4.2).

3.2 Polarized Positron Beam

Producing a polarized positron beam is one of the most important tasks for any future electron-positron collider project, since it enhances the physics studies. More details about the benefits of both polarized electron and positron beams are discussed in [1, 2, 3]. In the ILC, the circularly polarized photon beam produced by the helical undulator is used to produce a longitudinally polarized positron beam. In 1959, Olsen and Maximon studied the polarization transfer from a circularly polarized photon beam to longitudinally polarized lepton beams created through the electron-positron pair process when the photon hits an infinitely thin target [23]. The polarization of the incoming photon beam is transferred to the outgoing lepton beams. More details about the polarization transfer can be found in Appendix A. Figure 3.5 shows the longitudinal polarization of lepton (electron or positron) beams created in an infinitely thin target by a circularly polarized photon beam [23].

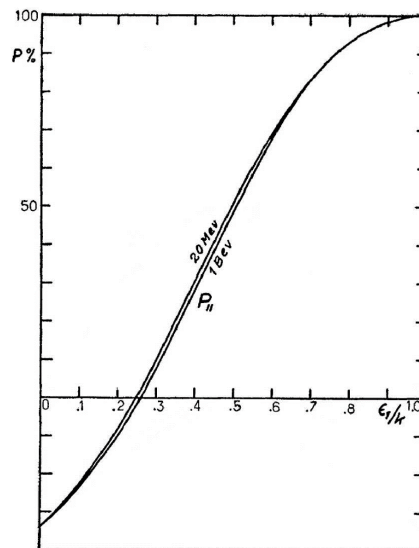


Figure 3.5: The longitudinal polarization of lepton (electron or positron) beam created in an infinitely thin target by circularly polarized photon beam, as a function of the ratio E_{e^+}/E_{γ} of positron to photon energies [23].

As can be seen in figure 3.5, the positron (electron) beam created by a circularly polarized photon beam is almost 100 % longitudinally polarized if its energy is close to that of the incoming photons.

The thickness of the target also determines the polarization of the produced positron beam. The proof-of-principle experiment (E-166) to test the e^+ production using a helical undulator at the Stanford Linear Accelerator Center (SLAC) has produced a photon beam with circular polarization. This beam was then converted in a thin target to longitudinally polarized positron and electron beams, as shown in reference [24]. The spectrum of the produced photon beam in the E-166 was used to calculate the polarization of the produced positron beam with different target thicknesses, as shown in figure 3.6.

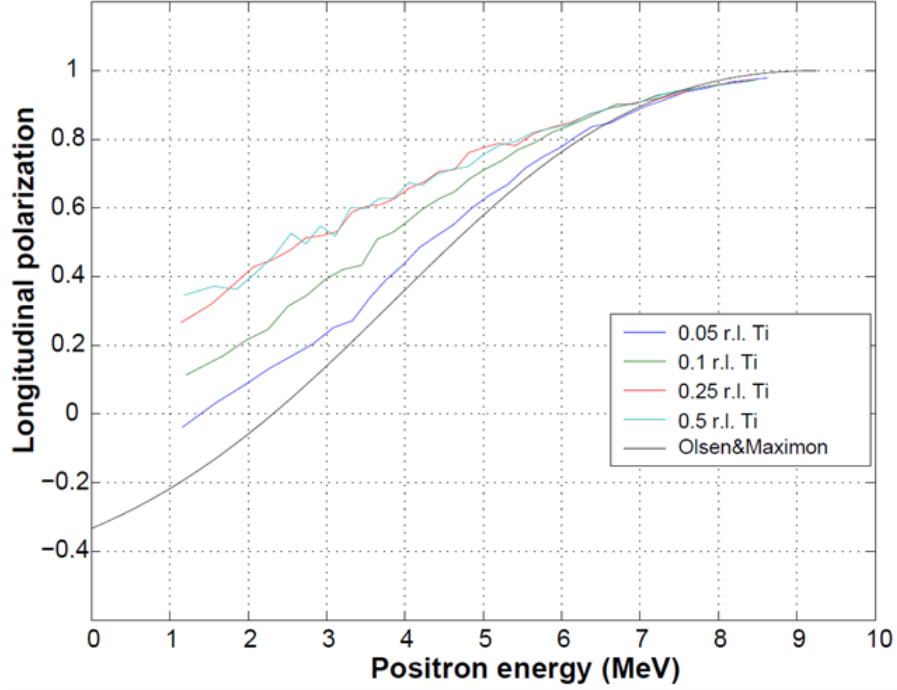


Figure 3.6: The longitudinal polarization of positron beam created by a circularly polarized photon beam with energy of 10 MeV in titanium target with different thicknesses in radiation lengths, as a function of the positron energy [24].

Figure 3.6 shows that by increasing the target thickness, the longitudinal polarization of the positron beam is increased [24], but, of course, this is at the expense of the intensity, as seen in figure 3.3. The material target used in this study is titanium.

Chapter 4

Positron Sources for High-Intensity Future Linear Colliders

The positron source is one of the most challenging areas in future electron-positron linear collider projects. A very intense positron source is required since the required positron number at the interaction point (IP) of, for example, the ILC is \approx hundreds of times higher than what was required at the SLC. The positron sources of future electron-positron linear collider projects have different designs. One method is that photons are produced by allowing electrons to interact with a thick target to produce positrons through the electromagnetic shower. The other method is to produce photons and send them to a thin converter target. This chapter briefly introduces the possible positron sources for future high-intensity linear colliders.

4.1 Undulator-Based Positron Source

The idea behind using an undulator-based positron source is to produce the photon beam with the required photon energy outside the converter target. This idea was first described in 1979 [25]. Here the undulator-based positron source is introduced, and the basics of the undulator will be introduced in chapter 5.

The undulator is an insertion device with a periodic structure of dipole magnets. The main purpose of the ILC undulator is to produce photons with energy of few MeV by forcing the electrons with energy > 100 GeV to oscillate as they travel through it. These photons are then directed to a thin target to produce positrons by a pair production mechanism. Figure 4.1 shows the schematic of a permanent magnet planar undulator. In this schematic, the oscillations of electrons are confined to a plane.

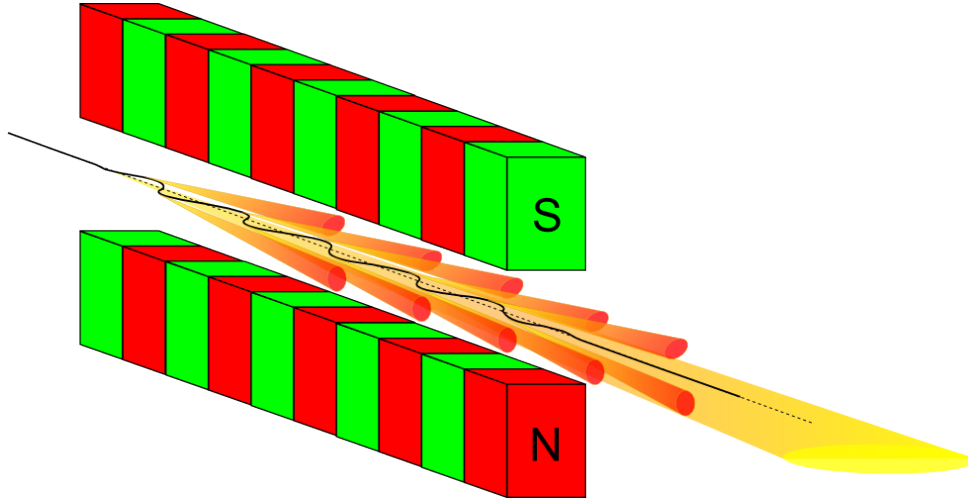


Figure 4.1: Schematic of a permanent magnet planar undulator. The red and green magnets are north and south poles, respectively. In between are the electron and produced photon beams [26].

Figure 4.2 shows the principle of the helical undulator-based positron source.

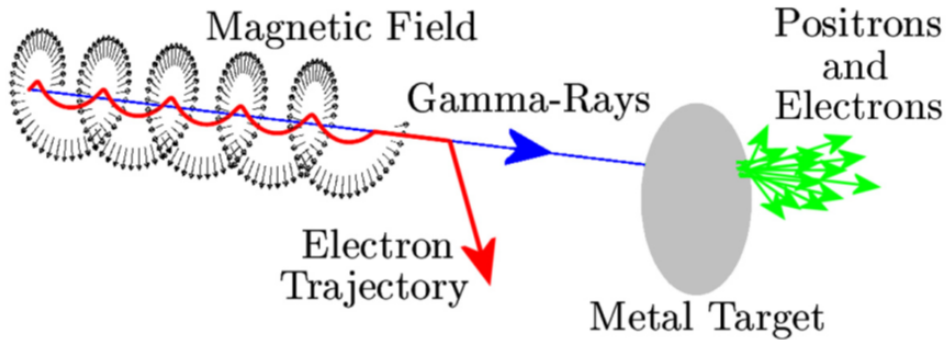


Figure 4.2: Principle of polarized positron beam produced by high-energy electron beam (red line) passing through a undulator with a helical magnetic field (black arrows) to produce a photon beam (blue line). Green arrows represent positrons and electrons generated through the electron-positron pair process when photons hit the metal target [27].

The advantages of the helical undulator over the planar undulator are that the number and power of photons produced per period of a helical undulator are up to twice that produced per period of a planar undulator with the same parameters. In addition, since the helical undulator produces a circularly polarized photon beam, there is a possibility of producing a longitudinally polarized positron beam by these photons. Due to the rotating magnetic field in the helical undulator, the electron beam trajectory is helical, proportional to the undulator period. The trajectory of the electron beam results in emitting a high-energy photon beam with circular polarization. The positron beam produced through the electron-positron pair process will inherit the polarization of this photon beam. A detailed study about the differences between planar and helical undulators has been conducted by Alexander Mikhailichenko in [28] and by Klaus Flottmann in [29].

4.1.1 Layout of the ILC Helical Undulator Source

The TDR of the ILC proposes the helical undulator-based positron source as the baseline of the ILC positron source. The ILC helical undulator is located at the end of the main linac of the electron. Figure 4.3 shows the layout of the ILC helical undulator-based positron source [11].

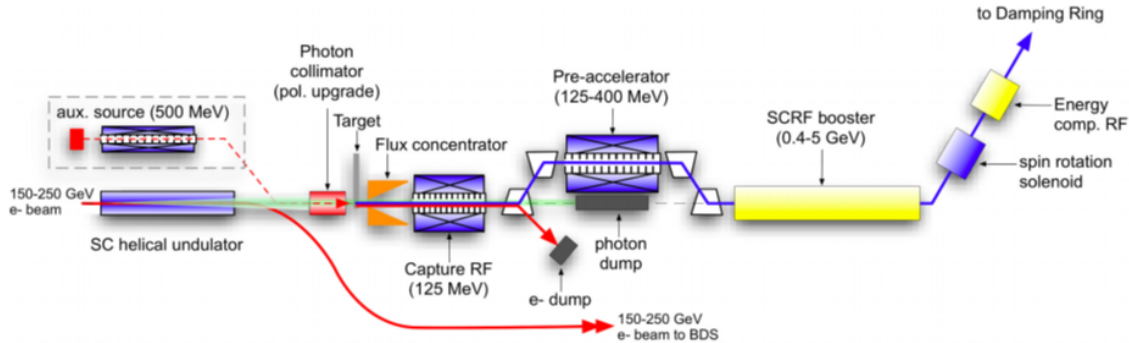


Figure 4.3: Layout of the ILC positron source. Figure is taken from [11].

A multi-GeV (> 100 GeV) electron beam passes through a helical undulator to produce a multi-MeV circularly polarized photon beam. The electron beam is then directed to the IP, while photons are incident on the target to produce positrons through the electron-positron pair. Depending on the electron energy, the target thickness is between 0.2 and 0.4 radiation lengths.¹ The target is a rotating wheel made of titanium alloy (Ti6Al4V) with a speed of 100 m/s, and a diameter of 1 m. After the target, positrons are captured by an Optical Matching Device (OMD), and photons and electrons are dumped. More detail about the ILC target and OMD can be found in [11, 30, 31]. Since a few of the photons will produce positrons, a particular system is required to dump the unused high-intensity photon beam after the OMD [32, 33]. The captured positrons are accelerated from 125 MeV to 400 MeV by the pre-accelerator. Then the positron beam with an energy of 400 MeV is directed to a superconducting Booster Linac to be accelerated up to 5 GeV. A spin rotation solenoid is used to change the spin of positrons from the longitudinal to the horizontal plane and then to the vertical in order to preserve the polarization in the positron DR. In addition, a special spin flipper that randomly flips the spins of the half-part of positrons to the other direction is needed. A study and possible design of a spin rotator and flipper for the ILC are discussed in [34]. Before injecting the positron beam into the positron DR, the energy compression is done using a separate superconducting RF structure.

The benefits of using the helical undulator-based positron source in the ILC are that the produced photon beam has a high intensity with circular polarization, which leads to a positron beam with a polarization of 30 %. This concept has been successfully demonstrated by the E-166 experiment at SLAC [24]. Moreover, the ILC helical undulator cryomodule prototype has been built, and

¹The target thickness of the ILC-350 and ILC-500 is always assumed to be 0.4 radiation length.

the B-field of the undulator has been tested [35]. In addition, the target prototype has been built and studied [36]. However, it has to be considered that the commissioning of the positron machine is more complicated without a high-energy e^- beam.

4.1.2 Parameters of the ILC Helical Undulator

The undulator parameters determine the intensity and shape of the photon spectrum. Therefore, changing the undulator parameters leads to changes in the positron distribution, which will cause changes in other source components.

In the helical undulator, to create such a powerful helix magnetic field ($B_0 \sim 0.79$ T) with a short helical undulator period (λ_u) in the range of 11.5 mm, the undulator aperture (d_u) must be tiny (~ 5.85 mm). Figure 4.4 shows a diagram of a wire wound in a double helix. In this schematic, two equal currents flow in opposite directions through two superconducting wires to create a double helix around the electron beam axis (z-axis).

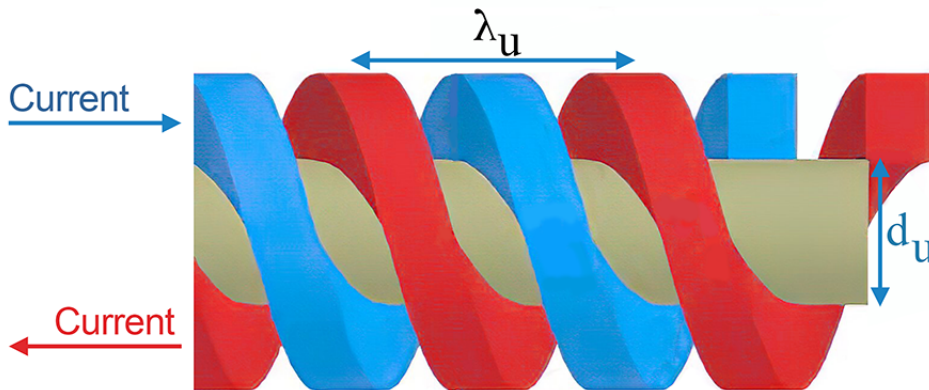


Figure 4.4: Diagram of a wire wound in double helix.

As discussed in chapter 3, photons with an energy of few MeV are needed to produce positrons. The ILC positron source parameters have been updated since the start of the ILC project in 2005. Following the Higgs boson discovery in 2012, the nominal parameters of the ILC Linac beam were changed from 500 GeV to 250 GeV centre-of-mass energy. Therefore, a longer helical undulator is needed to produce the required photon number. The ILC TDR, published in 2013, contains a detailed baseline design of the entire ILC project and parameters for the positron source after the high-energy ILC upgrade [11]. The last update of the positron source parameters for the ILC is in [13] and shown in table 4.1. The impact of each undulator parameter on the photon spectrum will be seen in chapter 5.

The required positron yield at the ILC positron DR is $1.5 e^+ / e^-$. The helical undulator of the ILC-250 should produce photons with an average energy of ≈ 7.6 MeV, which will hit the Ti6Al4V

Table 4.1: Nominal beam parameters of the ILC TDR [13, 15, 30].

Parameters	Symbol	Unit	Value		
Centre-of-mass energy	E_{cm}	GeV	250	350	500
Electron energy	E_e	GeV	128	178	253
Undulator period	λ_u	mm	11.5	11.5	11.5
Required undulator B-field	B	T	0.79	0.698	0.42
Undulator K	K		0.85	0.75	0.45
Electron energy loss in undulator	E_{loss}	GeV	3	2.6	2
Average photon energy	E_γ	MeV	7.6	14.0	27.0
Total active undulator length	L_u	m	231	147	147
Number of electron per bunch	N_e	10^{10}	2.0	2.0	2.0
Number of bunches per pulse	n_b		1312	1312	1312
Bunch separation	Δt_b	ns	554	554	554
Pulse repetition rate	f_{rep}	Hz	5.0	5.0	5.0
Target thickness	X_0	Hz	0.2	0.4	0.4

target with a thickness of 0.2 radiation length. The cross-section can be obtained from figure 3.2. Therefore, $\approx 1.05 \times 10^{16}$ photons per second are required to produce the required positron number, which is 2×10^{14} positrons per second. This is if we assume that the efficiency of the OMD is 100%, but the efficiency is somehow between 15% and 25% depending on the design, which is still under study. Therefore, if we assume that the efficiency of the OMD is 20%, then instead of $\approx 1.05 \times 10^{16}$ photons per second, the required photon number becomes $\approx 5.25 \times 10^{16}$ photons per second to produce 1×10^{15} positrons per second directly after the target. In this case, we can achieve the required positron yield at the positron DR.

4.2 Electron Driven Positron Source

The Electron Driven (e-driven) positron source is an alternative option in the ILC. This method has been used successfully in real projects for over 40 years, such as in SLC. However, the required positron yield in the ILC is almost a hundred times as high as in the SLC. Physicists have more experience with this kind of source compared with other sources. Figure 4.5 shows the schematic layout of the ILC e-driven positron source [37].

In this scheme, the ILC e-driven positron source uses an electron driver linear accelerator to produce a 3 GeV electron beam. This beam is then directed to a tungsten-rhenium (W-Re) target with a rotation speed of 5 m/s and a thickness of 16 mm to produce positrons through the electromagnetic shower process. After the target, positrons with a large momentum deviation, photons, and electrons are removed, while wanted positrons are captured and accelerated up to 250 MeV. Then positrons are accelerated up to 5 GeV before being sent to the positron DR.

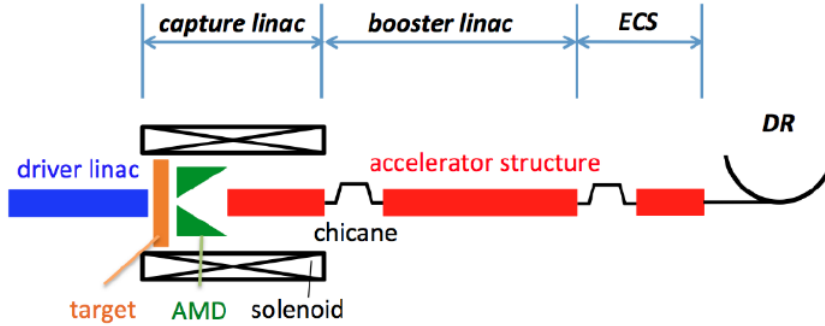


Figure 4.5: Schematic of the ILC E-driven positron source [37].

In this scheme, the parameters for generating the required positrons for the ILC are 20 pulses at 300 Hz with 66 bunches each and 2×10^{10} electrons per bunch. This scheme takes approximately 67 ms to generate the required positrons for the ILC single Main Linac pulse with its 1312 bunches, compared with 0.8 ms for the helical undulator-based positron source. Positrons are then sent to the positron DR. Positrons are kept in the positron DR for 136 ms before being sent to the positron main linac to be accelerated to the required energy and then sent to the IP. The beam structure should be matched in this configuration, although it depends on the DR fill pattern. This design, with these parameters, can produce the required positron yield of the ILC [30, 38]. The main disadvantage of the e-driven source compared with the helical undulator is that the e-driven source provides an unpolarized positron beam with substantial consequences for the physics potential of the ILC [39].

The ILC Positron Source Group has recently discussed and studied the helical undulator-based, and e-driven positron source schemes in the ILC community [30]. As a result, both source ideas will work with no known problems that would stop them, but they need more engineering work.

4.3 Laser-Compton Positron Source

Another possible positron source is the laser-Compton. This source is based on two fundamental processes: backward Compton scattering of the circularly polarized laser light and the pair production of the polarized gamma rays (γ -rays) [40]. The principle of this scheme is shown in figure 4.6.

Polarized gamma rays are created by a circularly polarized laser light through backward Compton scattering, and these gamma rays are directed to hit a thin target. As a result, the electron-positron pairs are created by some of these gamma rays. The kinematics of the Compton scattering are determined by the energy of both electron beam and laser photons, the interaction angle between the laser photons and the electron beam, and the backscattering angle. This angle is the angle between the produced photons by Compton scattering and the electron beam. The main advantage

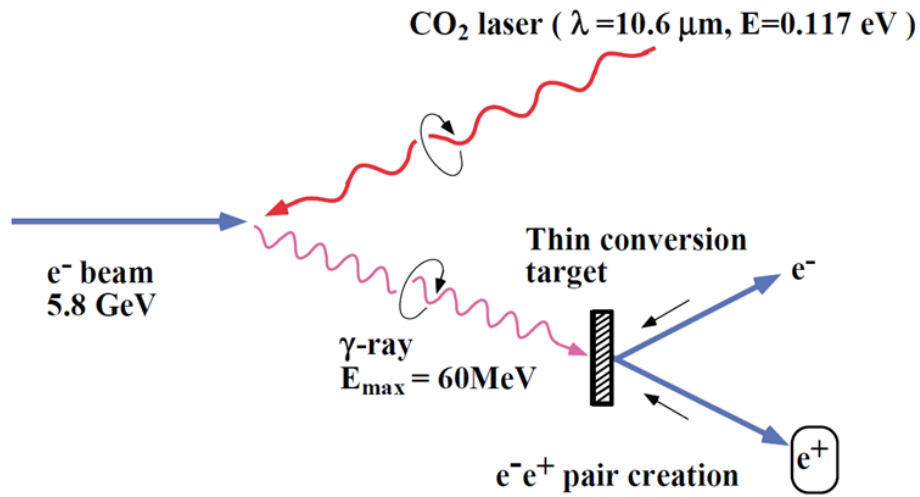


Figure 4.6: Principle of laser-Compton positron source [40]

of the laser-Compton positron source is that the photon beam is polarized, so there is a possibility of producing a polarized positron beam. In addition, it is independent of the e^- beam for the e^+e^- collisions. However, this source has the challenge of producing the required photon number that will be used to create the required positron number. This source is discussed in more detail in [40].

Chapter 5

Synchrotron Radiation from a Helical Undulator

This chapter presents the physics of helical undulators. By the end of this chapter, the effect of each undulator parameter on the photon spectrum and polarization beam produced by a helical undulator will be understood.

5.1 Synchrotron Radiation

The Synchrotron Radiation (SR) is the electromagnetic radiation that is emitted when relativistic charged particles undergo acceleration [41]. This radiation was first observed in April 1947 at the General Electric Company Research Laboratory in New York State [42].

The SR can be understood by two basic processes: Lorentz contraction and relativistic Doppler shift [43]. For example, considering a relativistic charged particle that travels at almost the speed of light and passes through an undulator. In the moving frame, if the undulator period is λ_u , the electron will see it as $\frac{\lambda_u}{\gamma}$. As a result, the electron emits a radiation with a wavelength of $\frac{\lambda_u}{\gamma}$. Here, γ is the relativistic Lorentz factor and given by:

$$E_e = \gamma m_0 c^2 = \gamma E_0 \quad (5.1)$$

Where, c is the speed of light, E_0 is the electron rest energy and E_e is the electron energy.

For the relativistic Doppler effect, the observer sees the frequency of the emitted light, at rest, f , is:

$$f = \gamma f' (1 + \beta \cos \theta') \quad (5.2)$$

Where, f' and θ' are the frequency emitted by the moving electron and the angle between the emitted light and the observer, respectively. β is the relative velocity of electron and given by:

$$\beta = \sqrt{1 - \frac{1}{\gamma^2}}, \beta = v/c \quad (5.3)$$

Where, v is the speed of the electron.

If the particle travels towards the observer, where $\theta' = \pi$, the observer sees the frequency of the emitted light as:

$$f = \gamma f' (1 + \beta) \quad (5.4)$$

If the frequency is converted to the wavelength, equation 5.3 becomes:

$$\lambda = \frac{\lambda'}{\gamma(1 + \beta)} \quad (5.5)$$

Where, λ is the wavelength of the emitted light seen by the observer and λ' is the wavelength emitted by the moving electron. If it is assumed that the β of the relativistic source is ≈ 1 , then equation 5.5 becomes:

$$\lambda \approx \frac{\lambda'}{2\gamma} \quad (5.6)$$

The result of combining these two effects shows that the electron emits a light with a wavelength of $\frac{\lambda_u}{\gamma}$ and if it travels towards to the observer, this wavelength is further reduced by 2γ . So the wavelength of the emitted radiation that is seen by the observer in the rest frame will be $\frac{\lambda_u}{2\gamma^2}$. Therefore, when electrons are accelerated to tens of GeV, the value of γ reaches tens of thousands. Also, when the period of undulators is reduced to a centimeter, the wavelength of the emitted radiation reaches few nanometers.

Another characteristic of the SR is that the SR is emitted into a narrow cone with an opening angle of $\approx \frac{1}{\gamma}$ around the instantaneous direction of the particle (the electron) trajectory. Since the undulator is being an interference device, the result is that a further narrowing of the cone is being added by a factor of \sqrt{N} . Here N represents the number of the undulator periods. This signifies that using undulators in high energy accelerators can create highly intense radiation with very small wavelengths (a few nanometers).

Now the properties of the SR from a helical undulator will be studied in more details.

5.2 Radiation from a Helical Undulator

The helical undulator device is an Inserting Device (ID) that is used to produce photon radiation when an electron beam passes through it. The helix magnetic field is around the electron beam, so the field oscillates the electron beam, resulting in an emitting circularly polarized photon beam. Equation 5.7 shows the general expression for the energy radiated (U) per unit angular frequency (ω) per unit solid angle (Ω) emitted by one relativistic charged particle in a magnetic field [44]:

$$\frac{d^2U}{d\Omega d\omega} = \frac{\omega^2 q^2}{16\pi^3 c \epsilon_0} \left| \int_{-\infty}^{\infty} \left(\vec{n} \times \left(\vec{n} \times \vec{\beta} \right) \right) e^{i\omega \left(t' + \frac{r_e}{c} \right)} dt' \right|^2 \quad (5.7)$$

Where the q represents the electron charge, \vec{n} represents the unit vector in the direction to the observer, r_e represents the electron trajectory, and the $\vec{\beta}$ represents that the particle velocity is a function of 'retarded time t' '. The electron trajectory in an undulator device has to be determined in order to calculate the SR spectrum created by this undulator device. In the case of the ILC, the helical undulator is interesting. In the helical undulator, the electron trajectory is a helix, and its period is proportional to the undulator period (λ_u), and the amplitude depends on the magnetic field strength and the electron driven beam energy. The motion equations for the electron can be written as follow [43]:

$$\ddot{x} = \frac{d^2x}{dz^2} = \frac{q}{m_0 c^2 \gamma} (B_y - y B_z) \quad (5.8)$$

$$\ddot{y} = \frac{d^2y}{dz^2} = \frac{q}{m_0 c^2 \gamma} (\dot{x} B_z - B_x) \quad (5.9)$$

Since there is no a magnetic field in the z direction of undulators, $B_z = 0$. So equations 5.8 and 5.9 become:

$$\ddot{x} = \frac{d^2x}{dz^2} = \frac{q}{m_0 c^2 \gamma} (B_y) \quad (5.10)$$

$$\ddot{y} = \frac{d^2y}{dz^2} = -\frac{q}{m_0 c^2 \gamma} (B_x) \quad (5.11)$$

The magnetic field of a helical undulator is given by:

$$B_x = B_{x0} \sin\left(\frac{2\pi z}{\lambda_{xu}}\right) \quad (5.12)$$

$$B_y = B_{y0} \cos\left(\frac{2\pi z}{\lambda_{yu}}\right) \quad (5.13)$$

Substituting these into equations 5.10 and 5.11 we get:

$$\ddot{x} = \frac{d^2x}{dz^2} = \frac{q}{m_0c^2\gamma} B_{y0} \cos\left(\frac{2\pi z}{\lambda_{yu}}\right) \quad (5.14)$$

$$\ddot{y} = \frac{d^2y}{dz^2} = -\frac{q}{m_0c^2\gamma} B_{x0} \sin\left(\frac{2\pi z}{\lambda_{xu}}\right) \quad (5.15)$$

By integrating equation 5.14 and 5.15 with respect to z, \dot{x} and \dot{y} can be got:

$$\dot{x} = \frac{dx}{dz} = \frac{q\lambda_{yu}}{m_0c^2\gamma 2\pi} B_{y0} \sin\left(\frac{2\pi z}{\lambda_{yu}}\right) \quad (5.16)$$

$$\dot{y} = \frac{dy}{dz} = \frac{q\lambda_{xu}}{m_0c^2\gamma 2\pi} B_{x0} \cos\left(\frac{2\pi z}{\lambda_{xu}}\right) \quad (5.17)$$

Here \dot{x} and \dot{y} represent the horizontal and vertical deflection angles. The maximum deflection angles (K_y and K_x) experienced by the electron are given by:

$$K_y = \frac{q\lambda_{yu}}{m_0c^2\gamma 2\pi} B_{y0} \quad (5.18)$$

$$K_x = \frac{q\lambda_{xu}}{m_0c^2\gamma 2\pi} B_{x0} \quad (5.19)$$

Equations 5.16 and 5.17 can be integrated in order to calculate the position of the electron in a helical undulator:

$$x = \frac{dx}{dz} = -\frac{K_y \lambda_u}{\gamma 2\pi} \cos\left(\frac{2\pi z}{\lambda_u}\right) \quad (5.20)$$

$$y = \frac{dy}{dz} = \frac{K_x \lambda_u}{\gamma 2\pi} \sin\left(\frac{2\pi z}{\lambda_u}\right) \quad (5.21)$$

If we assume that

$$\lambda_{xu} = \lambda_{yu} = \lambda_u \quad (5.22)$$

and

$$B_{x0} = B_{y0} = B_0 \quad (5.23)$$

then

$$K_x = K_y = K \quad (5.24)$$

So, K is proportional to the undulator period (λ_u) and the peak magnet field strength (B_0) and is

given by:

$$K = \frac{q\lambda_u B_0}{2\pi mc^2} = 0.934\lambda_u(cm)B_0(T), \quad (5.25)$$

Assuming γ is large, and $N > 100$, equation 5.7 can be used to integrate the energy radiated from a helical undulator at a particular frequency and opening angle. The integration was performed by Brian Kincaid and the integration steps can be found in [45]. The result is given by:

$$\frac{d^2W}{d\Omega d\omega} = \frac{q^2\omega^2 K^2}{4\pi^3\epsilon_0 c\gamma^2\omega_0^2} \sum_{n=1}^{\infty} \left[J_n'^2(x) + \left(\frac{\theta\gamma}{K} - \frac{n}{x}\right)^2 J_n^2(x) \right] \frac{\sin^2 \left[N\pi \left(\frac{\omega}{\omega_1} - n \right) \right]}{\left(\frac{\omega}{\omega_1} - n \right)^2} \quad (5.26)$$

Where $J_n(x)$ is the Bessel function, θ is the angle between the z-axis of the helical undulator and the observation point, and N represents the number of periods in the helical undulator, n is the harmonic number. ω_0 is the circular frequency of the electron's helical orbit. The other terms in the expression are:

$$x = \frac{K\theta}{\gamma} \frac{\omega}{\omega_0}, \quad (5.27)$$

$$\omega_0 = \frac{2\pi\beta^*c}{\lambda_u}, \quad (5.28)$$

$$\omega_1 = \frac{\omega_0}{1 - \beta^* \cos\theta} \approx \frac{2\gamma^2\omega_0}{1 + K^2 + \gamma^2\theta^2}, \quad (5.29)$$

Here, β^* represents the average velocity of the electron in the z direction and is given by :

$$\beta^* = \beta \left[1 - \left(\frac{\lambda_u}{2\pi\rho_{cyc}} \right)^2 \right]^{\frac{1}{2}} \quad (5.30)$$

$$= \beta \left[1 - \left(\frac{K}{\gamma} \right)^2 \right]^{\frac{1}{2}} \quad (5.31)$$

Here, ρ_{cyc} is the cyclotron radius, which is the radius of the motion of the particle inside the helical undulator.

5.2.1 Photon Number Spectrum

The total radiated energy spectrum as a function of frequency can be calculated by integrating equation 5.26 over all angles as given by [45]:

$$\frac{dW}{d\omega} = \frac{N_p K^2 q^2 r}{\epsilon_0 c} \sum_{n=1}^{\infty} \left[J_n'^2(x_n) + \left(\frac{a_n}{K} - \frac{n}{x_n} \right) J_n^2(x_n) \right] u(a_n^2) \quad (5.32)$$

Where:

$$a_n^2 = \frac{n}{r} - 1 - K^2, \quad (5.33)$$

$$x_n = 2Kra_n, \quad (5.34)$$

$$r = \frac{\omega}{2\gamma^2\omega_0}, \quad (5.35)$$

and $u(a_n^2)$ is the unit step function.

The photon number spectrum can be calculated by using the relationship between the radiation frequency ω and photon energy E_γ . So, the photon number spectrum can be calculated by dividing equation 5.32 by $\omega\hbar$. Figure 5.1 shows the spectrum of photon number per unit energy range for the first five harmonics from a helical undulator. The different harmonics have been plotted separately to show how the significance of the higher harmonics decreases.

The effect of each parameter, including λ_u , undulator length, K value and E_e , on the photon spectrum will be discussed separately.

5.2.1.1 K Value

As seen in equation 5.25, the K value depends directly on the λ_u and the B field. Equation 5.32, which is valid for a helical undulator with $N \geq 100$ as discussed in [45], is used to calculate the photon spectrum created by a helical undulator. Figure 5.2 shows the photon spectrum created by a 1.75 m helical undulator length with different K values. For each K value, the λ_u is fixed (11.5 mm), while the B-field has been changed in order to change the K value. The photon spectrum with different K values have been plotted to show the effect of the K value on the photon number spectrum.

By increasing the K value, the photon number and the photon average energy increase, while the energy cut-off decreases.

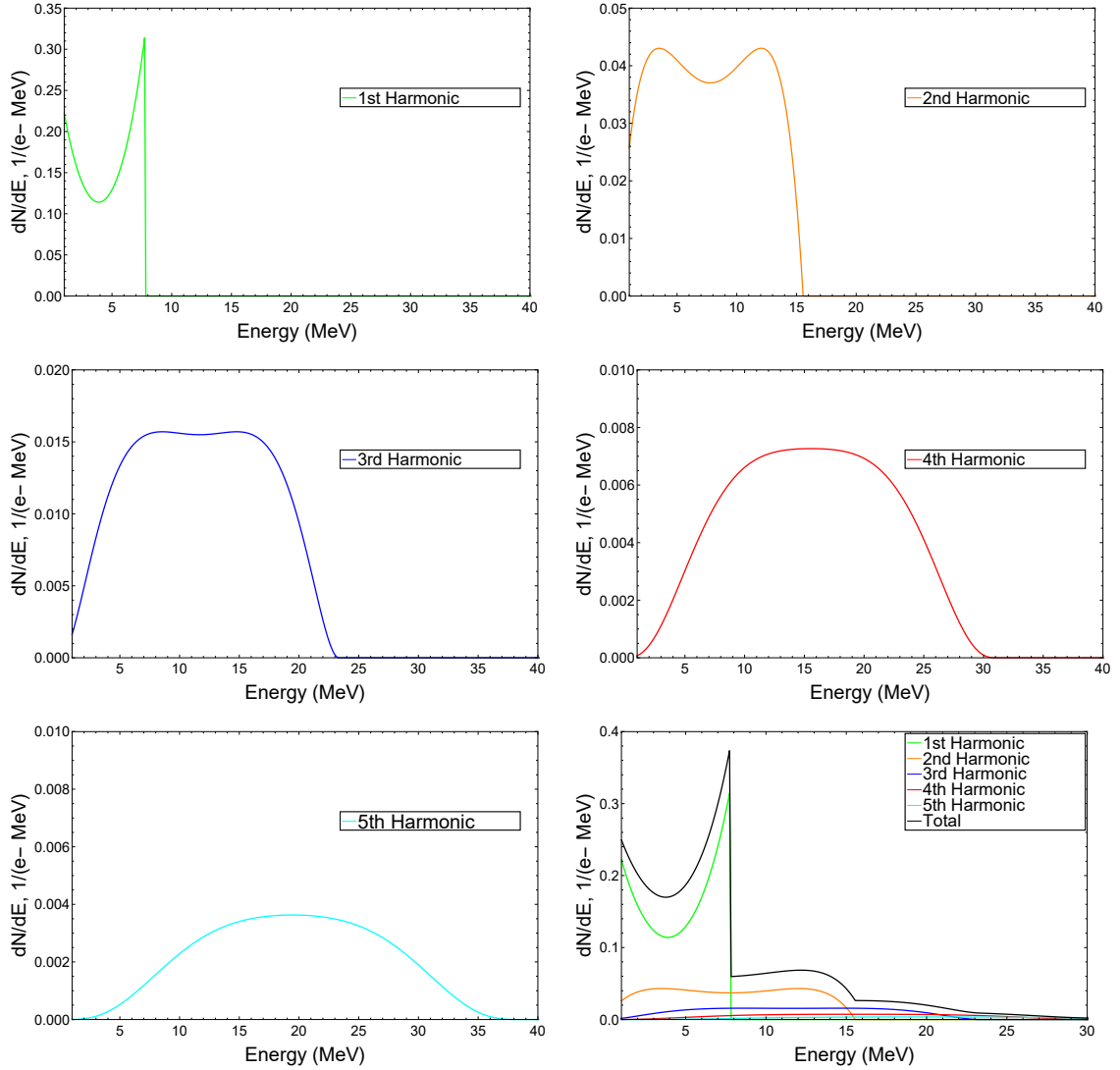


Figure 5.1: Photon number spectrum for the first five harmonics. Each plot represents a separated harmonic. The plot on the bottom right shows the total photon number of all the five harmonics. Using a 1.75 m helical undulator length with an undulator period of $\lambda_u = 11.5$ mm, $K = 0.85$ and the electron energy is $E_e = 125$ GeV.

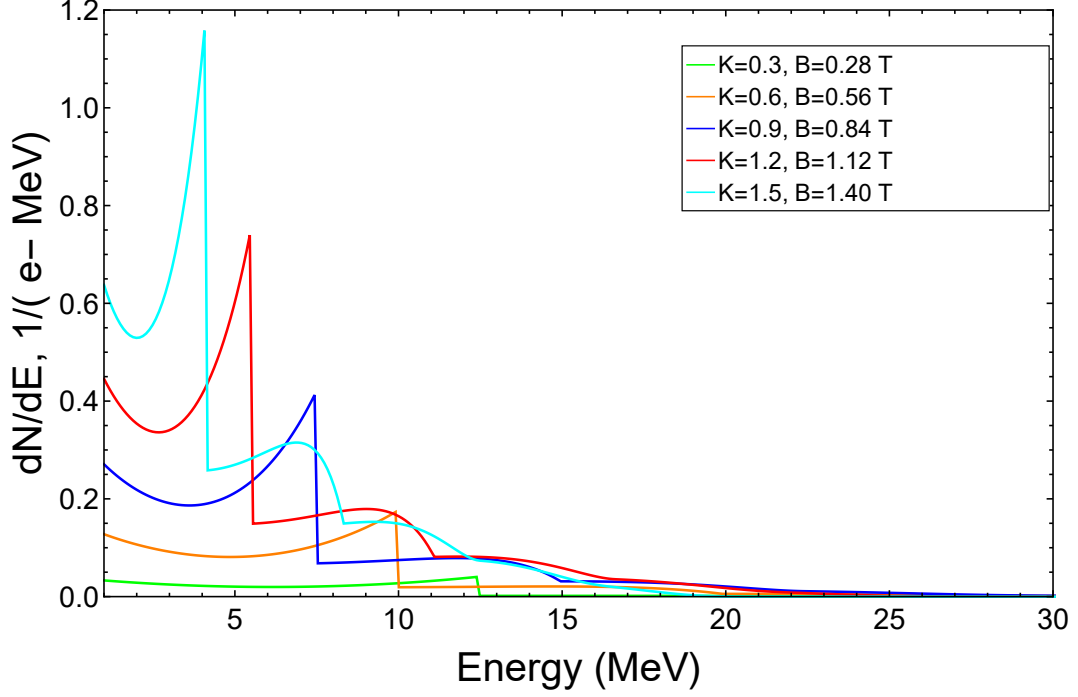


Figure 5.2: Photon spectrum created by a 1.75 m helical undulator length using different K values $K=0.3, 0.6, 0.9, 1.2$ and 1.5 . The undulator length and period ($\lambda_u = 11.5$ mm) are fixed. It means that when $K=0.3$, the B-field is 0.28 T, and when $K=1.5$, B-field is 1.4 T. The electron energy is $E_e = 125$ GeV.

5.2.1.2 Undulator Period

Photons are produced as long as the electron beam is shaking. The effect of the size of the undulator period on the photon spectrum is discussed. Equation 5.32 is used to calculate the photon spectrum created by a helical undulator. Figure 5.3 shows the photon spectrum produced by a 1.75 m undulator length for different period sizes using $K = 0.85$ and an electron energy of 125 GeV. To keep the overall undulator length constant at 1.75 m, the number of periods has been changed for each period size shown in figure 5.3. Also, for each of the period size shown, the B-field has been changed to keep the K value constant at 0.85.

The significance of the size of the undulator period is clear on the spectrum of the photon number. For higher period sizes, the average energy and number of photons decreases. For example, the average energy of the photon beam is 6.7 MeV and 8.4 MeV for period size 12.5 mm (B-field = 0.73 T) and 10.0 mm (B-field = 0.91 T), respectively. So using a smaller period allows for a reduction in the overall undulator length which will lead to decrease the photon beam spot size and, in the same time, the average energy of photons increases which will help to increase the probability to produce positrons.

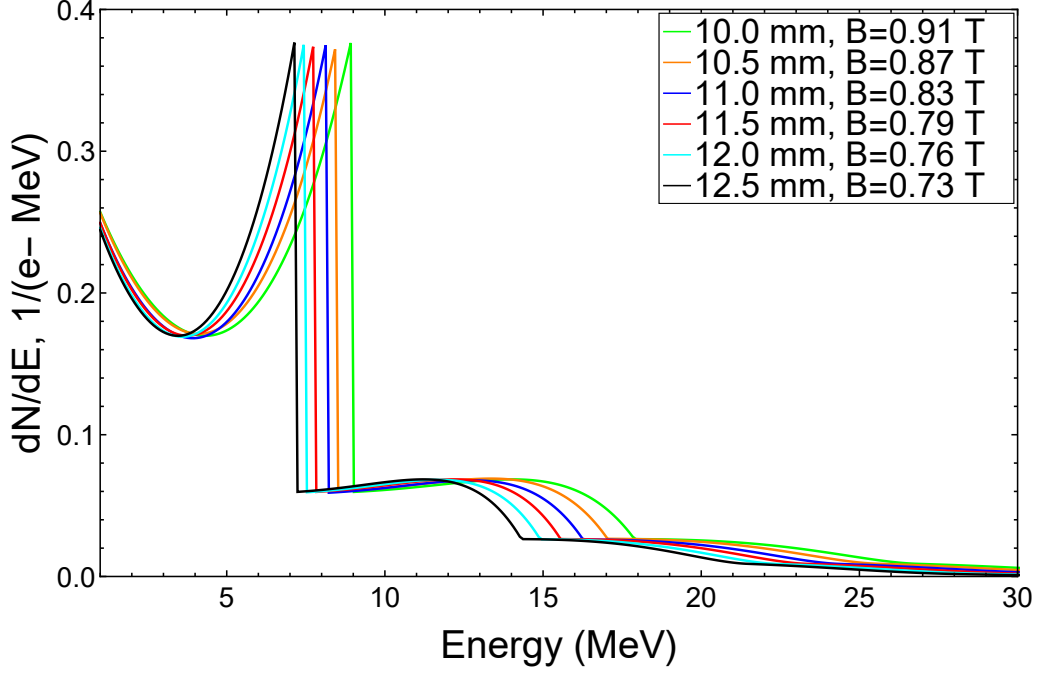


Figure 5.3: Photon spectrum created by a 1.75 m helical undulator length using different period sizes $\lambda_u = 10.0, 10.5, 11.0, 11.5, 12.0$ and 12.5 mm. The undulator length and K value ($K=0.85$) are fixed. It means that when $\lambda_u = 10.0$, the period number is 175 and B-field = 0.91 T, and when $\lambda_u = 12.0$, the period number is 146 and B-field = 0.72 T. The electron energy is $E_e = 125$ GeV.

5.2.1.3 Electron Beam Energy

The electron beam energy (E_e) also affects the shape of the photon spectrum. Equation 5.32 is used to calculate the photon spectrum created by a helical undulator with different electron beam energies. Figure 5.4 shows the spectrum of the photon beam produced by a 1.75 helical undulator for different E_e such as 125, 175 and 250 GeV but with the same parameters such as $K = 0.85$ and $\lambda_u = 11.5$ mm.

However, the produced photon number is stable. Increasing E_e will increase the average energy and power of the photon beam, which will increase the probability of producing positrons.

5.2.2 Angular Power Distribution

The angular power distribution produced by a helical undulator with $N > 100$ can be calculated by integrating equation 5.26 over all frequencies and is given by [45]:

$$\frac{dW}{d\Omega} = \frac{2Nq^2\omega_0\gamma^4K^2}{\pi\epsilon_0c(1+K^2+\gamma^2\theta^2)^3} \sum_{n=1}^{\infty} n^2 \left[J_n'^2(x_n) + \left(\frac{\gamma\theta}{K} - \frac{n}{x_n} \right)^2 J_n^2(x_n) \right] \quad (5.36)$$

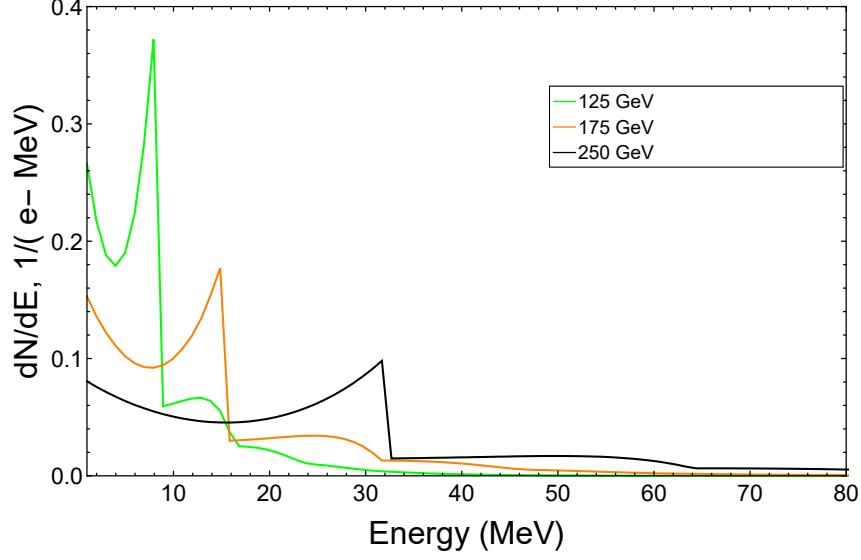


Figure 5.4: Photon spectrum created by a 1.75 m undulator length using different electron energies $E_e = 125, 175$ and 250 GeV. The undulator length, $K=0.85$ and $\lambda_u = 11.5$ mm are fixed.

Where:

$$x_n = \frac{2nK\theta\gamma}{1 + K^2 + \gamma^2\theta^2}, \quad (5.37)$$

$$\theta = \frac{1}{\gamma} \left[n \frac{\omega_1(1 + K^2)}{\omega} - 1 - K^2 \right] \quad (5.38)$$

Figure 5.5 shows the power distribution of photons for the first five harmonics produced by a 1.75 m helical undulator module with $K=0.85$, $\lambda_u = 11.5$ mm and 125 GeV electron beam. The

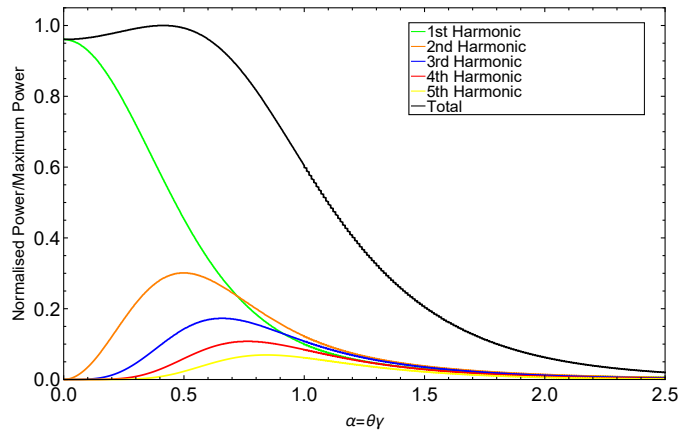


Figure 5.5: Angular power distribution in the first five harmonics produced by the ILC undulator with $K = 0.85$, 125 GeV electron beam and 152 periods.

different harmonics have been plotted separately to show how the significance of the higher harmonics decreases. Figure 5.6 represents the angular distribution of the radiation power produced by a 1.75 m helical undulator with $\lambda_u = 11.5$ mm and $E_e = 125$ GeV for different K values. The significance of the higher K value is shown.

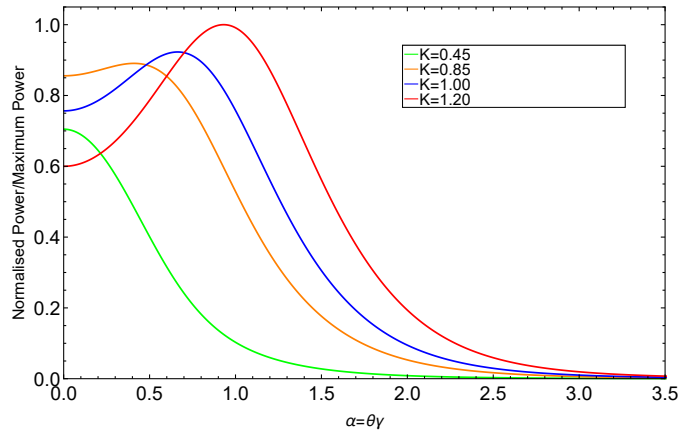


Figure 5.6: Angular power distribution produced by a 1.75 m helical undulator with $\lambda_u = 11.5$ mm and $E_e = 125$. Each color represents the power distribution of the ILC helical undulator with different K values.

The photon peak distribution is not on the axis. And by increasing the K value, the peak moves further from the axis, which will affect the positron distribution.

5.2.3 Photon Beam Polarization

Stokes parameters can be used to give a description of the polarization state of the electromagnetic radiation. The stokes parameters is introduced in appendix A. The polarization of an electromagnetic wave can be described by the relationship between two orthogonal components of, for instance, the B-field:

$$B_x = B_{x0} \cos(\omega t) \quad (5.39)$$

and

$$B_y = B_{y0} \cos(\omega t + \delta) \quad (5.40)$$

So, there are three independent parameters: the field amplitudes (B_{x0} and B_{y0}) and the phase difference δ .

When the phase difference is zero or 45° the light is linearly or elliptically polarized. When the phase difference is $\frac{\pi}{2}$ and $B_{x0} = B_{y0}$, the light is circularly polarized. The helical undulator generates

a photon beam that is circularly polarized. This is significant because the positron beam produced by this photon beam will inherit the polarization of the photon beam. The schematic of the helical undulator-based positron production process has been seen in figure 4.2. If we consider an ideal helical undulator, its horizontal and vertical fields on-axis with a variable phase difference between them are written as follows:

$$B_x = B_{x0} \sin\left(\frac{2\pi z}{\lambda_u} - \delta\right) \quad (5.41)$$

$$B_y = B_{y0} \sin\left(\frac{2\pi z}{\lambda_u}\right) \quad (5.42)$$

The electron velocities in the two planes can be written as follows:

$$\beta_x = \frac{K_y}{\gamma} \cos\left(\frac{2\pi z}{\lambda_u}\right) \quad (5.43)$$

$$\beta_y = \frac{K_x}{\gamma} \cos\left(\frac{2\pi z}{\lambda_u} - \delta\right) \quad (5.44)$$

The K_y and K_x are shown in equations 5.18 and 5.19, respectively. For the first harmonic and small K_y and K_x , the circular polarization rate (P_3) can be expressed as follows:

$$P_3 = \frac{2B_{x0}B_{y0} \sin \delta}{B_{x0}^2 + B_{y0}^2} \quad (5.45)$$

As mentioned above, the polarization can be specified by only three independent variables: the field amplitudes and the phase difference. $P_3 = 0$, when B_{x0} and B_{y0} are in phase, which is a linearly polarized wave. While $P_3 \pm 1$, when $B_{x0} = \pm iB_{y0}$. The first term in square brackets in equation 5.26 corresponds to one component of the B-field, whereas the second term corresponds to the perpendicular component. This enables us to calculate the polarization of the radiation produced by an electron beam passing through a helical undulator as a function of the frequency and angle with respect to the undulator axis:

$$P_3 = \frac{S_3}{S_0} \quad (5.46)$$

Where

$$S_3 = -2 \sum_{n=1}^{\infty} \left[J'_n(x) \left(\frac{\theta\gamma}{K} - \frac{n}{x} \right) J_n(x) \right] \frac{\sin^2 \left[N\pi \left(\frac{\omega}{\omega_1} - n \right) \right]}{\left(\frac{\omega}{\omega_1} - n \right)^2} \quad (5.47)$$

and

$$S_0 = \sum_{n=1}^{\infty} \left[J_n^2(x) + \left(\frac{\theta\gamma}{K} - \frac{n}{x} \right)^2 J_n^2(x) \right] \frac{\sin^2 \left[N\pi \left(\frac{\omega}{\omega_1} - n \right) \right]}{\left(\frac{\omega}{\omega_1} - n \right)^2} \quad (5.48)$$

Figure 5.7 shows the photon spectrum and the circular polarization rate of the photon beam as a function of energy (integrated over all angles) of radiation from a helical undulator with a 1.75

m length, $K = 0.85$, $\lambda_u = 11.5$ mm and $E_e = 125$ GeV. The photon beam polarization rises as the photon beam energy approaches the harmonic cut off before dramatically dropping at the cut off. The maximum opening angle included in this figure is $12 \mu rad$.

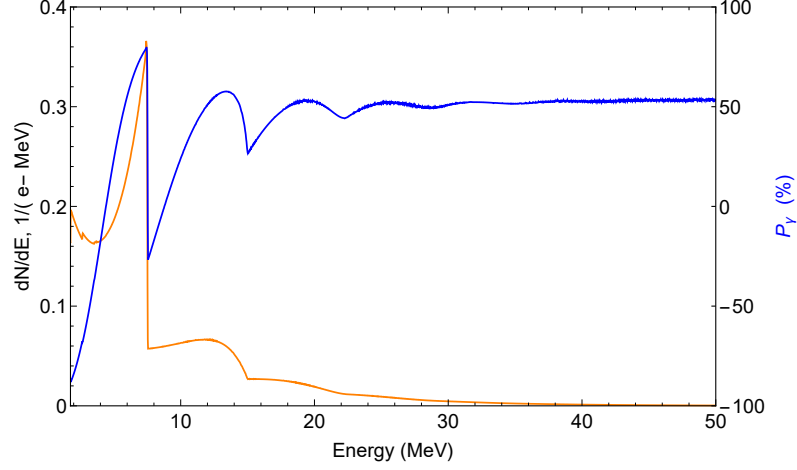


Figure 5.7: Photon beam spectrum and polarization created by a 1.75 m helical undulator with $K = 0.85$ ($\lambda_u = 11.5$ mm) and $E_e = 125$ GeV.

Since the circularly polarized photon beam will be directed to a target to produce a longitudinal polarized positron beam, the degree of the positron beam polarization depends on the degree of the photon beam polarization, photon energy and the pair production cross section. As shown in equations 5.29 and 5.38, the frequency of the radiation and the angle at which it is emitted have a strong correlation as photons with low frequency (low energy) have larger opening angles. Therefore, the average polarization of the photon beam can be controlled by removing photons with low energy (large angles) for which the polarization varies over a wide range.

Figure 5.8 shows the photon beam spectrum and polarization produced by a helical undulator module with 1.75 m length, $\lambda_u = 11.5$ mm, $K = 0.85$ and $E_e = 125$ GeV. Each color represents a different maximum opening angle (θ_{Max}) that is included in the calculation. Different θ_{Max} s are chosen to show how the significance of the included θ_{Max} is on the spectrum and polarization of the photon beam.

The chosen θ_{Max} impacts the photon number ($N\gamma$), average energy (E_{ave}^γ) and polarization (P_γ) of the photon beam. Table 5.1 summarizes the results. However, the average energy and polarization of the photon beam increase. The photon number decreases when a small θ_{Max} is considered.

In section 5.2.1.1, we saw the effect of the K value on the photon spectrum number. Here we will investigate the effect of K value on the photon beam polarization. Figure 5.9 shows the photon beam polarization produced by a 1.75 m undulator length with $\lambda_u = 11.5$ mm, $\theta_{Max} = 14.6 \mu rad$ and $E_e = 125$ GeV for different K values.

The positron beam polarization is discussed not in terms of the peak polarization but in terms of

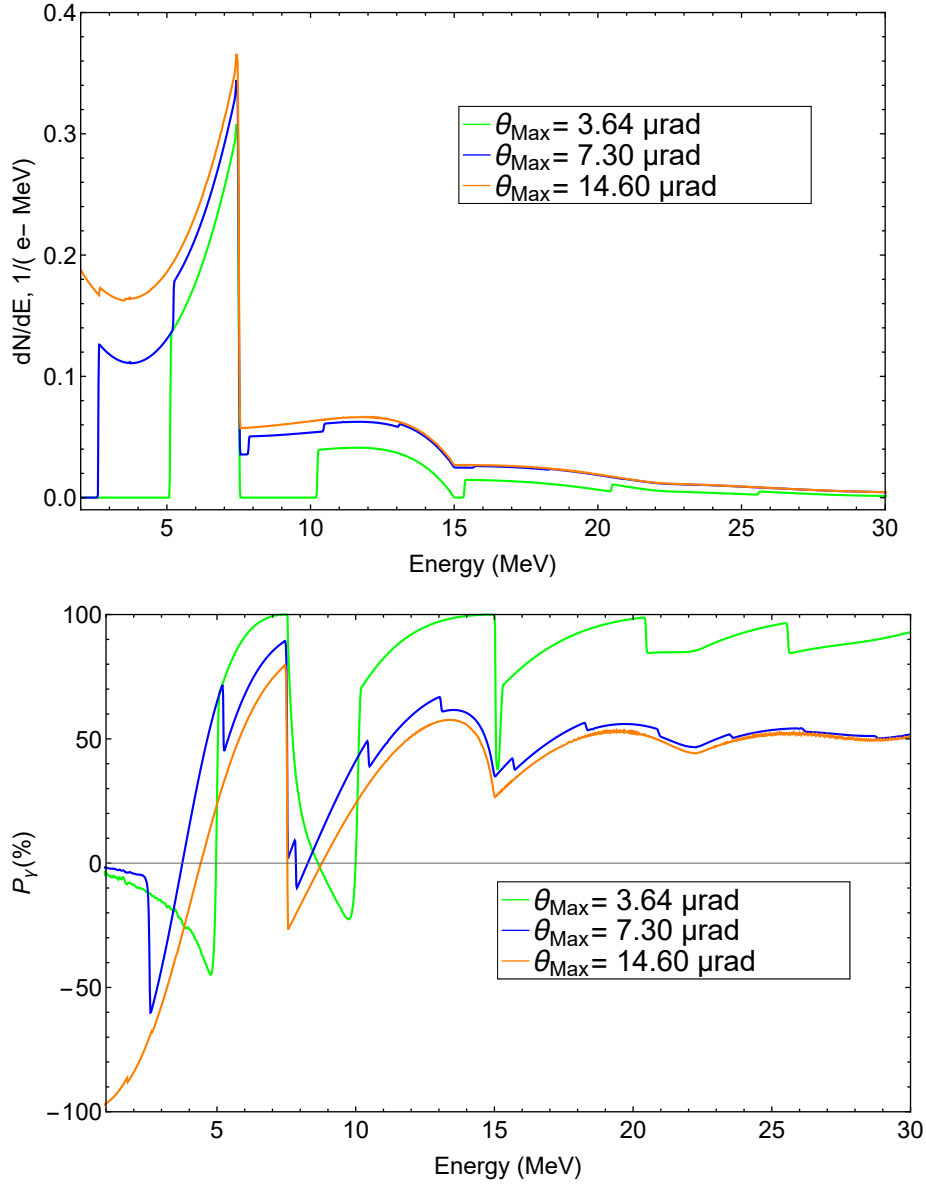


Figure 5.8: Spectrum (top) and circular polarization (bottom) of the photon beam with different maximum opening angle θ_{Max} produced by a 1.75 m helical undulator length with $K = 0.85$ ($\lambda_u = 11.5$ mm) and $E_e = 125$ GeV. Each color represents a different included θ_{Max} .

Table 5.1: The number (N_γ), average energy (E_{ave}^γ), polarization (P_γ) of the photon beam using three different maximum opening angle (θ_{Max}) produced by a helical undulator with a 1.75 m length (152 periods), $\lambda_u = 11.5$ mm and $K=0.85$, which is being passed by E_e of 125 GeV. Distance between this undulator module exit and observation points is 401 m.

θ_{Max} (μrad)	N_γ (photons/e/1.75 m)	E_{ave}^γ (MeV)	P_γ (%)
3.64	0.76	10.0	91.5
7.30	1.52	9.9	53.0
14.60	2.01	8.2	37.7

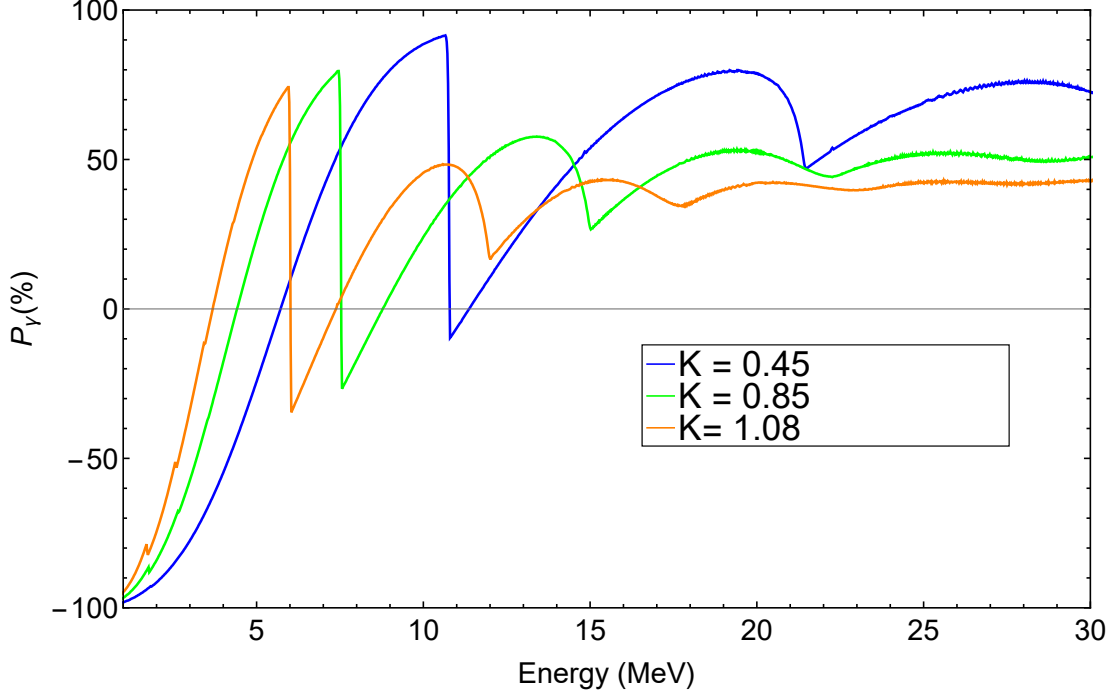


Figure 5.9: Photon beam polarization produced by a 1.75 m undulator length with $\lambda_u = 11.5$ mm for different K values and $E_e = 125$ GeV. Each color represents a different K value. The considered θ_{Max} is $14.6 \mu rad$.

the average polarization in a positron bunch. Therefore, not only the value of the peak polarization of the photon beam is crucial, but also the spread in the photon beam polarization. As shown in figure 5.9, the helical undulator with higher K value produces lower photon beam polarization while helical undulator with small K value produces a higher photon beam polarization. The average photon beam polarization with $\theta_{Max} = 14.6 (\mu rad)$ for $K = 0.45$ is 46 % while it is only 37.7 % and 33.5 % for $K = 0.85$ and 1.08, respectively.

Chapter 6

The ILC Helical Undulator

The positron source is one of the challenging areas for any high-intensity future electron-positron colliders. Since a very high-intensity positron beam with $\approx 2 \times 10^{14}$ positrons per second is required at the IP of the ILC, a very high-intensity photon beam with $\approx 5.25 \times 10^{16}$ photons per second are needed to produce this amount of positrons. The TDR of the ILC has chosen the helical undulator as the ILC photon source. The basics of the helical undulator were introduced in the chapter 5. In this chapter the helical undulator as a photon source for the ILC is discussed in terms of structure and parameters to ensure that the ILC helical undulator can create the required photon beam that can produce the required positron beam. In addition, the aim of the thesis is shown at the end of this chapter.

6.1 The ILC Helical Undulator Prototypes

A prototype study is crucial in validating design decisions before development starts. The aim is to give the developers a chance to identify problems so that they can make the necessary changes prior to developing and building their product. As discussed in section 4.1.2, a high-energy multi-GeV electron beam should pass through a helical undulator with a high magnetic field, a short period, and a small aperture to generate a high power multi-MeV photon beam in order to produce the required positron yield. The first suitable cryomodule prototype of the ILC has been demonstrated at Rutherford Appleton Laboratory [35]. Figure 6.1 shows photographs of these prototypes.

The left plot in figure 6.1 shows four short undulator prototypes and the right plot shows the two superconducting helical undulator prototypes with a 1.74 m length for each inserted into a cryomodule with 4.1 m long. These prototypes were built to get the expected size of the errors in the B-field of the helical undulator modules that would be used in the ILC helical undulator-based positron source. Hall probes, a device used to measure the magnetic field, were used to measure

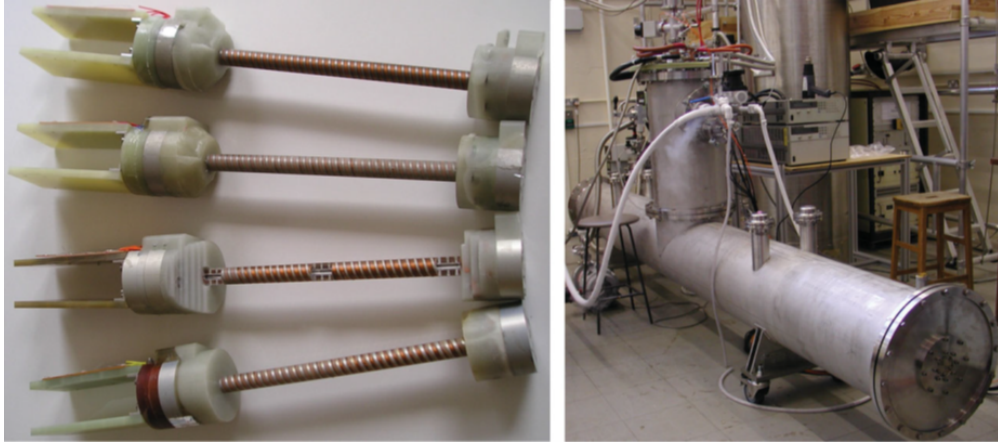


Figure 6.1: The left photograph shows four short undulator prototypes. The right photograph shows a 4.1 m long cryomodule prototype, containing two undulator modules with a 1.74 m length for each [35].

the magnetic field of the two helical undulator prototypes. The upper plot in figure 6.2 shows the K value per period for both helical undulator prototypes. The bottom plot shows the ideal and measured photon number spectrum per electron.

The prototype studies have shown that the error size in the second undulator prototype is larger than in the first undulator prototype. This difference is likely due to some errors in the winding during the construction. In addition, these studies have shown that superconducting undulators with λ_u of 11.5 mm and K factors up to 0.92 are possible. More detail about the study of the helical undulator prototypes can be found in [35].

6.2 The Structure of the ILC Undulator Line

The first stage of the ILC is to operate at 250 GeV centre-of-mass energy. The later stages upgrade the centre-of-mass energy to 350 GeV and 500 GeV. That means that the linacs of the electron and positron accelerate the electron and positron beams up to their collision energy of between 125 GeV and 250 GeV. Therefore the helical undulator must produce usable photons from the electron drive beam with energy between 125 GeV and 250 GeV and higher.

Nevertheless, the complete ILC helical undulator would contain a series of cryomodules with 4.1 m long. Each cryomodule contains two superconducting helical undulator modules with a length of 1.75 m length and λ_u of 11.5 mm. To focus and steer the electron beam through the undulator, quadrupoles are placed after every three cryomodules. Figure 6.3 shows the schematic layout of the ILC undulator line.

In total, twenty-two copies of such depicted in this scheme are needed for the ILC-250, which means that the ILC undulator would consist of 66 cryomodules and 22 quadrupoles.

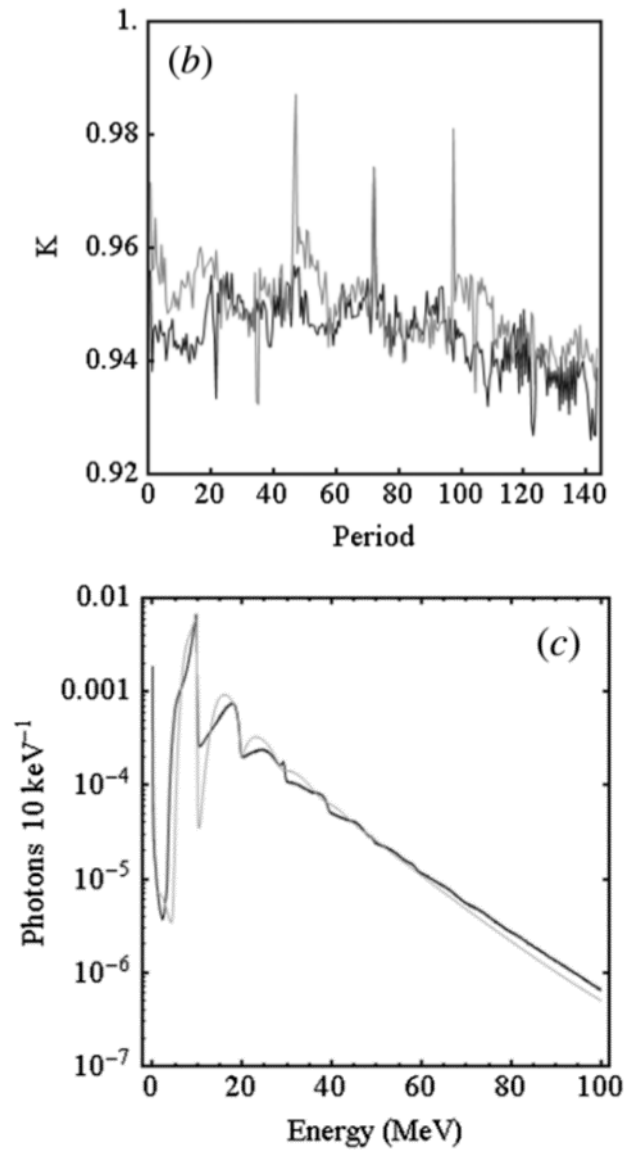


Figure 6.2: Upper plot shows K value per period for first (black lines) and second (gray lines) undulator prototypes. The bottom plot shows the ideal (gray lines) and measured (black lines) number of photons per electron per 10 keV bandwidth [35].

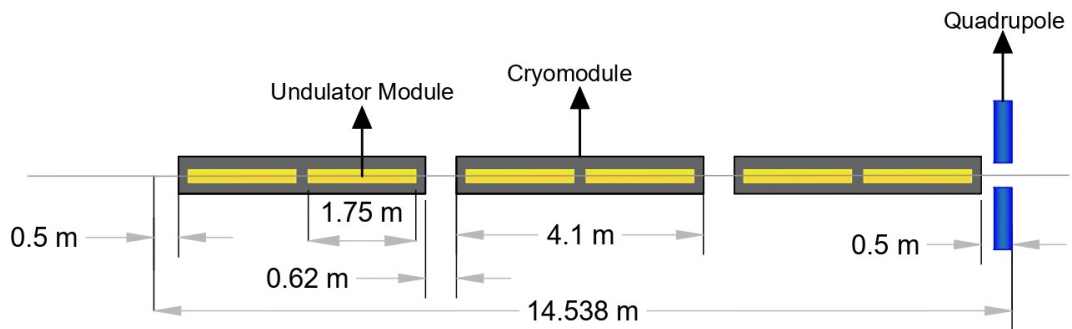


Figure 6.3: Schematic layout of the ILC undulator line.

Since the first stage in the ILC is 250 GeV centre-of-mass energy, the full active length is needed to create the required positron yield ($1.5 e^+/e^-$) at the positron DR. The active length of the ILC-250 helical undulator is ≈ 231 m, and the total length is ≈ 320 m. For 350 or 500 GeV centre-of-mass energy, only 42 cryomodules are required to create the required positron yield.

Table 6.1 shows the parameters of the ILC helical undulator structure line that are required to produce the required positron yield for each stage, taken from [11, 46].

Table 6.1: The parameters of the ILC helical undulator structure line are taken from [11] and [46].

Parameters	Values			Unit
Undulator aperture	5.85			mm
Undulator period	11.5			mm
Period number in an undulator	152			
Effective undulator length	1.75			m
Undulator number in a cryomodule	2			
Cryomodule length	4.1			m
Quadruple length	1			m
Quadruple spacing	14.538			m
Centre-of-mass energy	250	350	500	GeV
Required undulator B-field	0.79	0.698	0.42	T
Undulator K value	0.85	0.75	0.45	
Required number of undulators	132	84		
Required number of cryomodules	66	42		
Total active required undulator length	231	147		m
Total length of undulator line	319.84			m
Distance from middle of undulator to the target	401.10			m
Distance from undulator exit to the target	241.18			m

6.3 Thesis Aims

Since a very high-intensity positron beam with $\approx 2 \times 10^{14}$ positrons per second are required at the IP of the ILC, a very high-intensity photon beam with $\approx 5.25 \times 10^{16}$ photons per second are needed to produce this amount of positrons. In order to produce this amount of photons, the helical undulator-based positron source is used. There are important challenges for this source:

- In order to produce a very high-intensity photon beam, the helical undulator must be long enough. The total ILC undulator length is ≈ 320 m. The photons are created with an opening angle in the helical undulator, and part of these photons will hit the very long superconducting undulator walls. The incident power at the undulator walls must be studied to ensure it is below the acceptable level of 1 W/m [27].

- To keep the incident power below the acceptable level, photon masks must be placed along the undulator line. These masks should be designed to protect the undulator walls and meet the required vacuum level. At the same time, enough photons must pass through these masks to the target to generate the required positrons.
- The energy deposition, temperature rise, and stress at the photon masks will be studied to check if values are still below the limit.
- After designing the masks, the effects of these masks on the photon beam distribution and polarization at the target plane should be checked.
- Since building an ideal undulator to generate a perfect photon distribution is impossible, the realistic photon beam distribution and polarization at the target plane must be studied. The realistic studies here are based on the helical undulator prototype studies in [35].

Finally, this photon distribution can be used to check the realistic efficiency of the e^+ production. All these studies are done for the three stages of the ILC (ILC-250, ILC-350, and ILC-500).

Chapter 7

Simulating Helical Undulator

Photon Spectra

There are a few simulation codes that are used to calculate the photon spectra that are expected from a helical undulator. The FluxCalc is a Mathematica notebook and was developed by Duncan Scott at STFC Daresbury Laboratory in the UK to calculate the Synchrotron Radiation (SR) created by a helical undulator. SPECTRA code, which is a C++ based code developed by Takashi Tanaka at the SPring-8 Center is one of the most widespread codes that is used to calculate the expected SR created by a helical undulator [47]. The accuracy of the SPECTRA was tested by simulating the photon spectrum that is expected from the helical undulator prototypes demonstrated at Daresbury Laboratory and Rutherford Appleton Laboratory and there were some issues that arose during this test. One of these issues was the length of the time that is required to simulate the photon spectrum and the photon spectrum accuracy at wide angles. Therefore, it was subsequently required to develop a new simulation code that can simulate the photon spectrum created by the helical undulator-based positron source. Therefore, the Helical Undulator Synchrotron Radiation (HUSR) code was developed.

This chapter shows a comparative study between these three codes. The best suited code for our task is then discussed with more detail and benchmarked for both ideal and non-ideal helical undulator cases.

7.1 Simulation Methods

Possible methods for simulating the SR are the FluxCalc, SPECTRA and HUSR codes. The FluxCalc, which was developed by Duncan Scott, is a Mathematica notebook that can calculate the SR

produced when an electron traveling through a helical undulator field map. SPECTRA code is a code that can calculate various characteristics of SR and was developed in Japan and described in [47]. HUSR is a C++ code and was developed by David Newton [48, 49, 50]. HUSR was developed to simulate the SR output from the prototype helical undulators built at the Cockcroft Institute of accelerator science and technology in the UK [35].

Duncan Scott conducted a comparative study between these three codes to determine the differences between these codes and their results [51]. Table 7.1 shows the undulator parameters used in this comparative study. The used parameters are close to the required helical undulator parameters of the ILC TDR positron source. The main difference is that the number of the undulator periods is much lower; here it is 10 periods while in the ILC TDR is over 150 periods.

Table 7.1: The undulator parameters used in the comparison between FluxCalc, HUSR and SPECTRA [51].

Parameters	Values	Unit
Electron beam energy	150	GeV
Undulator period (λ)	10.0	mm
Number of periods	10.0	
Undulator B-field	1.07	T
Distance to aperture	10.0	m
Undulator K	1.0	
Aperture area	1.0	mm^2

Figure 7.1 shows the results of this study. All these codes have a good agreement in the region below 30 keV. The SPECTRA code no longer agrees with the HUSR and FluxCalc codes in the region above 30 keV. Based on the results seen in figure 7.1, the HUSR and FluxCalc codes were the best candidates to be used for calculating the photon spectrum output from the helical undulator-based positron source.

With regard to functionality, speed of calculation and ease of modification, a comparison study had been conducted between HUSR and FluxCalc to determine which one would be better appropriate to be used to simulate the photon spectrum output from the undulator-based positron source. In terms of functionality, the study showed that there were more scope for extending the functionality with HUSR compared with FluxCalc. Furthermore, the functionality of HUSR would be easier to be extended as HUSR is a C++ code. With regard to the speed of calculation, HUSR had this advantage. This study concluded that HUSR is a better candidate to be used for simulating the photon spectrum created by the helical undulator. In addition, not only HUSR can calculate the ideal photon spectrum, but also the non-ideal photon spectrum. Furthermore, HUSR can calculate the photon beam polarization.

Due to the death of David Newton, HUSR could not be finally described by a journal article

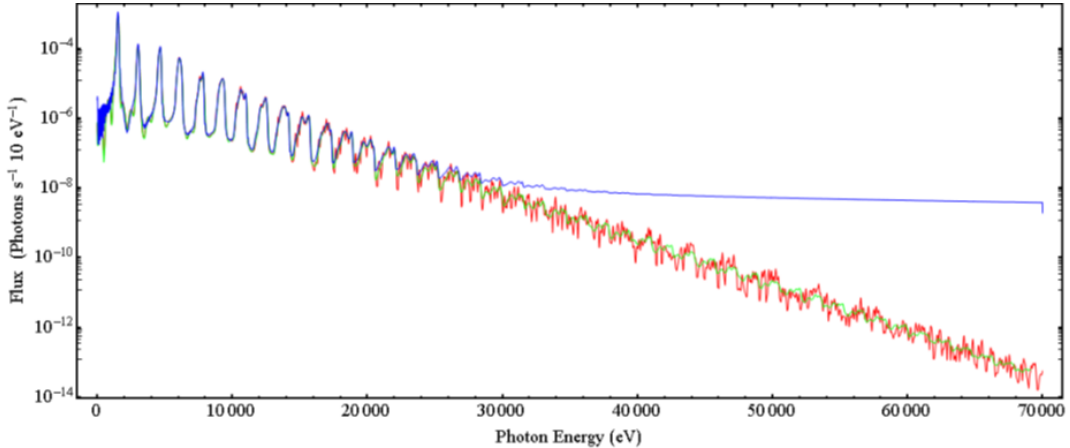


Figure 7.1: Comparison between the photon flux produced by a single electron passing through a 1 mm^2 helical undulator aperture calculated by SPECTRA (Blue line), FluxCalc (red line) and HUSR in (green line) [51].

or paper, but it was used and tested by developers at the Cockcroft Institute of accelerator science and technology in the UK. Some previous helical undulator studies [51, 52] were done by using the HUSR code.

7.2 HUSR Simulation

The HUSR code calculates a Lie Map from a given magnetic field. It happens by interpolating the data of the given magnetic field on the surface of a cylinder. Lie maps which represent a small step in the period of the helical undulator are created by numerically integrating the Hamiltonian of an electron [53, 49]. In order to increase the accuracy of tracking a particle inside the magnet system, the number of integration steps used in this study in each Lie Map is over 10^6 steps. Each Lie map which is a transfer map provides the new coordinates of a particle in the phase space. After creating the Lie Maps, the spectrum is calculated at the observation points that are set at an appropriate distance after the exit of the helical undulator module. In order to do this, the electric field at each observation point is calculated using the retarded potential. Then from the retarded potential, the electric field as a function of the time domain is calculated at each observation point. In order to change from the time domain to the frequency domain, the field is Fourier transformed.

Since, the photon beam produced in the helical undulator has a circular polarization, each observation point will recognize if the observer at this observation point sees whether the spins of these photons are right-handed or left-handed. If the direction of the photon spin is the same as the direction of its motion, the photon is right-handed. If the directions of spin and motion of the photon are opposite, then the photon is left-handed. Therefore, in the output file, there are two columns. One column is for the photon number with the left-handed spins, and another is for the

photon number with the right-handed spins at each observation point.

In the thesis, 1000 energy bins of equal size over the energy range between 0.2 MeV and 200 MeV are used when the radiation spectrum is calculated. The dimension of the target plane can be chosen and the number of the observation points which have the same size over the target plane. The HUSR code considers the electron as a pencil-like beam. That is acceptable since the initial electron beam spot size of the ILC is too small, $\sigma_x = 37 \mu\text{m}$ and $\sigma_y = 2.4 \mu\text{m}$ [54]. The HUSR code can calculate the photon spectrum produced by both ideal and non-ideal (realistic) undulators. The flowchart in figure 7.2 summarizes the steps of the process in the HUSR for both ideal and realistic undulator cases. These steps will be discussed in more details in the following sections.

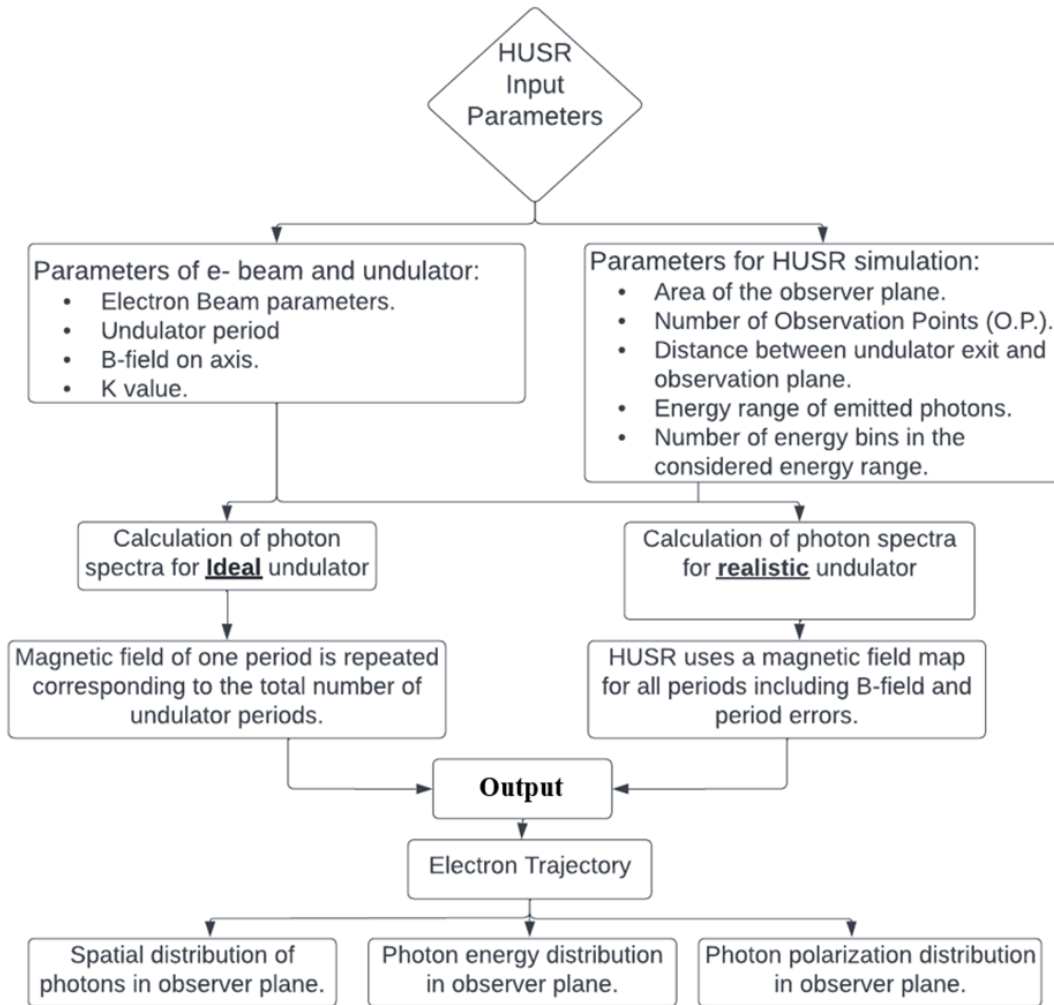


Figure 7.2: flowchart shows the steps of the process in the HUSR for both ideal and realistic undulator cases.

7.2.1 Tracking an Electron Through an Ideal Field Map

In the ideal case (Ideal magnetic field map), the HUSR uses one period as shown in figure 7.3 and 150 equal steps are used along this period. Then the Lie Maps of this period will be used many time in order to have the overall undulator length. For instance, if $\lambda_u = 11.5$ mm, the Lie Maps for this period will be used 152 times for simulating one ILC helical undulator which has a length of 1.75 m. The magnetic field inside the ideal helical undulator is described by equations 5.12 and 5.13. The beam is injected on-axis at an angle that ensured the beam exits the helical undulator on-axis with no tapering in the ideal magnetic field map.

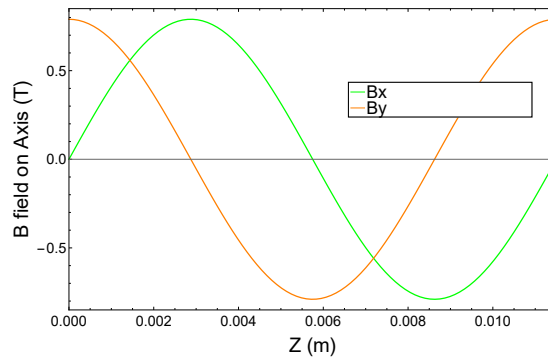


Figure 7.3: Ideal magnetic field of the helical undulator parameters, $\lambda_u = 11.5$ mm and $K=0.85$.

In the case of an ideal undulator, the electron would experience an average magnetic field strength of zero and move through the undulator with a total deflection of zero. According to the equation 5.26, an electron in the helical undulator that is injected on axis will move in a helical pattern. Considering an helical undulator with a 1.75 m length, $K = 0.85$ and $\lambda_u = 11.5$ mm, figure 7.4 present the position of the electron of 125 GeV on the x and y axis in the case of an ideal helical undulator.

7.2.2 Tracking an Electron Through a Realistic Field Map

The ideal photon spectrum is created by an ideal helical undulator. Since it is impossible to build an ideal helical undulator, it is an interesting and useful to study the non-ideal (realistic) photon spectrum that is produced by a realistic helical undulator. One benefit of using HUSR code in this thesis is its ability to simulate the realistic photon spectrum of the ILC. This can be done by introducing random errors into each period in the undulator magnetic field map. In the ideal case, HUSR constructs the overall field map by using a single undulator period as discussed earlier, while in the realistic case HUSR uses the realistic magnetic field map where each period has a different random error distribution.

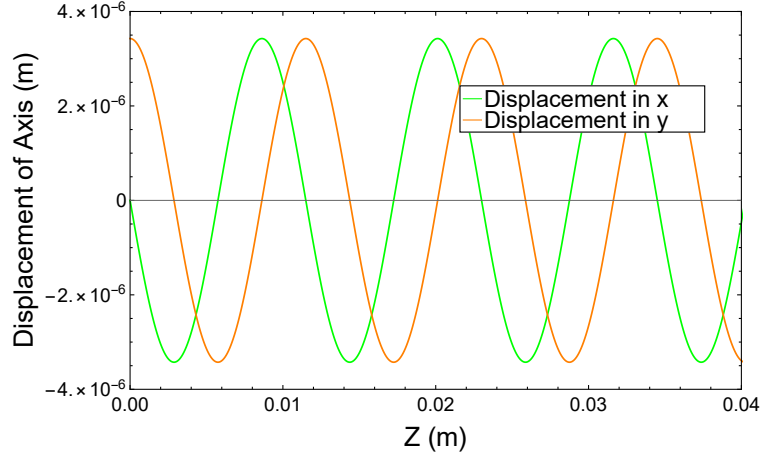


Figure 7.4: Displacement of a 125 GeV electron through first 3 periods of the Ideal helical undulator of the ILC with a $K = 0.85$ and $\lambda_u = 11.5$ mm.

I added the errors of the field ($\sigma_B(z)$) and the error of the period ($\sigma_\lambda(z)$) to the value of the field strength and period size, respectively, into equations 5.12 and 5.13. The model ensures that there will be no discontinuities in the realistic map. By adding $\lambda_u + \sigma_\lambda(z)$, $B_{x0} + \sigma_{B_{x0}}(z)$ and $B_{y0} + \sigma_{B_{y0}}(z)$ into the ideal equations 5.12 and 5.13 instead of λ_u , B_{x0} and B_{y0} , the magnetic field inside a realistic helical undulator can be described by the following equations:

$$B_x = (B_{x0} + \sigma_{B_{x0}}(z)) \sin \frac{2\pi z}{(\lambda_u + \sigma_\lambda(z))} \quad (7.1)$$

$$B_y = (B_{y0} + \sigma_{B_{y0}}(z)) \cos \frac{2\pi z}{(\lambda_u + \sigma_\lambda(z))} \quad (7.2)$$

Figure 7.5 shows an example of the realistic magnetic field of the helical undulator parameters with 1.75 m long, $\lambda_u = 11.5$ mm and $K = 0.85$ with a tapering in the B-field in the first and last two periods.

In order to get the expected size of the errors in the actual helical undulator modules that can be used in the ILC undulator-based positron source, the error sizes in the measured magnetic fields are used here. As can be seen in figure 6.2, the maximum error size in the first undulator prototype is almost $\pm 4\%$, while the error size in the second undulator prototype is higher ($\pm 10\%$). By using the HUSR, the electron is tracked in two realistic magnetic maps with the error in K of $\pm 4\%$ and $\pm 10\%$. Figure 7.6 shows the realistic K value with these errors along the realistic undulator with 1.75 m length.

When an electron moves through an ideal undulator, it moves on a helical motion around the central axis of the helical undulator with a total deflection of zero. In the non-ideal (realistic) field map case, equations 7.1 and 7.2 were used after introducing the errors in both magnetic strength and

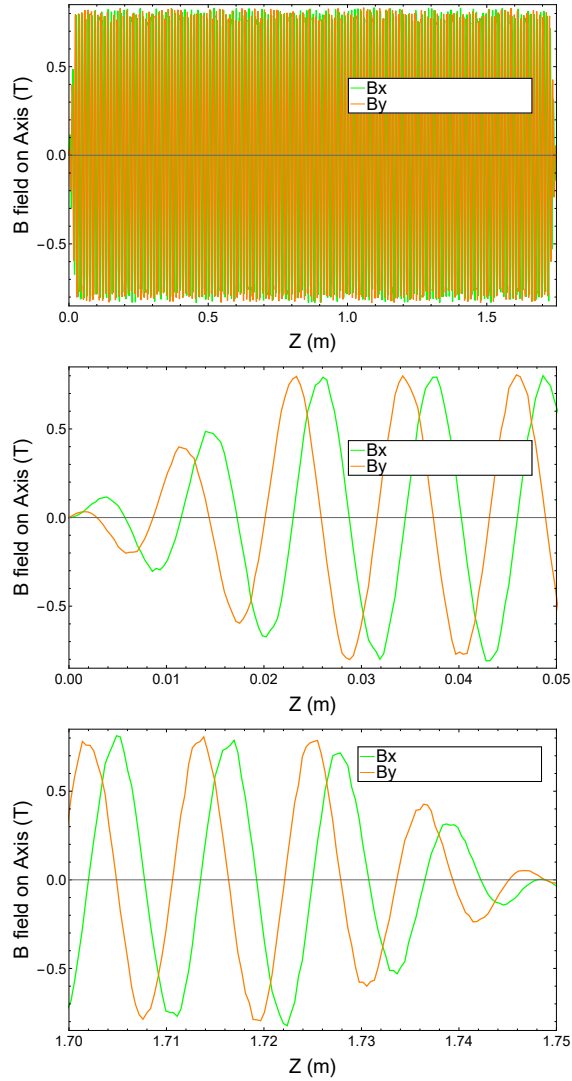


Figure 7.5: Realistic magnetic field of the helical undulator parameters, $\lambda_u = 11.5$ mm and $K=0.85$. Top plot shows the whole magnetic field of a 1.75 m helical undulator. The magnetic field at the entrance and at the exit of the undulator are shown in the middle and bottom plots, respectively.

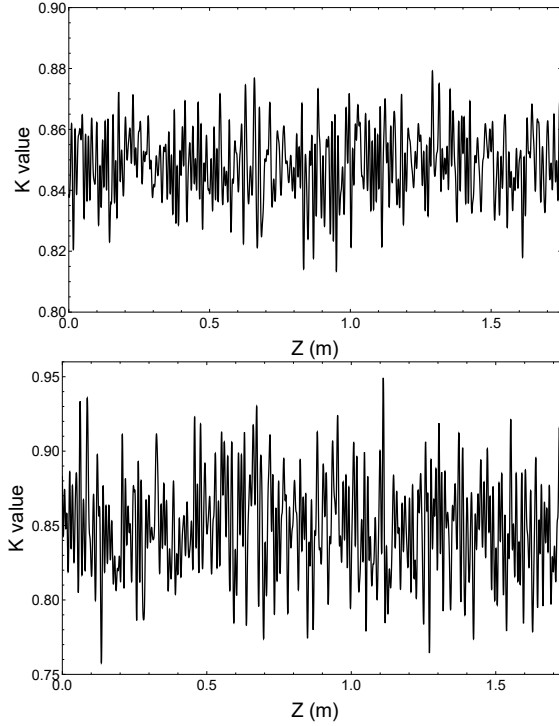


Figure 7.6: K value with errors along the realistic undulator, with helical undulator parameters of $\lambda_u = 11.5$ mm and $K=0.85$. Error in upper plot is $\pm 4\%$ while the error in the bottom plot is $\pm 10\%$.

period. In this case, the electron will experience similar errors in the realistic magnetic field map. Considering the same parameters of the ideal helical undulator such as 1.75 m undulator length, $K = 0.85$ and $\lambda_u = 11.5$ mm, figures 7.7, 7.8 and 7.9 show the full three-dimensional motion of the electron inside the realistic undulator and show the position of the electron in the x and y directions for three different electron energies including 125 GeV, 175 GeV and 250 GeV, respectively. In these figures, the same error size ($\pm 4\%$) and error distribution are used. The only different parameter in these figures is the electron energy. In the realistic case, the deviation of the electron trajectory is no longer zero, although the oscillation of the electron trajectory is close to the axis.

The radius of the electron helix is inversely proportional to the energy of the electron and this agrees with what is shown in figures 7.7, 7.8 and 7.9. Therefore, as expected the energy of the electron beam increases the radius of the helix is decreased. However the electron is injected on-axis in all cases, the position of the electron at the exit of the undulator is tens or, for a 125 GeV electron, hundreds of nanometers off the central axis and, of course, the photon spectrum of each case is based on the electron trajectory. The photon spectrum created by the realistic undulators with different electron beam energies will be discussed in chapter 9.

The deviation from the axis increases as long as the electron is traveling through the realistic helical undulators. Figure 7.10 shows the electron deviation from the axis when an electron travels through one, two and three cryomodules using $\pm 4\%$ error size in K. Figure 7.11 shows the electron

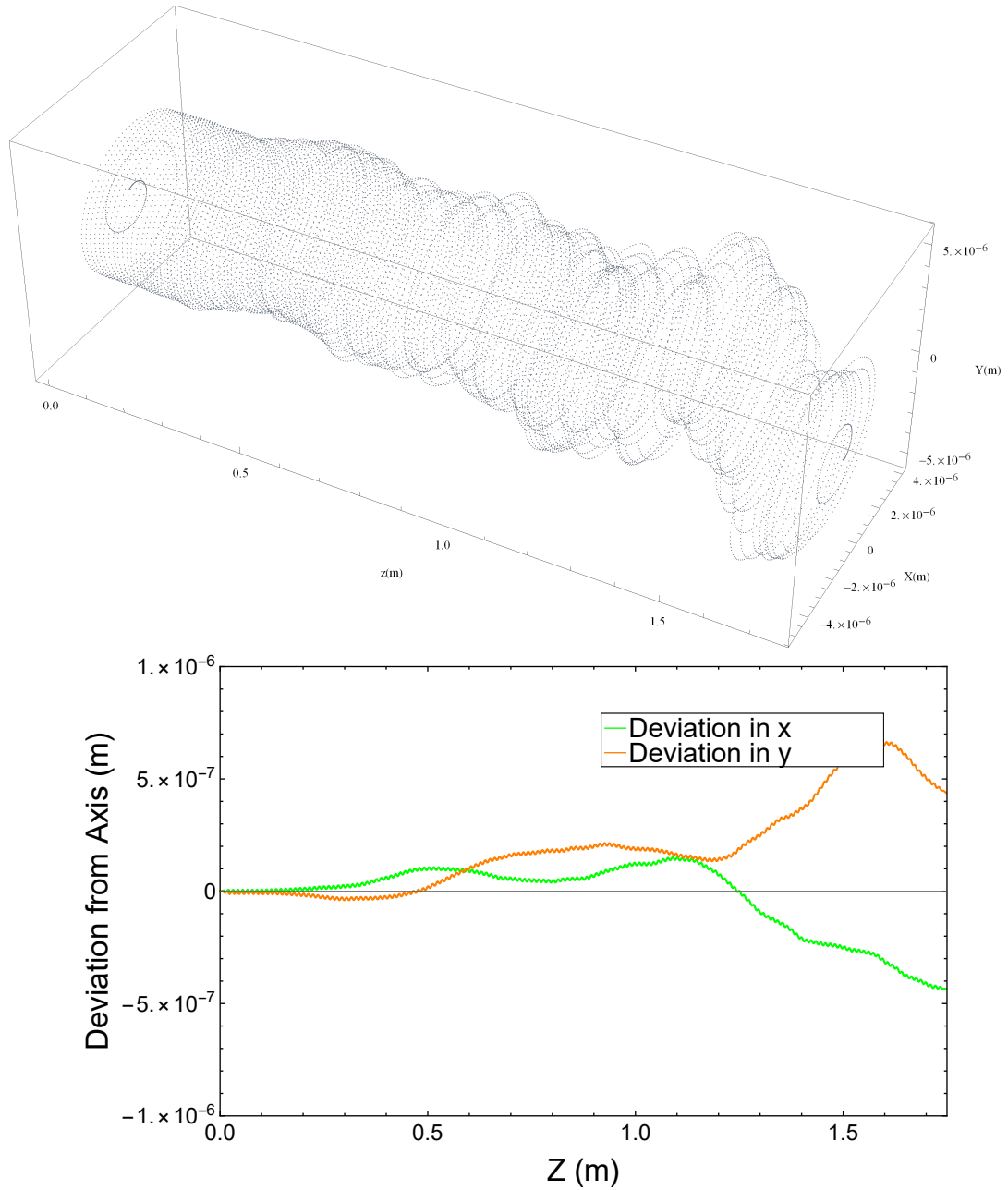


Figure 7.7: Trajectory (Upper plot) and deviation from the axis (Bottom plot) of a **125 GeV** electron traveling through a 1.75 m long realistic undulator with $K=0.85$ (0.79 T magnetic field strength) with $\pm 4\%$ error size in K . The electron is injected on axis and the realistic B-field is tapered in the first and last two periods.

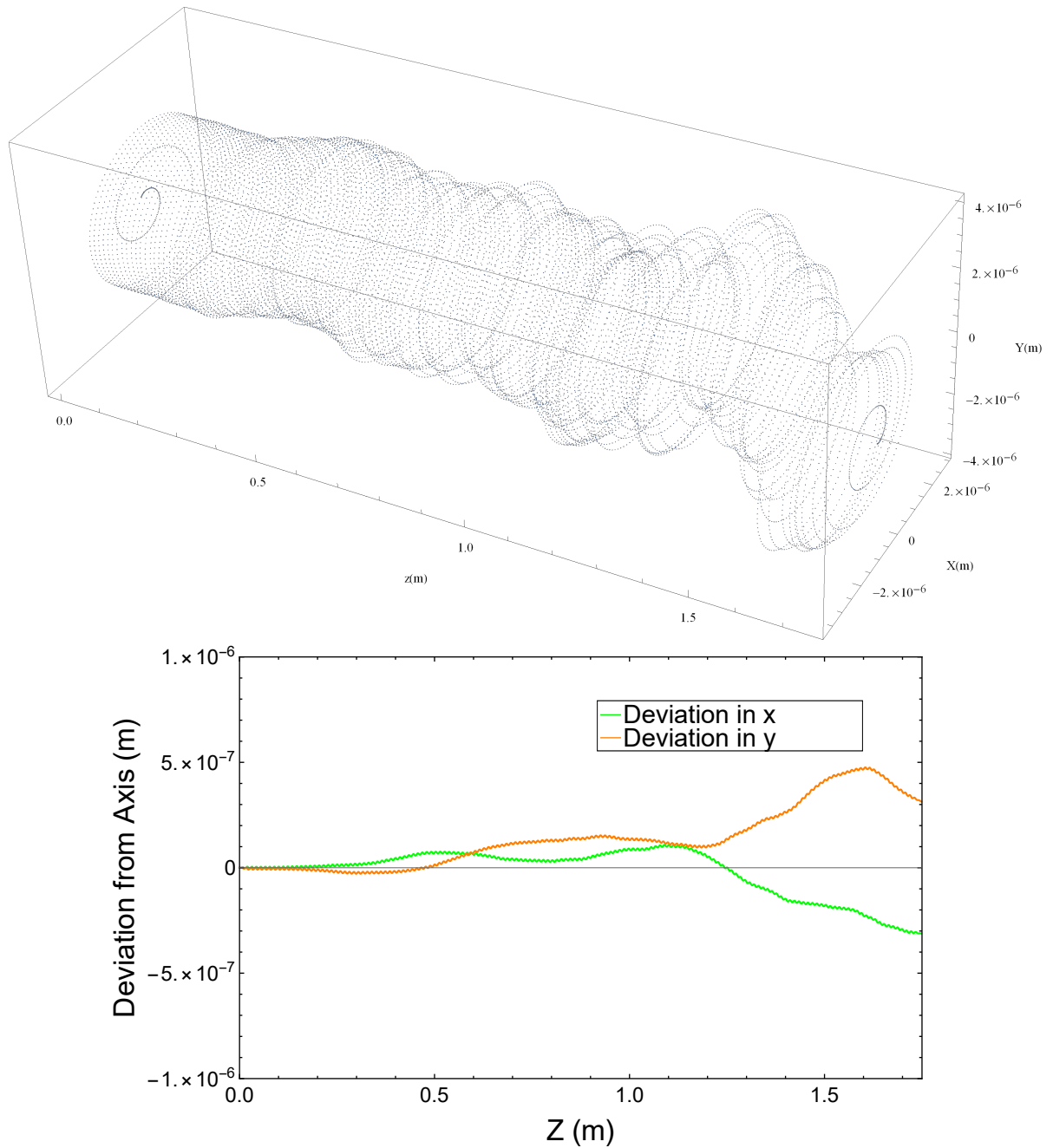


Figure 7.8: Trajectory (Upper plot) and deviation from the axis (Bottom plot) of a **175** GeV electron traveling through a 1.75 m long realistic undulator with $K=0.85$ (0.79 T magnetic field strength) with $\pm 4\%$ error size in K . The electron is injected on axis and the realistic B-field is tapered in the first and last two periods.

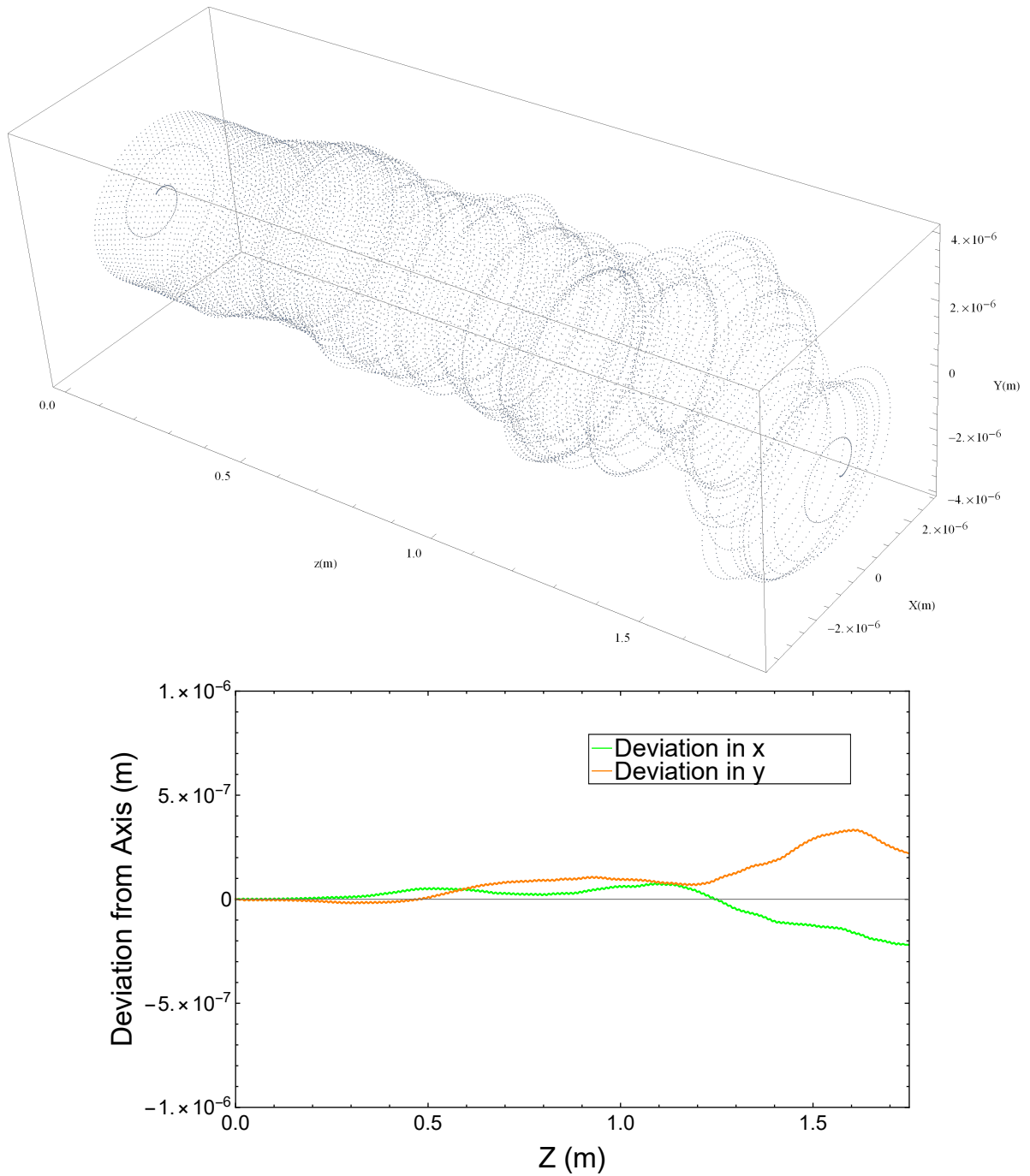


Figure 7.9: Trajectory (Upper plot) and deviation from the axis (Bottom plot) of a **250** GeV electron traveling through a 1.75 m long realistic undulator with $K=0.85$ (0.79 T magnetic field strength) with $\pm 4\%$ error size in K . The electron is injected on axis and the realistic B-field is tapered in the first and last two periods.

tracking through the whole length of the ILC undulator which was studied by Toshiyuki OKUGI, KEK [55]. In the study of Toshiyuki OKUGI, three different cases were investigated, including no correction for the electron beam, a correction for the electron beam by quadrupoles after 6 undulator modules and a correction for the electron beam by quadrupoles after each two undulator modules, respectively. There is a good agreement between the HUSR study and the study of Toshiyuki OKUGI when quadrupoles are placed after 2 and 6 undulator modules. The parameters of the ILC-250 are used in these two studies. Since the angle correction by quadrupoles is not provided by the HUSR code, it was assumed that the electron beam after each quadrupole is at the central axis of the undulator.

7.3 Simulating the Photon Spectrum

As seen in section 7.1, HUSR was chosen as the best candidate code that can be used to simulate the spectrum of the photon created by a helical undulator-based positron source. For more further benchmarking HUSR code, the helical undulator photon spectrum simulated by HUSR is compared with the photon spectrum calculated by the analytical equation as in equation 5.32. Figure 7.12 shows a comparison between the ideal and realistic photon spectrums simulated by HUSR and the photon spectrum calculated by the analytical equation. The undulator parameters used here are that the undulator length is 1.75 m, $K = 0.85$ and $N = 152$, and $\lambda_u = 11.5$ mm and the error size are ± 4 and ± 10 % in case of the realistic undulator, respectively. The E_e used here is 125 GeV.

In the ideal case, the agreement between the two ideal approaches is pretty good for large numbers of observation points, for 20000 observation points that are distributed over a target plane of 1 cm^2 , although there is a small noise at higher harmonics. The difference is less than 0.02 %. In case of the realistic undulator, the noise is higher and the difference depends on the error size in K whether it is $\pm 4\%$ or $\pm 10\%$, respectively. This comparison as well as the comparative study carried out by Duncan Scott, discussed in section 7.1, show that the HUSR code is very accurate, and its results can be trusted when both ideal and realistic undulators are simulated.

7.4 Simulating the Photon Beam Polarization

The photon beam polarization, P_γ , can be calculated as a function of the photon energy by equation 7.3:

$$P_\gamma = \frac{N_l - N_r}{N_l + N_r} \quad (7.3)$$

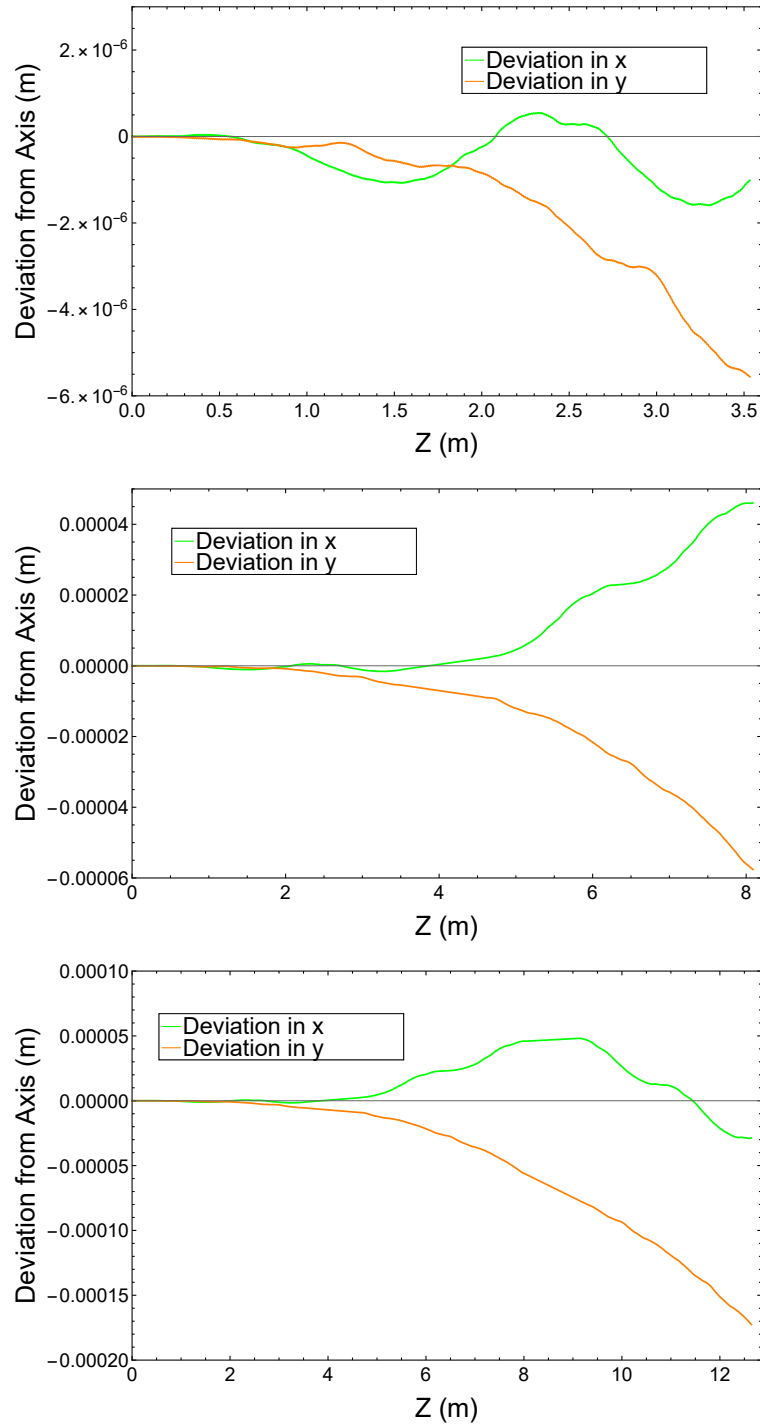


Figure 7.10: Deviation from the axis of a 125 GeV electron beam traveling through one, two and three (from top to the bottom) ILC realistic cryomodules with $K=0.85$ (0.79 T magnetic field strength) with $\pm 4\%$ error size in K .

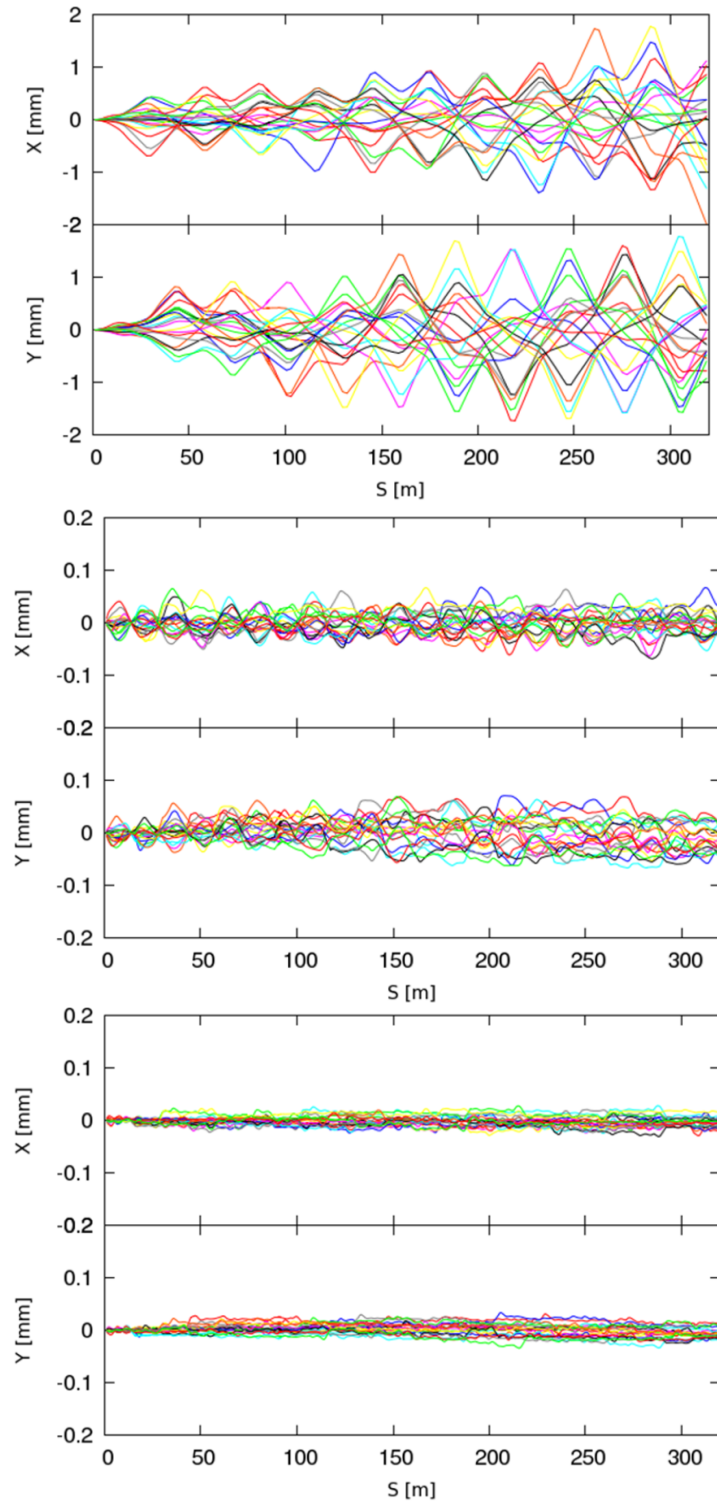


Figure 7.11: Deviation from the axis of a 125 GeV electron beam through the whole ILC realistic undulator length (320 m) with $K=0.85$ (0.79 T magnetic field strength) simulated by Toshiyuki OKUGI, KEK [55]. With no correction (top plot), with correction after 6 undulator modules (mid plot) and with correction after 2 modules (bottom plot).

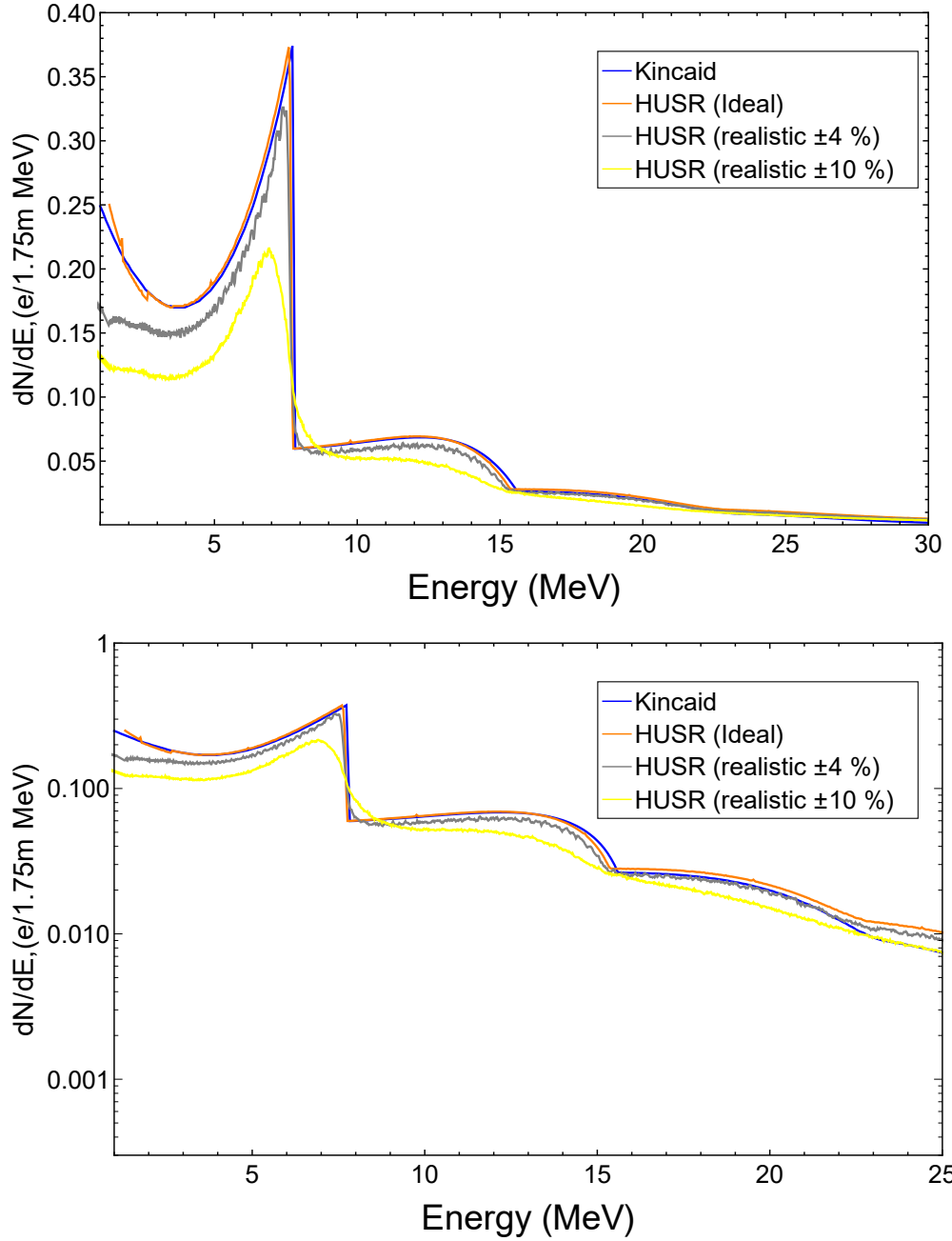


Figure 7.12: Comparison of the photon spectrum produced by a 125 GeV electron traveling through a 1.75 m helical undulator with $K = 0.85$ and $\lambda_u = 11.5$ mm calculated by an analytical equation and simulated by HUSR taking into account the ideal and realistic cases. The bottom plot is a logarithmic scale version of the top plot.

where N_l and N_r are the number of left and right handed circular polarized photons, respectively.

The trajectory of the electron beam through the undulator follows the trajectory of the wire wound of the undulator. as shown in figure 4.4. The emitted photons have left-handed spins if the winding is to the left side, and have right-handed spins if the winding is to the right side with respect to the observer, although, there will be photons with low energy that have a polarization of the opposite sign. In addition, the polarization rate depends on the distance between the emitter and the observer. More detail can be found in [29]. The HUSR code determines both the number of left and right handed circular polarized photons, figure 7.13 shows the spectrum and polarization of the photon beam at the target plane produced by passing one electron with energy of 125 GeV through one helical undulator module with 1.75 m length, $K=0.85$ and $\lambda_u=11.5\text{mm}$. The distance between this module and the target plane is 401 m.

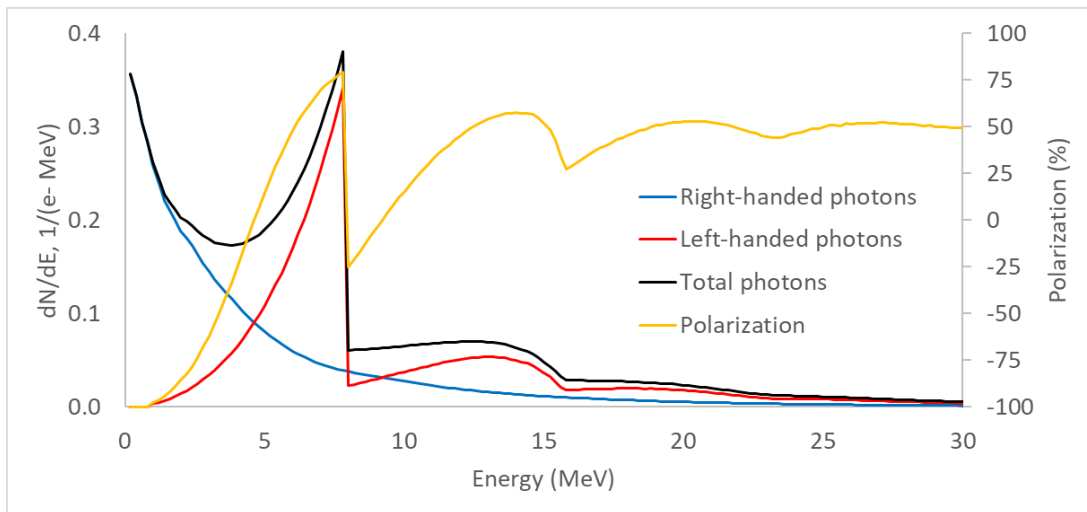


Figure 7.13: Ideal spectrum and polarization of the photon beam at the target plane produced by passing one electron with an energy of 125 GeV through one module with a 1.75 m length, $K = 0.85$, $B = 0.79$ T, period = 11.5 mm. The distance between this module and the target plane is 401 m.

Figure 7.14 shows the distribution of the energy and polarization of this photon beam at the target plane.

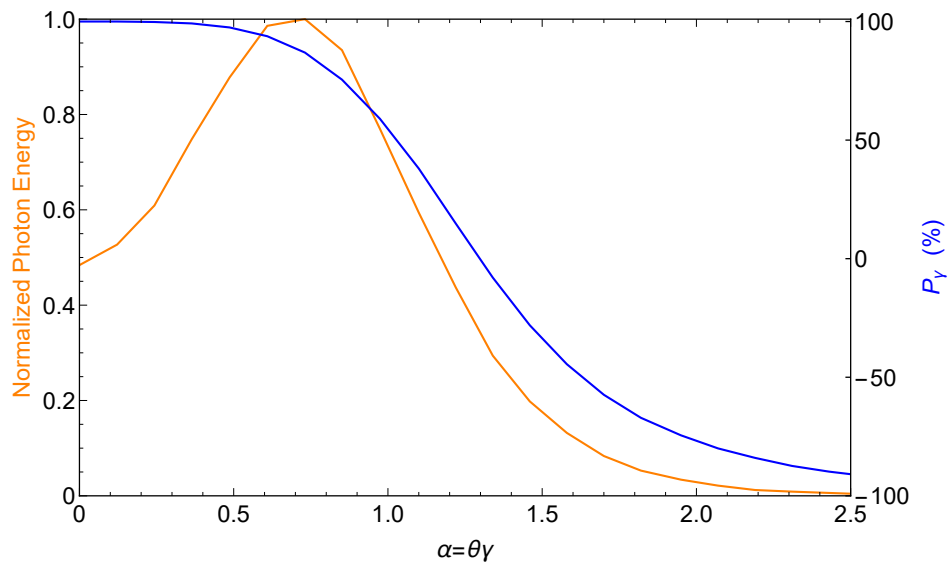


Figure 7.14: Ideal distribution of the photon beam energy and polarization at the target plane produced by passing one electron with energy of 125 GeV through one module with 1.75 m length, $K = 0.85$, $B = 0.79$ T, period = 11.5 mm. The distance between this module and the target plane is 401 m.

Chapter 8

Power Incident into the Undulator Vessel

Since the helical undulator produces photons with angular divergence and these photons travel through a very long undulator, a non-negligible fraction of these photons will hit the walls. It happens when the diameter of the photon beam cross-section becomes larger than the inner diameter of the helical undulator. Since the helical undulator emits photons as a cone of radiation, the incident photons will cause most problems towards the end of the undulator. The opening angle of the produced photon is determined by the K value and the energy of the electron beam, as seen in equation 5.38. This issue makes designing the vacuum system challenging since the vacuum pressure must be ~ 100 nTorr [56]. The incident photon on the undulator wall may cause two issues: the so-called Photon-Stimulated Desorption (PSD) on the beam pipe and the second one is the increase in the temperature of the beam pipe. As a result, the superconducting undulator magnets will quench.

PSD happens when a gas molecule is desorbed from subsurface layers of a vacuum vessel by an incident photon. The result is an increase in the vapour equilibrium gas density, which decreases the vacuum quality. In general, a very high vacuum in the superconducting magnet can be achieved by cryo-pumpings. Cryo-pumpings rely on gas molecules being cryo-sorbed onto the walls of the vacuum vessel. Nevertheless, this incredible technology can not provide a high vacuum due to the PSD. Therefore, photon masks can minimize the effect of this issue and ensure that the vacuum pressure is below ~ 100 nTorr. A detailed study of vacuum systems for the ILC helical undulator can be found in [56].

Besides the PSD, incident photons increase the temperature of the undulator walls so that the superconducting magnets can quench. In the following section, the incident power in the undulator

walls due to the SR is studied.

8.1 Calculating the Incident Synchrotron Radiation

Two methods are used to calculate the angular power distribution of the synchrotron radiation (SR) created by a helical undulator per longitudinal distance, including the analytical equation 5.36 and numerical HUSR code. In order to make sure that the electron beam exits the undulator with an energy of 125 GeV in the case of the ILC-250, the electron energy loss in the undulator must be taken into account, which is 3 GeV. Therefore, the electron beam energy that enters the first undulator module should be 128 GeV. While for example, the electron beam energy that enters the seventh and thirteenth undulator modules are 127.86 and 127.73 GeV, respectively.

The incident power is calculated using the relevant angles in the analytical case. Since the total helical undulator length is ~ 320 m, and the undulator aperture is 5.85 mm, all photons with an opening angle (θ) greater than $9.2 \mu\text{rad}$ will hit at the wall. As seen in figure 5.6, for example, in the case of the first undulator module, all power will leave the undulator except when $\alpha \geq 2.25$ ($\alpha = \gamma\theta$). So, the power with $\alpha \geq 2.25$ will hit the undulator wall. Also, in the case of, for example, the seventh module, the power with $\alpha \geq 2.35$ will hit the undulator wall.

In the numerical case, HUSR can be used to calculate the incident power at the undulator wall by increasing the distance between the undulator exit and the observation points. It is done by the following: The observation points, 20000 points, are distributed over a circular plane with the same diameter as the undulator module (5.85 mm). This plane is moved up to the exit of the first undulator. Since each observation point needs to receive enough events, and by the given ILC-250 parameters such as undulator diameter and E_e , HUSR is too time-consuming to calculate the photon spectrum when the distance between the undulator exit and observation points is below 25 m. Therefore, to get an accurate calculation, the chosen starting point was when the distance between the exit of the first undulator module and observation points is 25 m. It means that by the given parameters of the ILC-250, the maximum opening angle of photons that is included in this simulation is $103.5 \mu\text{rad}$. Firstly, only the first module was run to calculate its power distribution. Then the distance is increased to 26 m and thus, the power distribution is calculated. The different power values between these two steps are the incident power per meter at the wall. Then we increase the distance by steps, and each step is 1 m up to the exit of the last undulator module. Then the same method is done for the second undulator module and also for the rest of the modules taking into account the electron energy loss after each module.

8.2 Incident Power at the ILC Undulator Vessel

Figure 8.1 shows the incident power per meter on undulator walls caused by three different undulator modules, including the first, seventh, and thirteenth undulator modules for the ILC-250 undulator calculated by the analytical case. The incident power by these three modules has been plotted separately to show the significance of the position of the undulator modules and the electron beam energy on the incident power. The first module deposits the highest power, 1.2 W/m, at the

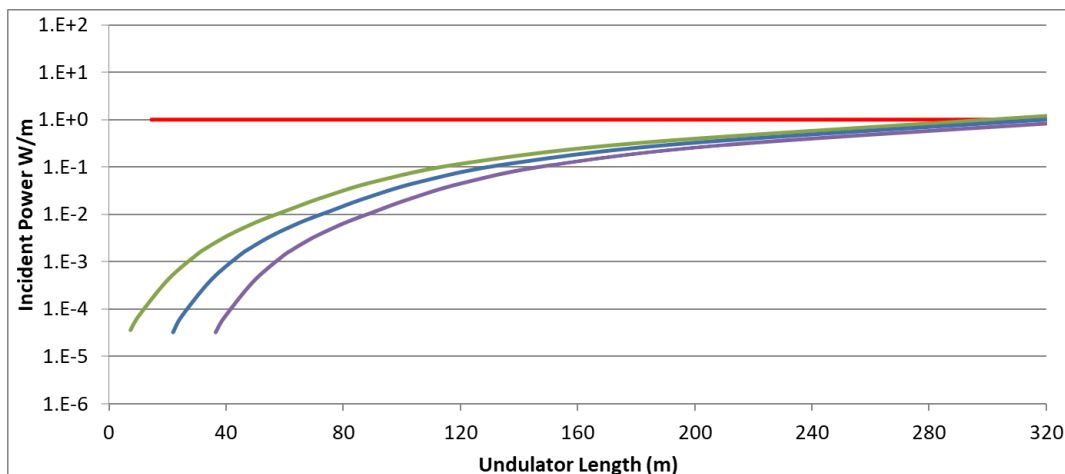


Figure 8.1: Incident power per meter in the undulator walls deposited by the first undulator module (green line), seventh undulator module (blue line) and the thirteenth undulator module (purple line). Red line represents the maximum allowable incident power into the undulator wall. The energy of electron beams are 128, 127.86 and 127.73 GeV for the first, seventh and thirteenth undulator modules, respectively. The undulator has a length of 1.75 m, $K=0.85$ and period=11.5 mm.

last meter of the undulator length. The maximum incident power by the seventh and thirteenth undulator modules is 0.89 W/m and 0.65 W/m at the last meter of the undulator length, respectively.

In order to verify the agreement of the results for both analytical and numerical cases, the power deposition from the first helical undulator module is calculated for both approaches considering the ideal case. Figure 8.2 shows the incident power by the first undulator module at the undulator walls along the undulator length for both analytical and numerical cases, using the parameter of the ILC-250. Comparing the results of both approaches, a good agreement can be found for distances above 30 m from the exit of the first undulator module to the observation points. Since the positron source of the ILC-250 needs 132 modules to produce the required positron yield, the incident power by these modules at the undulator walls is calculated and shown in figure 8.2.

The maximum incident power per meter from the first module is ≈ 1.20 W, and from all undulator modules is ≈ 21 W, which is a high heat load for the undulator walls. The maximum limit of the incident power in the undulator walls is 1 W/m [27]. Therefore, a photon mask system for machine protection is needed.

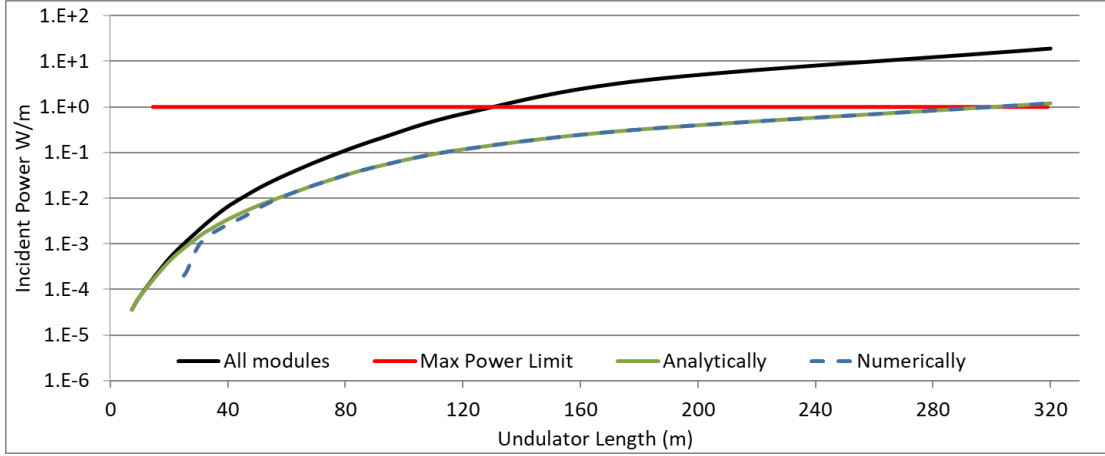


Figure 8.2: The green line and blue dashed line represent the incident power per meter along the undulator walls from a single ideal undulator module calculated using the analytical equation and HUSR, respectively. The black line represents the incident power on the undulator walls per meter from all 132 modules in case of the ILC-250 with $K=0.85$ and period=11.5mm. The red line shows the maximum allowable heat load in the undulator walls.

8.3 Mask System for the Undulator Protection

The system for protecting the undulator walls is a series of photon masks inserted along the length of the undulator line. These masks have a cylindrical geometry and are axially symmetric with a smaller radius than the undulator radius. As shown in the study of vacuum systems [56], the distance L_m between photon masks depends on the ratio of the inner diameters of photon masks d_m to undulator d_u . The simple geometry calculations below show that in order to achieve the required vacuum level, the L_m has to be:

$$L_m \leq 15 \text{ m for } d_m:d_u = 1:2$$

$$L_m \leq 7.5 \text{ m for } d_m:d_u = 3:4$$

Figure 8.3 shows that a photon mask is placed after the quadrupole. In total, 22 photon masks are used in the ILC undulator line.

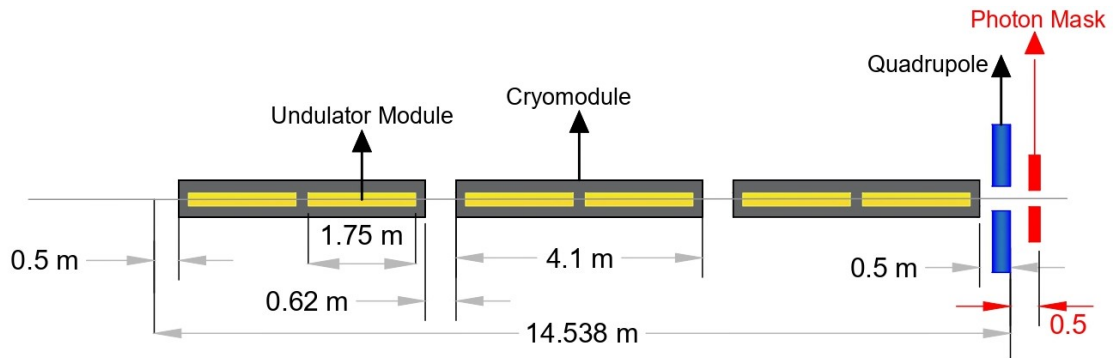


Figure 8.3: Schematic layout of the undulator line with a photon mask.

8.3.1 Basic Photon Mask Layout

The TDR [11] does not contain a complete design for photon masks to protect the undulator walls. A previous study in [57] proposed a possible mask design. In that study, a higher electron energy and a shorter undulator length were used with respect to the parameters of the ILC-250. Almost the same design as implemented in [57] is used here but with some differences since the ILC-250 has a lower electron energy and a longer undulator. The main similarity between these two designs is the inner diameter of 0.44 cm. Figure 8.4 shows a longitudinal section of the proposed mask, and figure 8.5 shows a drawing of the proposed mask cross-section along the z direction.

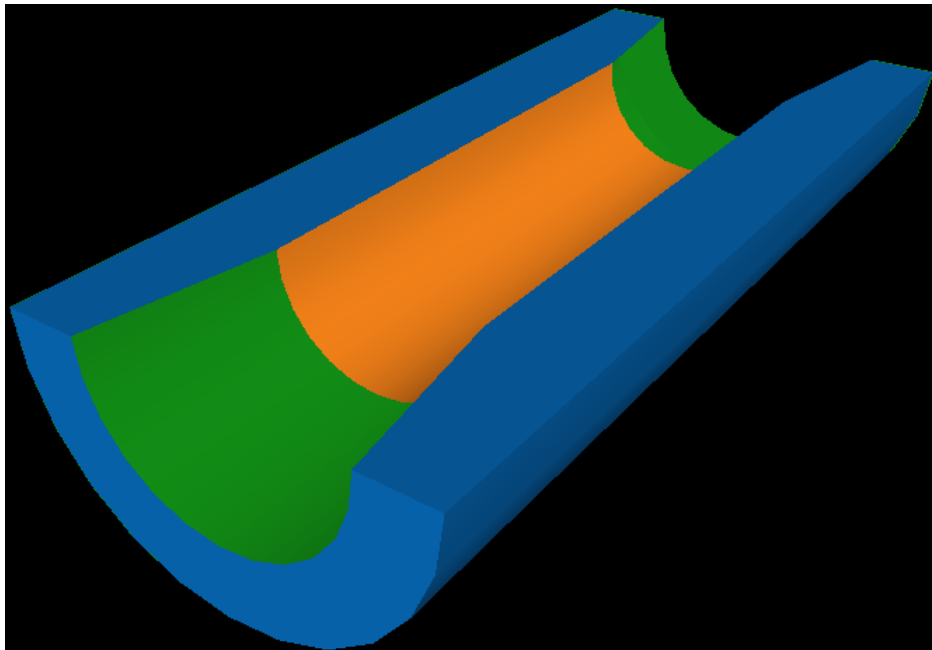


Figure 8.4: A longitudinal section of the photon mask. Green areas show the tapered sections. Orange area shows the inner radius with 0.22 cm.

The proposed mask here has a cylindrical geometry of 15 cm outer diameter. Since the available area for the ILC helical undulator is limited (the length of the undulator line is fixed to be 320 m), the maximum length of the mask is 30 cm. In order to reduce wake-fields, the inner radius of the mask is tapered for the first and last 5 cm of the length of the mask. Within the first 5 cm of the mask length, the inner radius is tapered from 0.2925 cm to 0.22 cm, and within the last 5 cm of the mask length, the inner radius is tapered from 0.22 cm to 0.2925 cm to match the undulator aperture. In between the two tapered sections, the inner radius of the photon mask is 0.22 cm.

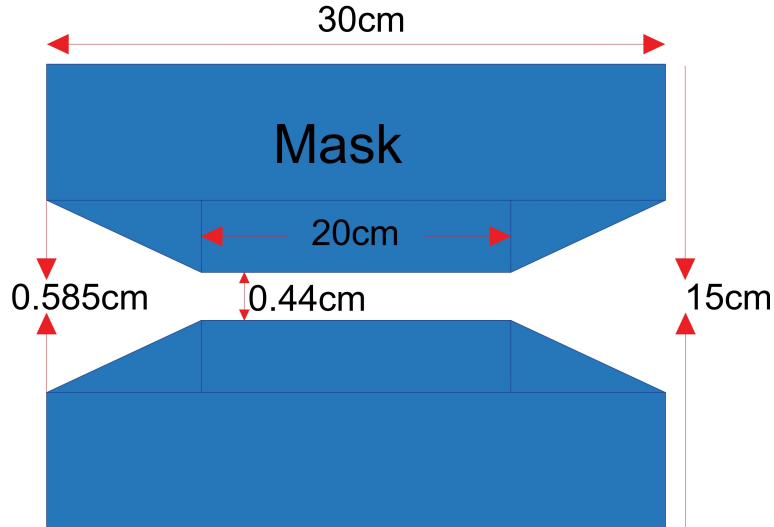


Figure 8.5: A drawing of the photon mask cross-section along the z direction.

8.3.2 Incident Power at Undulator Walls with Ideal Photon Masks

The incident power into the undulator walls is simulated using the HUSR code for ideal and realistic helical undulators. The considered error size in the realistic undulator case is $\pm 4\%$ as discussed in chapter 7. Figure 8.6 shows the incident power along the undulator walls for ideal and realistic undulators with and without photon masks. In this calculation, we assumed that photon masks are ideal and stop 100% of the incident power, so there are no secondary particles.

Since photons in a helical undulator are produced with an opening angle, some photons will pass through the mask hole and deposit at the undulator walls before the next mask, as seen in both cases. Since each realistic undulator module has a different B-field error distribution, the incident power on walls between masks is expected to differ as seen in the dip values in the bottom plot in figure 8.6. Photon masks could reduce the incident power on the undulator walls due to the primary photons below the acceptable limit (1 W/m). The maximum incident power due to the primary photons before placing the masks is 21 W/m and 23.5 W/m for the ideal and realistic undulators, respectively. This power hits the last meter of the undulator line. It is the last meter before the last mask, number 22 (Mask-22). After placing the masks, this power reduces to 0.021 W/m and 0.025 W/m for the ideal and realistic undulators, respectively.

Since an ideal mask will never exist, the realistic mask should be studied. In order to calculate the incident power into walls due to the secondary particles, the incident power into each mask must be studied. Next, the material of the mask can be chosen, and then the incident power due to secondary particles into the undulator walls can be calculated.

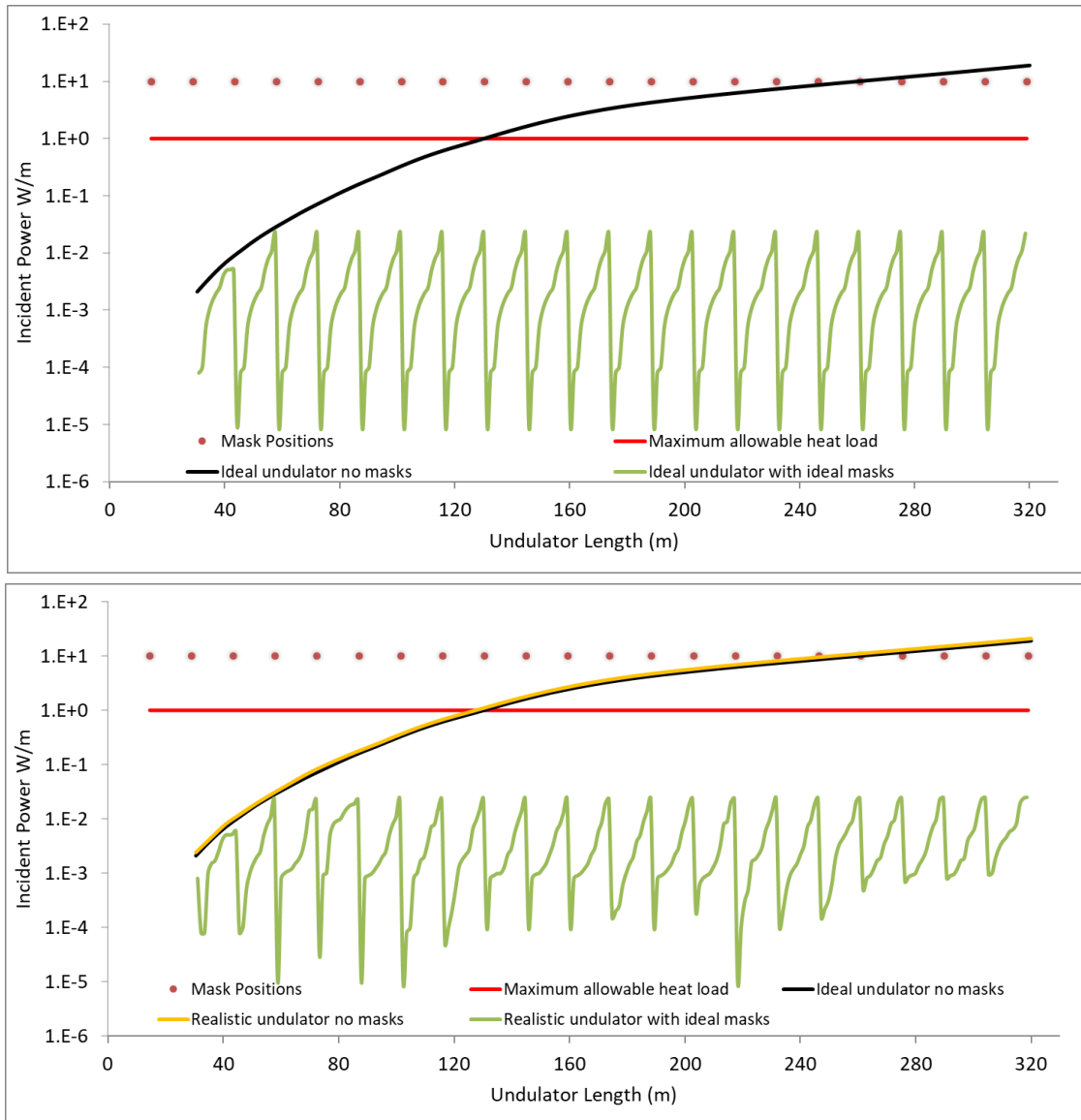


Figure 8.6: Incident power at the undulator walls due the primary photons produced by the full active length of the ideal (upper plot) and realistic (bottom plot) ILC-250 undulators simulated by the HUSR code. Black and orange lines represent the deposited power at the wall with no masks for ideal and realistic undulator cases, respectively. The green line represents the deposited power at the walls with masks. The red points represent the position of the photon masks and red line shows the maximum allowable heat load in the undulator walls.

8.3.3 Incident Power at Photon Masks

In order to choose the appropriate material for the photon masks, the incident power at these masks was simulated. Due to the opening angle of the photons created by a helical undulator, Mask-22 receives the highest amount of the power which is 335 W and 361 W for ideal and realistic undulators, respectively. In addition, the average energy of the incident photons is 2.01 and 2.14 MeV for both ideal and realistic undulators, respectively. While for example, Mask-15 receives only 100 W and 110 W for ideal and realistic undulators, respectively. Figures 8.7 and 8.8 show the incident power and average photon energy at masks. Table 8.1 summarizes the data for ideal and realistic undulators.

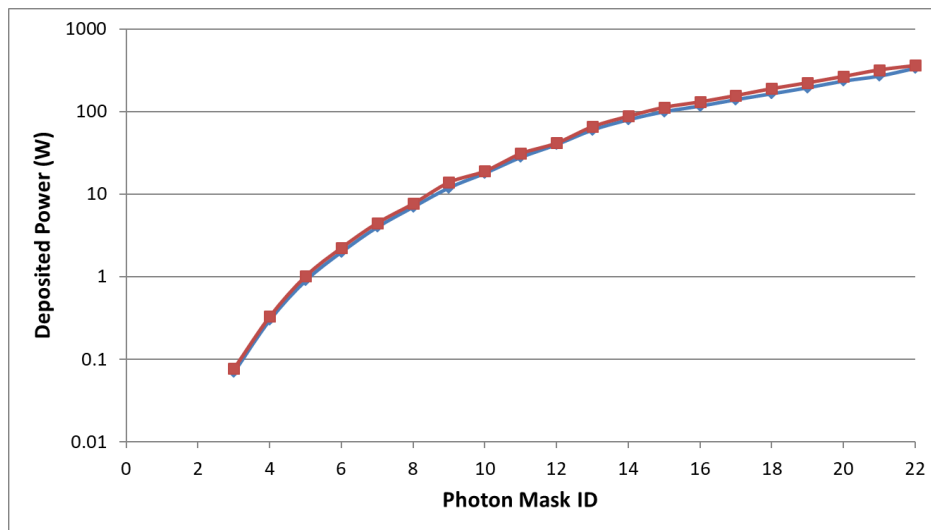


Figure 8.7: Power incident on photon masks. The blue (red) represents the incident power by ideal (realistic) undulators using the parameters of the ILC-250.

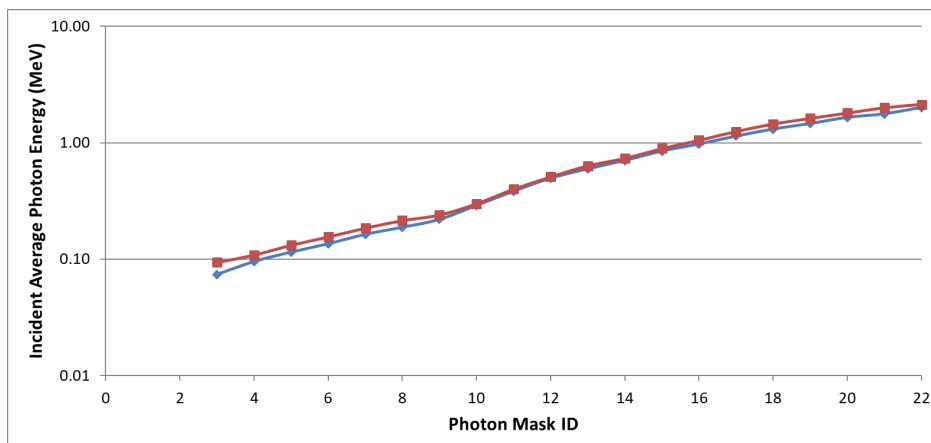


Figure 8.8: Average incident photon energy on photon masks. Blue (Red) represents the average incident photon energy by ideal (realistic) undulators using the parameters of the ILC-250.

Table 8.1: Incident power, average incident photon energy and incident photon number at masks for both ideal and realistic undulators using the parameters of the ILC-250.

Mask ID	Power (W)		Average energy (MeV)		Photon number $\times 10^{13}$ /pulse	
	<i>Ideal</i>	<i>Real</i>	<i>Ideal</i>	<i>Real</i>	<i>Ideal</i>	<i>Real</i>
3	0.07	0.08	0.07	0.09	0.12	0.13
4	0.3	0.33	0.10	0.11	0.39	0.42
5	0.9	1	0.12	0.13	0.98	1.04
6	2	2	0.14	0.16	1.84	1.95
7	4	5	0.16	0.19	3.06	3.24
8	7	8	0.19	0.21	4.65	4.93
9	12	14	0.22	0.24	6.82	7.23
10	18	19	0.29	0.30	7.76	7.91
11	28	31	0.38	0.40	9.11	9.66
12	40	42	0.50	0.51	10.1	10.2
13	60	66	0.60	0.63	12.6	12.9
14	80	88	0.70	0.74	14.2	14.9
15	100	110	0.85	0.89	14.7	15.5
16	117	131	0.98	1.05	15.0	15.6
17	140	157	1.14	1.25	15.4	15.7
18	165	190	1.31	1.45	15.7	16.4
19	195	223	1.46	1.62	16.7	17.2
20	235	267	1.65	1.80	17.8	18.5
21	270	320	1.77	2.00	19.1	20.0
22	335	361	2.01	2.14	20.8	21.1

8.4 Material Candidates for Photon Masks

The photon masks must absorb both the primary incident photons and the secondary particles. Since photon masks will have the same design and receive different amounts of power, the power that leaves masks differs from mask to mask. As a result, incident secondary particles into walls from each mask will be different. The mask material has to stop photons with an average energy in the range of MeV. It also should allow for a short mask that provides excellent thermal conductivity. Three different materials, iron (Fe), copper (Cu), and tungsten (W), are studied to find the proper material for the mask. The properties of the material candidates are summarized in table 8.2.

Table 8.2: Properties of the material candidates for masks.

Parameter	Symbol	Unit	Copper	Iron	Tungsten
Atomic number	Z		29	26	74
Density	ρ	g/cm ³	8.96	7.89	19.3
Thermal conductivity	λ	W/(cm.K)	4.01	0.835	1.82
Heat capacity	C_p	J/g/K	0.385	0.45	0.134
Melting point		K	1357.77	1811	3695
Radiation length	X_0	cm	1.436	1.757	0.35

8.5 Power Deposition in Realistic Photon Masks

In the ILC-250, the total active length (231 m) should be used to produce the required photon beam. Due to the opening angle of the photon beam, masks inserted in the second half of the undulator line receive a higher power than masks inserted in the first half, as seen in figure 8.7. The last mask (Mask-22) is placed at the undulator exit. This mask receives the highest amount of the incident power. Therefore, Mask-22 is essential to determining the maximum energy deposition, the instantaneous temperature rise and the stress in masks. But to study the worst-case scenario of the incident power into the undulator wall due to the secondary particles, the incident power into mask number 21 (Mask-21) should be studied since it is the last mask located inside the undulator line. This can be simulated by the software package of FLUKA [58]. FLUKA is a Monte Carlo code for particle tracking and particle interactions with matter. The distribution of the incident photons at masks simulated by HUSR is used as input to FLUKA. Figures 8.9 and 8.10 show the deposited energy along Mask-21 and Mask-22 with Fe, Cu, and W materials for both ideal and realistic undulators using the parameters of the ILC-250, respectively. Figures 8.11 and 8.12 show the distribution of the maximum energy along the Fe, Cu, and W masks for both ideal and realistic undulators in Mask-21 and Mask-22, respectively.

Figure 8.13 shows the maximum deposited energy and the Peak Energy Deposition Density

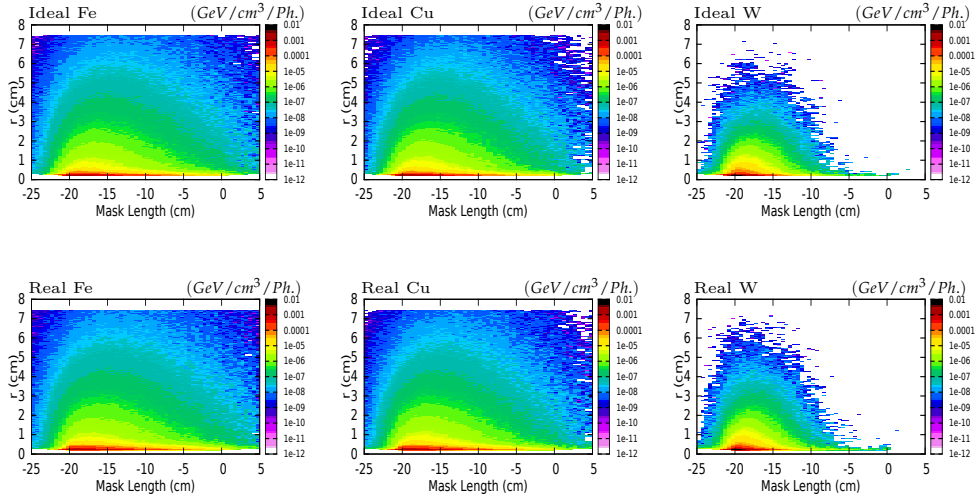


Figure 8.9: The deposited energy along the Fe , Cu and W Mask-21. Top (Bottom) plots show the energy deposition in case of ideal (realistic) undulators of the ILC-250 with $K = 0.85$.

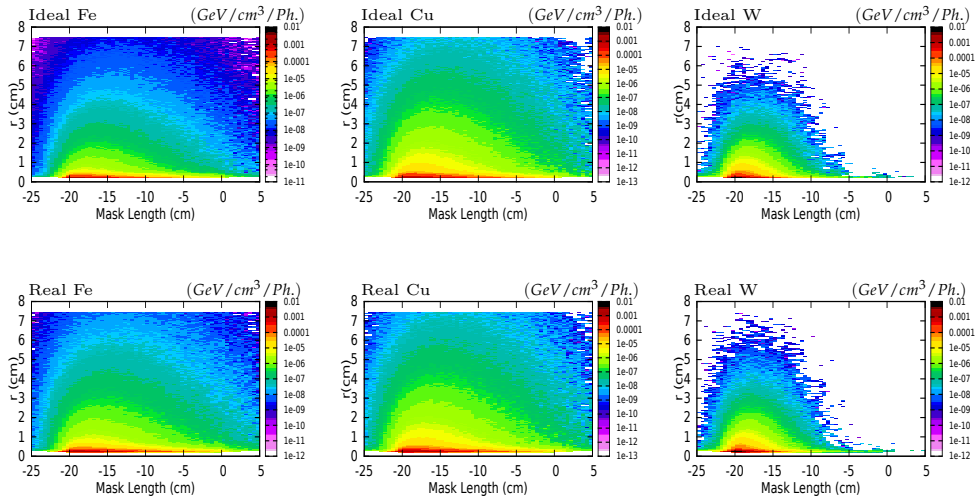


Figure 8.10: The deposited energy along the Fe , Cu and W Mask-22. Top (Bottom) plots show the energy deposition in case of ideal (realistic) undulators of the ILC-250 with $K = 0.85$.

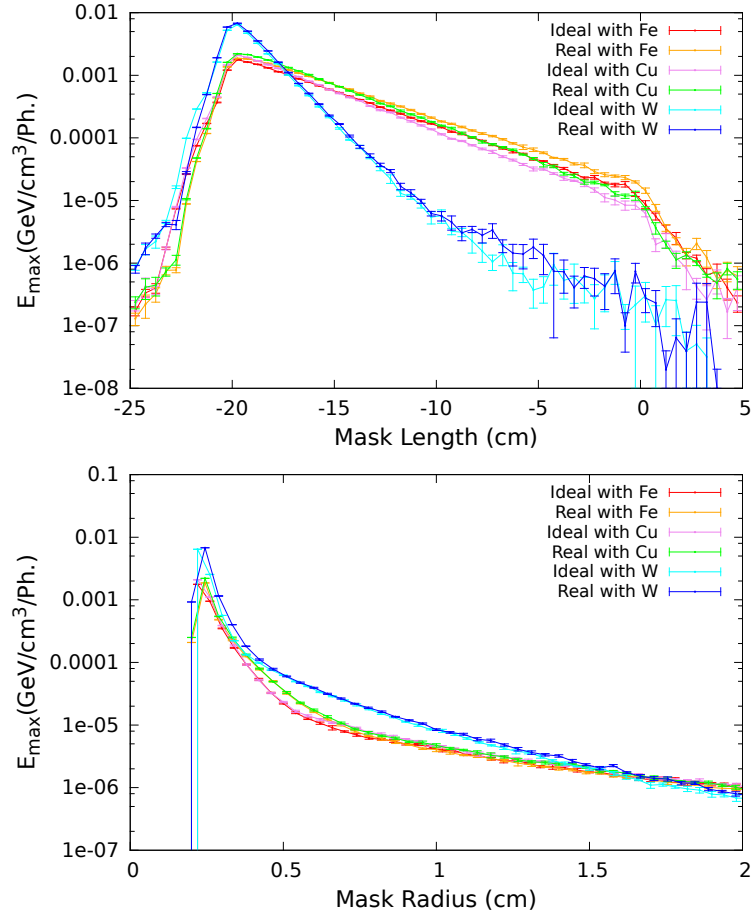


Figure 8.11: The maximum deposited energy ($\text{GeV}/\text{cm}^3/\text{photon}$) along iron, copper and tungsten **Mask-21** for both ideal and realistic undulators of the ILC-250 with $K = 0.85$. Upper (Bottom) figure shows the maximum deposited energy along Z-direction (radial) mask length.

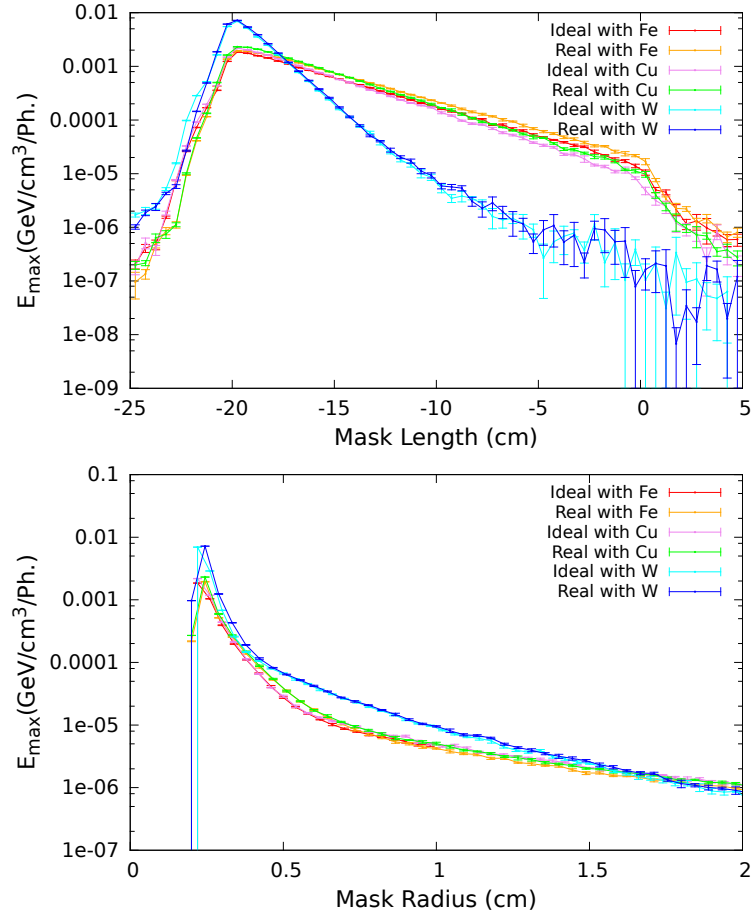


Figure 8.12: The maximum deposited energy ($\text{GeV}/\text{cm}^3/\text{ph.}$) along iron, copper and tungsten **Mask-22** for both ideal and realistic undulators of the ILC-250 with $K = 0.85$. Upper (Bottom) figure shows the maximum deposited energy along Z-direction (radial) mask length.

(PEDD) along the length of the Cu Mask-22. The maximum values are at the end of the first tapered section of the mask.

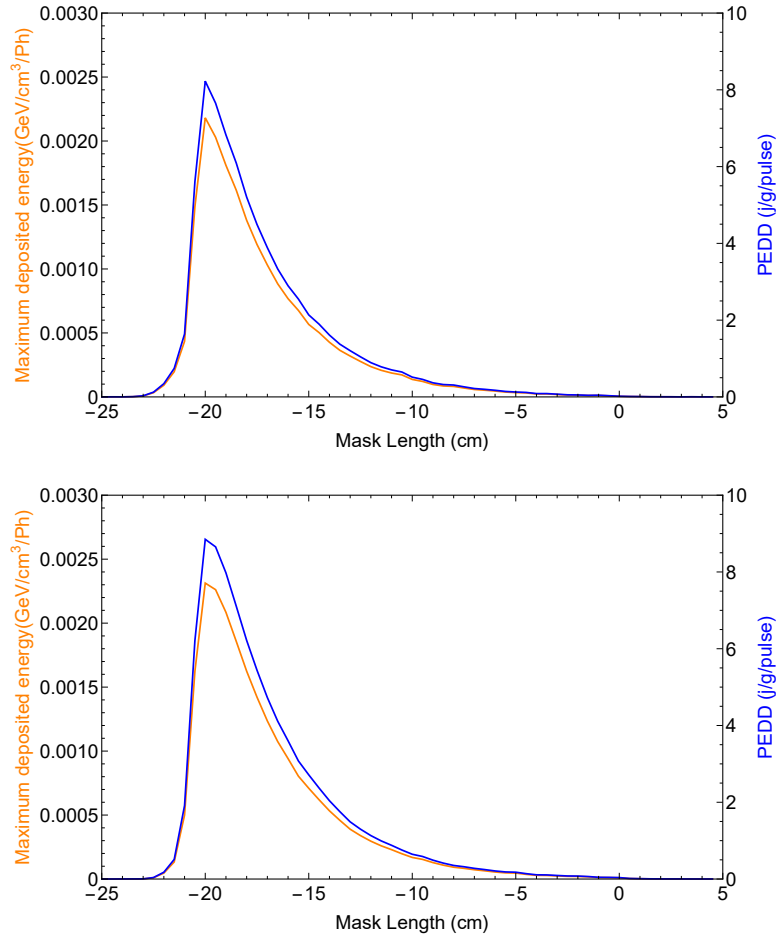


Figure 8.13: The PEDD and maximum deposited energy along Z-direction in Cu Mask-22 for both ideal (upper plot) and realistic (bottom plot) undulators of the ILC-250 with $K = 0.85$.

Table 8.3 summarizes the results of these studies. It shows that masks with any of the material candidates are safe. For example, PEDD on Mask-22 is 8.12 (J/g/Pulse), 8.66 (J/g/Pulse), and 12.59 (J/g/Pulse) for Fe, Cu, and W masks, respectively, in the case of realistic undulators. In addition, W Mask-22 can stop up to 99.5 % and 98.4 % of the incident power for both ideal and realistic undulators, respectively.

Table 8.3: Average incident photon energy (E_{ave}^γ), deposited power (P_{mask}), incident photon number (N_{mask}^γ), maximum deposited energy (E_{max}), Peak Energy Deposition Density (PEDD), temperature rise (ΔT_{max}) at Mask-21 and Mask-22 and power stopped by these masks (P_{stop}^{mask}) using three different materials in both ideal and realistic cases of the ILC-250 undulators with $K = 0.85$.

Parameters	<i>Mask</i>	Mask-21		Mask-22	
	<i>material</i>	<i>Ideal</i>	<i>Real</i>	<i>Ideal</i>	<i>Real</i>
$E_{ave}^\gamma (MeV)$		1.82	2.00	2.01	2.14
$P_{mask} (W)$		270	311	335	361
$N_{mask}^\gamma / \text{pulse} (\times 10^{13})$		18.54	19.47	20.83	21.09
$E_{max} (MeV / cm^3 / Ph.)$	<i>Fe</i>	1.7	1.8	1.8	1.9
	<i>Cu</i>	2.1	2.2	2.2	2.3
	<i>W</i>	6.4	6.8	6.9	7.2
PEDD (J/g/pulse)	<i>Fe</i>	6.4	7.1	7.6	8.1
	<i>Cu</i>	6.9	7.6	8.2	8.7
	<i>W</i>	9.8	11.0	11.9	12.6
ΔT_{max} (K/pulse)	<i>Fe</i>	14.2	15.8	16.9	18.0
	<i>Cu</i>	18.0	19.9	21.3	22.5
	<i>W</i>	73.4	81.9	88.9	93.9
P_{stop}^{mask} (%)	<i>Fe</i>	97.6	96.5	97.5	96.4
	<i>Cu</i>	98.3	97.3	98.4	97.2
	<i>W</i>	99.5	98.5	99.5	98.4

8.6 Heat Load at the Photon Masks

The deposited energy per photon along masks was simulated using FLUKA. The bottom plot in figure 8.12 shows the maximum deposited energy per photon (in units GeV/cm³/photon) along Mask-22 in the radial direction with different mask materials for both ideal and realistic undulators of the ILC-250. The peak energy is deposited at the inner radius of the mask, where it induces a maximum temperature rise per pulse (ΔT_{max}) as given in table 8.3. If the heat diffusion between pulses is neglected, the temperature accumulates to a non-realistic high value over time. Nevertheless, in reality, the heat moves in 200 ms, which is the time between pulses (t_p) in the ILC, and distributes over a distance (H_m) which is approximated by:

$$H_m = \sqrt{\frac{\lambda t_p}{\rho C_p}} \quad (8.1)$$

Where λ represents the thermal conductivity, C_p represents the heat capacity and ρ represents the density of the mask material.

The heat spot distributes between two pulses over an area with a radius of about 2.2 mm for iron, 4.9 mm for copper, and 3.8 mm for tungsten. The average radial temperature profile is quite smooth except the peaks of the cyclic loads with instantaneous temperature rise. Assuming 5000 hours as the running time of the ILC-250 per year, there will be 9×10^7 load cycles at the ILC photon mask. The instantaneous rise in temperature in a region, that is restricted to expand, creates a stress in the material. Usually, the maximum instantaneous stress (σ_{max}) can be estimated by the following equation [59, 60]:

$$\sigma_{max} = Y_m \Delta T_{max} \alpha_h \quad (8.2)$$

Table 8.4 shows the minimum and maximum values of the young's modulus (Y_m), thermal expansion coefficient (α_h), and tensile strength (F_{tu}) of the material candidates. The values of the maximum instantaneous temperature rise (ΔT_{max}) are calculated in the case of the realistic undulator and given in table 8.3.

Taking the minimum and maximum values of the material properties, table 8.4 shows the maximum instantaneous stresses (σ_{max}) at all three material candidates. The maximum instantaneous stress is below the tensile strength of all material candidates. To avoid a material failure for a long-term cyclic operation, it is recommended that the fatigue limits of the material should not be exceeded, which is $\approx 40\%$ of the tensile strength of the material [64]. The results in table 8.4 show that in the realistic case of the ILC-250 the maximum instantaneous stress is lower than 22% of the

Table 8.4: The minimum and maximum values of the Young’s modulus of elasticity (Y_m), Thermal expansion coefficient (α_h), and Tensile strength (F_{tu}) of the material candidates. Values of parameters are taken from [61, 62, 63]. The calculated σ_{max} at Mask22 with three material candidates using realistic undulators with $K = 0.85$ is added as well.

Parameters	Material candidates		
	<i>Fe</i>	<i>Cu</i>	<i>W</i>
Y_m (GPa)	204 – 212	121 – 133	340 – 405
α_h ($\times 10^{-6}/K$)	12.0 – 12.5	16.8 – 17.9	4.2 – 4.6
F_{tu} (MPa)	230 – 345	210 – 390	1670 – 3900
σ_{max} (MPa)	44.1 – 47.7	45.7 – 53.6	134.1 – 174.9

tensile strength for all material candidates. Since the PEDD and maximum temperature rise at the photon masks of both the ILC-350 and ILC-500, as will be seen in section 8.9, are lower than those of the ILC-250, the maximum instantaneous stress will also be lower.

In equilibrium and assuming there is a continuous heat source, equation 8.3 can be used to estimate the radial heat dissipation through the mask with central heating.

$$\Delta T = (t_i - t_o) = \frac{\ln(\frac{r_o}{r_i})Q}{2\pi L_{mask}\lambda} \quad (8.3)$$

Where, L_{mask} is the cylinder (mask) length. r_o and r_i are the outer and inner radius of the mask, respectively. λ is the thermal conductivity of the mask material and Q is the deposited power at the mask.

The highest deposited power in the ILC-250 is 361 W at Mask-22 in the case of the realistic undulator. As seen in figure 8.10, the deposited power is not equally distributed along the mask. The highest deposited power is at a small part of the mask that is represented by the red spot. Figure 8.14 shows the area of the mask which receives the highest deposited energy for three various material candidates in the case of the realistic undulator of the ILC-250.

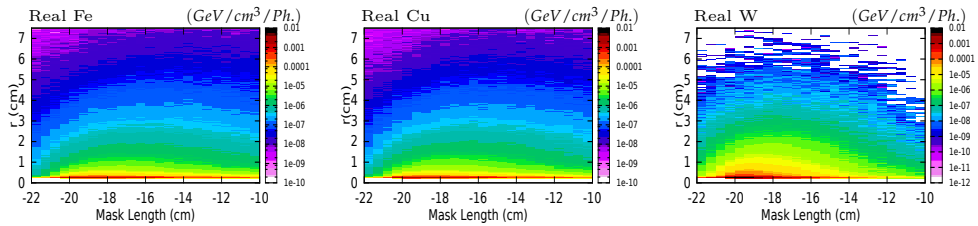


Figure 8.14: The deposited energy per photon along Z-direction of the considered part of the realistic Fe , Cu and W **Mask-22** (from left to right). Plots show the energy deposition in case of realistic undulators of the ILC-250 with $K = 0.85$.

Equation 8.3 is used to estimate the maximum temperature difference between the inner and outer surfaces of the mask. It is assumed that the length of the mask is $L_{mask} = 7$ cm corresponding to the part with the highest power deposition. The inner and outer mask radii are the same as the proposed values of the ILC mask, which are 0.22 cm and 7.5 cm, respectively. So, the maximum ΔT is 35 K for iron, 7 K for copper, and 16 K for tungsten. Although there is a hot spot at the mask, the heat gradient is not large and the heat can be carried away by a cooling system.

8.7 Distribution of Secondary Particles at the Undulator Walls

Secondary particles are generated when photons with high energy pass through a material. The main secondary particles are photons, electrons, and positrons. Depending on the mask material, the mask will stop and absorb some secondary particles, while some, especially those with enough energy, can escape from the mask.

In order to study the incident power at the undulator walls due to secondary particles, the distribution of secondary particles around the mask should be studied. This can be simulated using the so-called USRBDX detector in FLUKA. Figure 8.15 shows all possible directions of secondary particles around a photon mask. Here we are interested in secondary particles that leave the mask and may hit the wall. The orange and red arrows show the incident power into the undulator wall due to back-scattered photons and secondary particles, respectively.

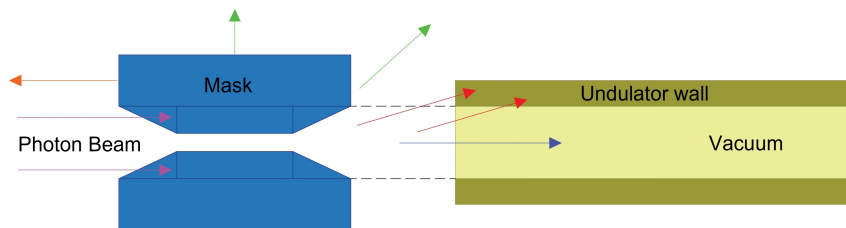


Figure 8.15: A drawing of all possible directions of secondary particles around the photon mask. Blue and red arrows represent secondary particles passing through the undulator vacuum and the secondary particles deposited into the undulator wall, respectively. Green arrows represent the direction of the secondaries leaving the mask in a radial direction and lost in between the mask and the undulator. The orange arrow represent the back-scattered photons.

Three different materials for the mask are studied using the exact mask dimensions. Due to material properties, particles that leave the mask are based on the type of material, whether it is a Fe, Cu, or W material. Therefore, it is accepted that the highest total incident power on the walls is when iron masks are used, while the lowest is with tungsten masks. Figure 8.16 and 8.17

show the density of secondary particles, including photons, electrons, and positrons, along the Fe, Cu, and W Mask-21 and Mask-22 for both ideal and realistic undulators, respectively. The density of electrons and positrons is lower than that of photons along the masks for ideal and realistic undulators. Photons form the most power (95%) that leaves the mask. While the incident power by electrons and positrons only forms $\leq 5\%$.

Figure 8.18 shows the spectrum of photons escaping Fe and Cu photon masks for both ideal and realistic helical undulators considering 250 GeV centre-of-mass energy and $K = 0.85$. Since the W mask stops almost 99.5 % of the deposited power, there are not enough photons to plot the spectrum.

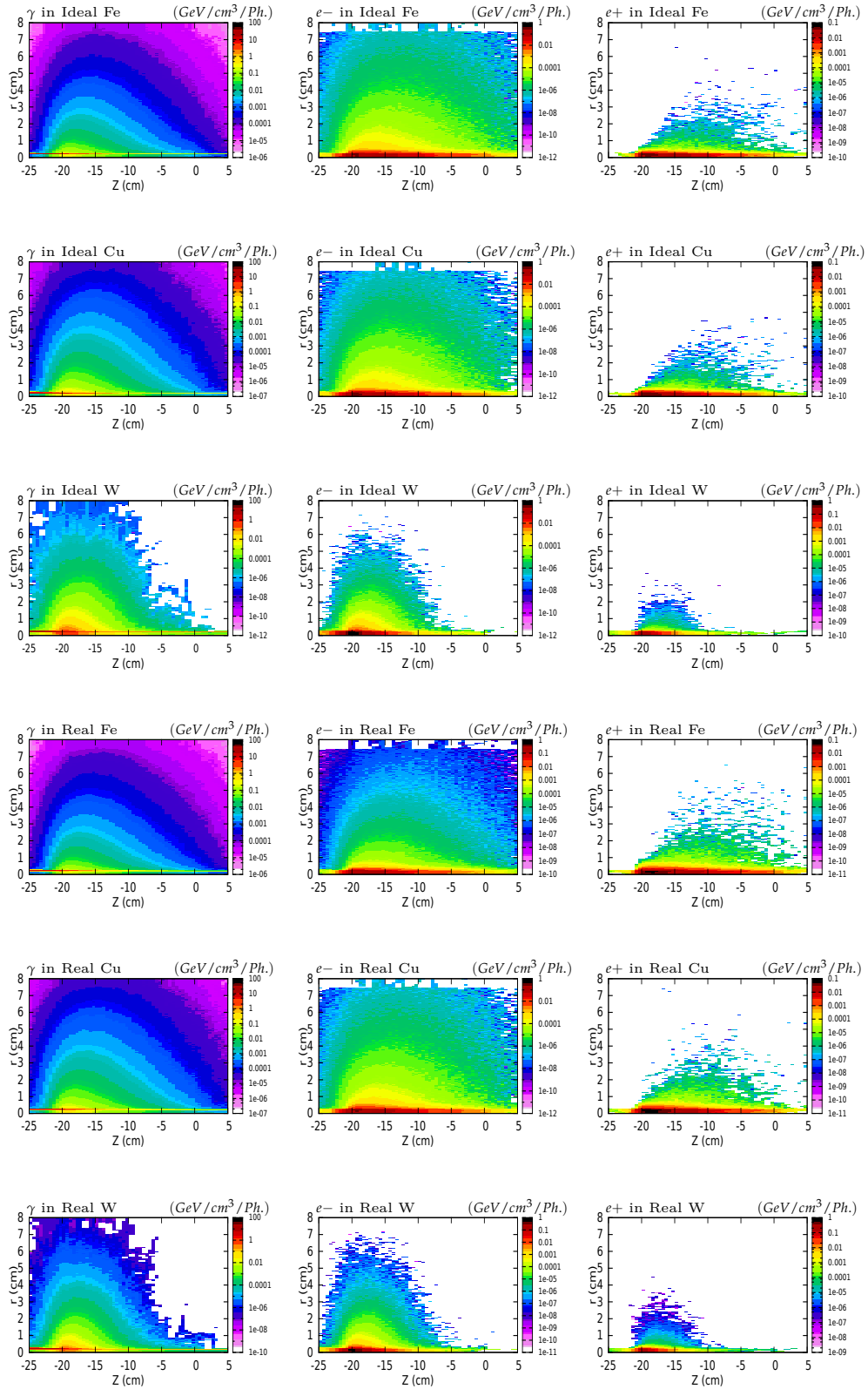


Figure 8.16: The density of secondary particles, including photons, electrons and positrons, along the Fe , Cu and W Mask-21 for both ideal and realistic undulators for the ILC-250 with $K = 0.85$.

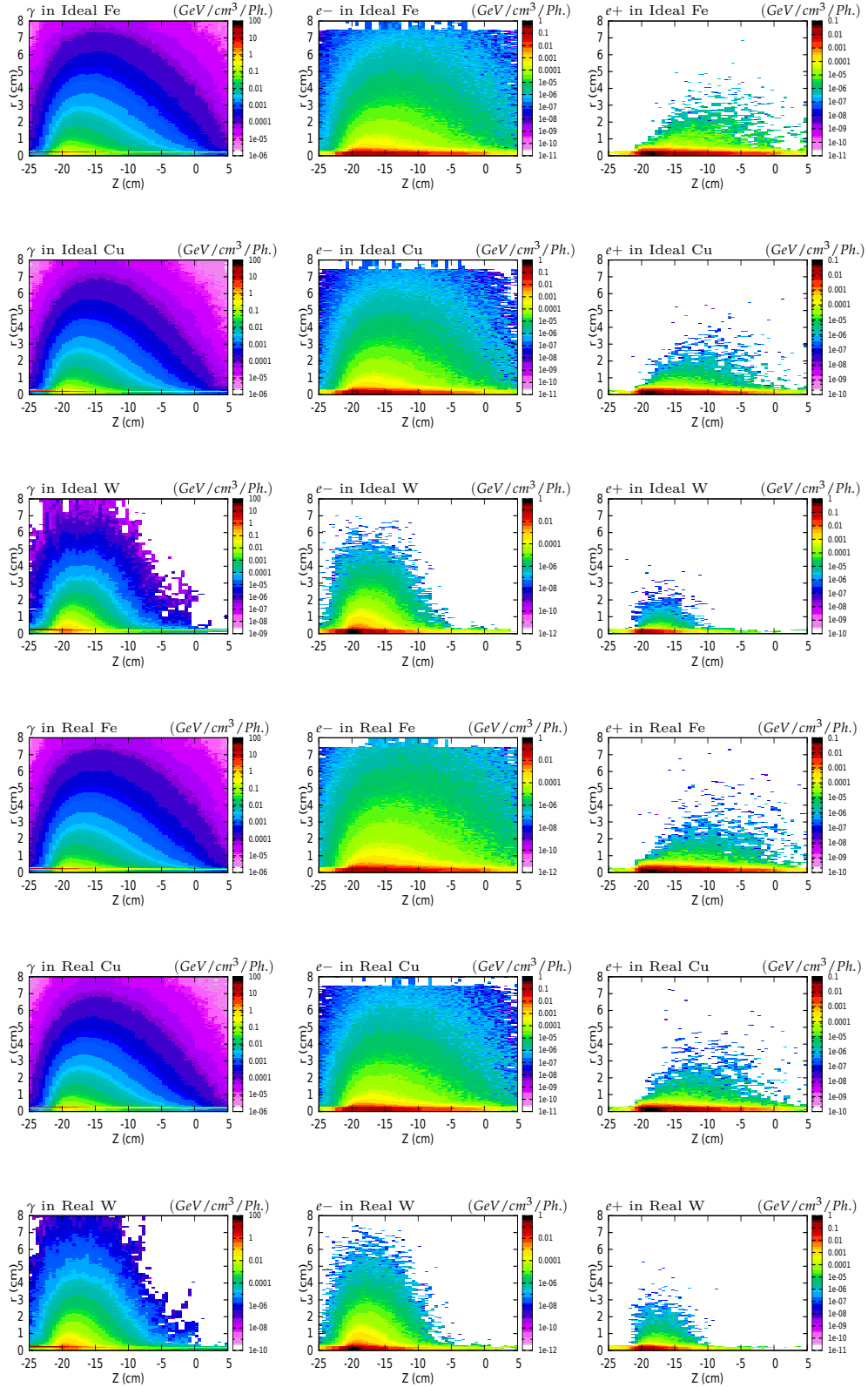


Figure 8.17: The density of secondary particles, including photons, electrons and positrons, along the Fe , Cu and W Mask-22 for both ideal and realistic undulators for the ILC-250 with $K = 0.85$.

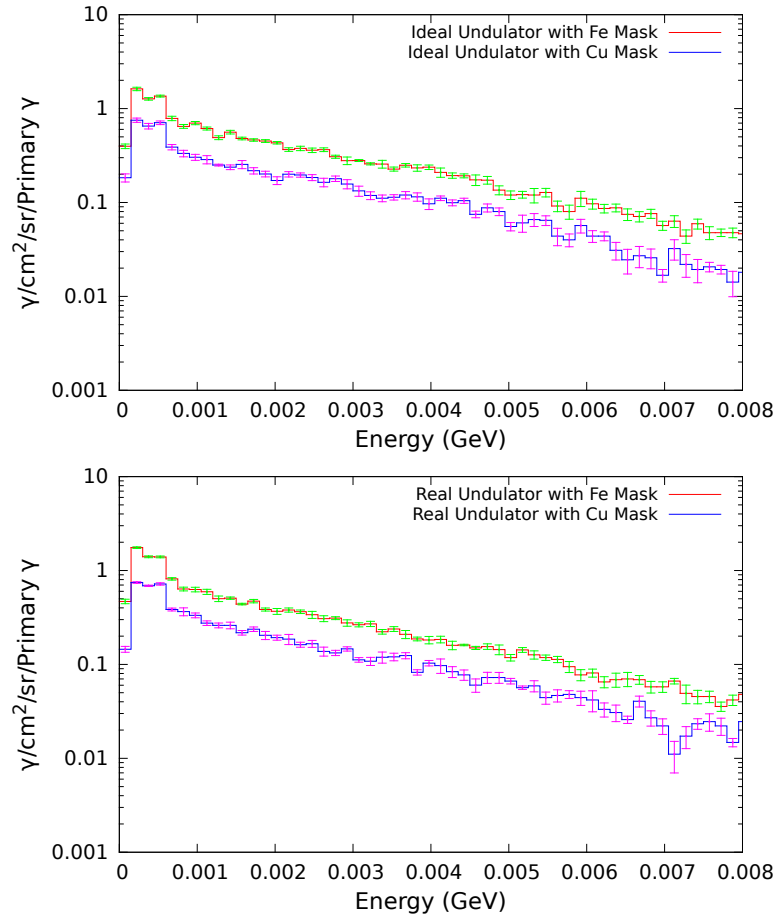


Figure 8.18: Spectrum of photons escaping Fe and Cu photon masks to the undulator. Upper (Bottom) plot shows the photon spectrum in the case of the ideal (realistic) undulator of the ILC-250 with $K = 0.85$. The unit of Y axis is photons/cm²/solid angle/primary photon.

8.8 Result

The incident power into the undulator walls is studied for both ideal and realistic undulators using the nominal parameters of the ILC-250. The maximum incident power due to the primary photons is 21 W/m and 23.5 W/m for the ideal and realistic undulators, respectively. This power deposits at the last meter of the undulator line. Since the maximum limit of the incident power in the undulator walls is 1 W/m, photon masks are proposed. Three different materials for photon masks are considered in this study, including Fe, Cu, and W materials. In addition to the incident power into the wall due to primary photons, the incident power due to secondary particles is studied for all considered materials. The "total incident power" here refers to the sum of the incident power due to the primary photons plus the incident power due to the secondary particles, including photons, electrons, and positrons.

8.8.1 Incident Power at Masks

Due to the photon opening angle, the highest deposited power is at the last mask located at the undulator exit (Mask-22), and is 335 W and 361 W for ideal and realistic undulators, respectively, in the case of the ILC-250 with nominal parameters. The average incident photon energy is 2.01 MeV and 2.14 MeV at the Mask-22 for ideal and realistic undulators, respectively. Therefore, the mask is designed to stop this deposited power.

8.8.2 Heat Load at Mask Material Candidates

The mask is designed in order to stop both the primary photons and secondary particles. Different mask materials are investigated. The best mask material is tungsten which can stop up to 99.5 % and 98.4 % of the deposited power for ideal and realistic undulators, respectively. In contrast, the copper can stop 98.4 % and 97.2 % of the deposited power in the case of ideal and realistic undulators, respectively.

The PEDDs of all candidate materials show that the mask is safe. For example, the PEDD of copper at Mask-22 is 8.2 J/g/pulse and 8.7 J/g/pulse for both ideal and realistic undulators, respectively. The result of the estimation of the heat distribution shows that the heat distribution through the copper is 4.8 mm/0.2 sec while it is only 2.2 mm/0.2 sec for the iron due to the high thermal conductivity of the copper. The maximum instantaneous stresses at masks are below the fatigue limits of all material candidates. In addition, the result of the estimation of the average temperature difference between the inner and outer surfaces of the mask shows that it is only 7.22 K while it is 34.7 K for the iron and this is due to the high thermal conductivity of the copper. However, cooling and maintaining low temperatures are not an issue. Using copper makes the

situation more efficient and less complicated.

8.8.3 Incident Power at Ideal and Realistic Undulator Walls

Figure 8.19 shows the incident power on the ideal undulator walls produced by the full active length of the ideal ILC-250 undulator case with nominal parameters before and after placing the photon masks. In addition, it shows the influences of the material mask candidates on the total incident power in the undulator walls. With tungsten masks, the total deposited power is only $0.034 \text{ W} \pm 30 \%$ in the first meter of the module after Mask-21, while it is $0.31 \text{ W} \pm 5 \%$ and $0.22 \text{ W} \pm 6 \%$ for iron and copper masks, respectively. The total deposited power is lower in the case of the W mask used because of its high density compared with the density of the Fe and Cu materials.

Figure 8.20 shows the incident power on the realistic undulator walls due the SR created by the full active length of the realistic undulator of the ILC-250 with nominal parameters before and after placing the photon masks. In addition, it shows the influence of the various photon masks of the different material candidates on the total deposited power at the undulator walls of the ILC-250. The total incident power at the realistic walls with Fe and Cu masks is $0.36 \text{ W} \pm 8 \%$ and $0.26 \text{ W} \pm 9 \%$, respectively, in the first meter of the module after Mask-21, while it is $0.035 \text{ W} \pm 40 \%$ with W masks. In the case of W masks, the error percentage of the deposited power becomes significant, and this is because that the W material stops up to 99.5 % of the deposited power since the W material has a high density.

In the case of the ideal masks, the maximum incident power is at the last meter of the last module upstream of the Mask-22. In contrast, in the case of realistic masks, whether it is Fe, Cu, or W, the maximum of the incident power becomes at the first meter of the first module downstream of the Mask-21, as shown in the bottom plots in figures 8.19 and 8.20. The incident power between the second meter of the first module downstream of Mask-21 and the last meter of the last module upstream of Mask-22 is caused by primary photons, meaning no secondary particles deposit in this region. That is why the agreement of the incident power is seen at this region.

The highest incident power is at the first meter of the first undulator module after Mask-22. This mask is located outside the undulator, showing the worst scenario of the total incident power. The most critical masks are those that are located inside the undulator. Therefore, the highest total incident power is downstream Mask-21 because it is the last mask inside the undulator line. For comparison, the incident power downstream Mask-20 is added. Table 8.5 summarizes the data of the incident power into the first undulator module after Mask-20, Mask-21, and Mask-22.

Results show that all considered materials can keep the incident power at the wall below the limit (1 W/m). In order to have almost the same amount of the incident power at the wall when a Cu mask with a length of 30 cm is used but with a shorter mask, tungsten can be used as a mask

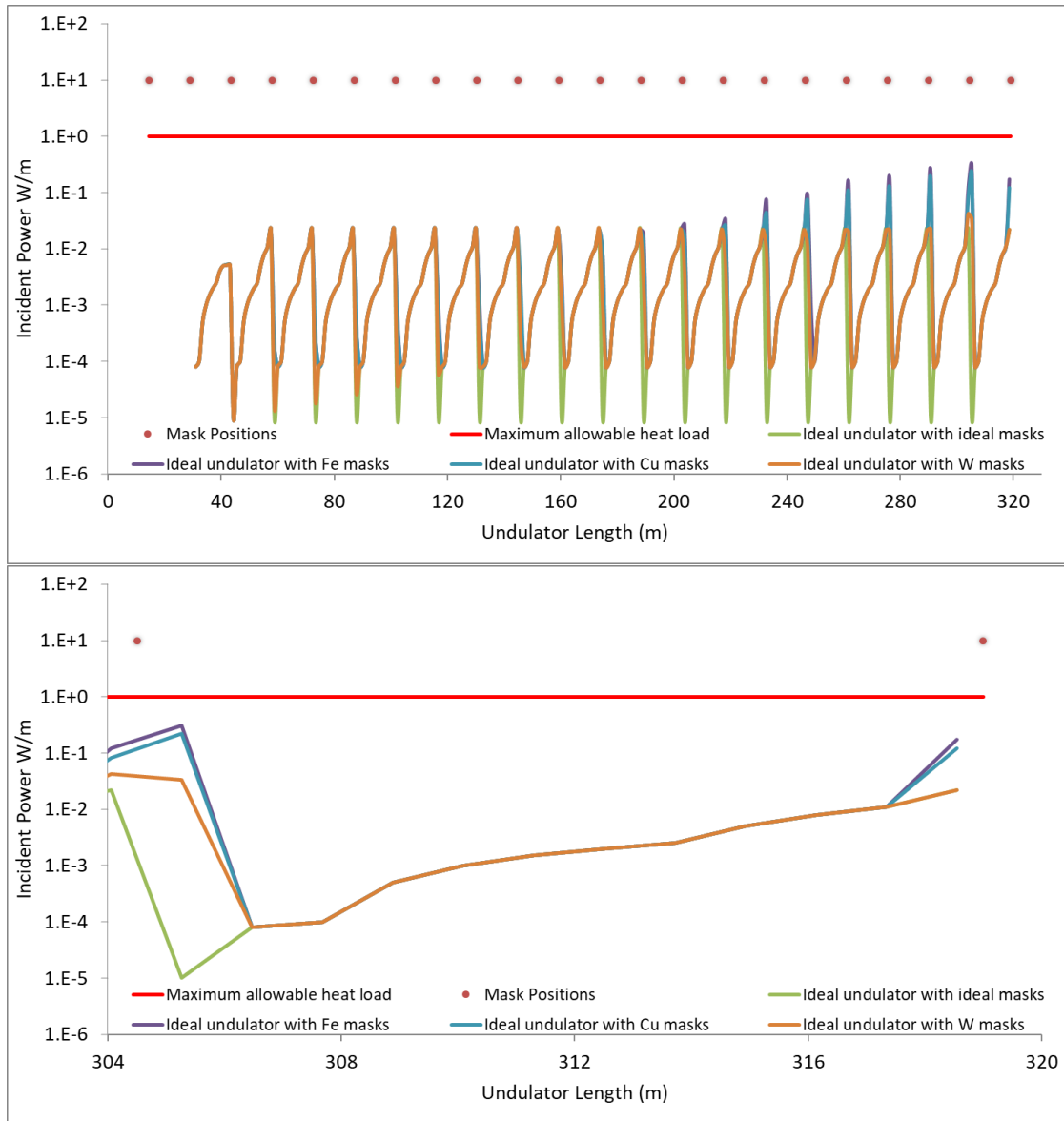


Figure 8.19: Incident power at undulator walls from the full active length of the **ideal** ILC-250. Green line represents the deposited power in undulator walls with ideal masks. Purple, blue and orange lines represent the total incident power in the wall with iron, copper and tungsten masks, respectively. Red points represent the position of the photon masks. Red line shows the acceptable limit of the incident power at the walls. Top plot shows the total incident power along the ILC-250 undulator line. Bottom plot shows the incident power between the last two masks (Mask-21 and Mask-22).

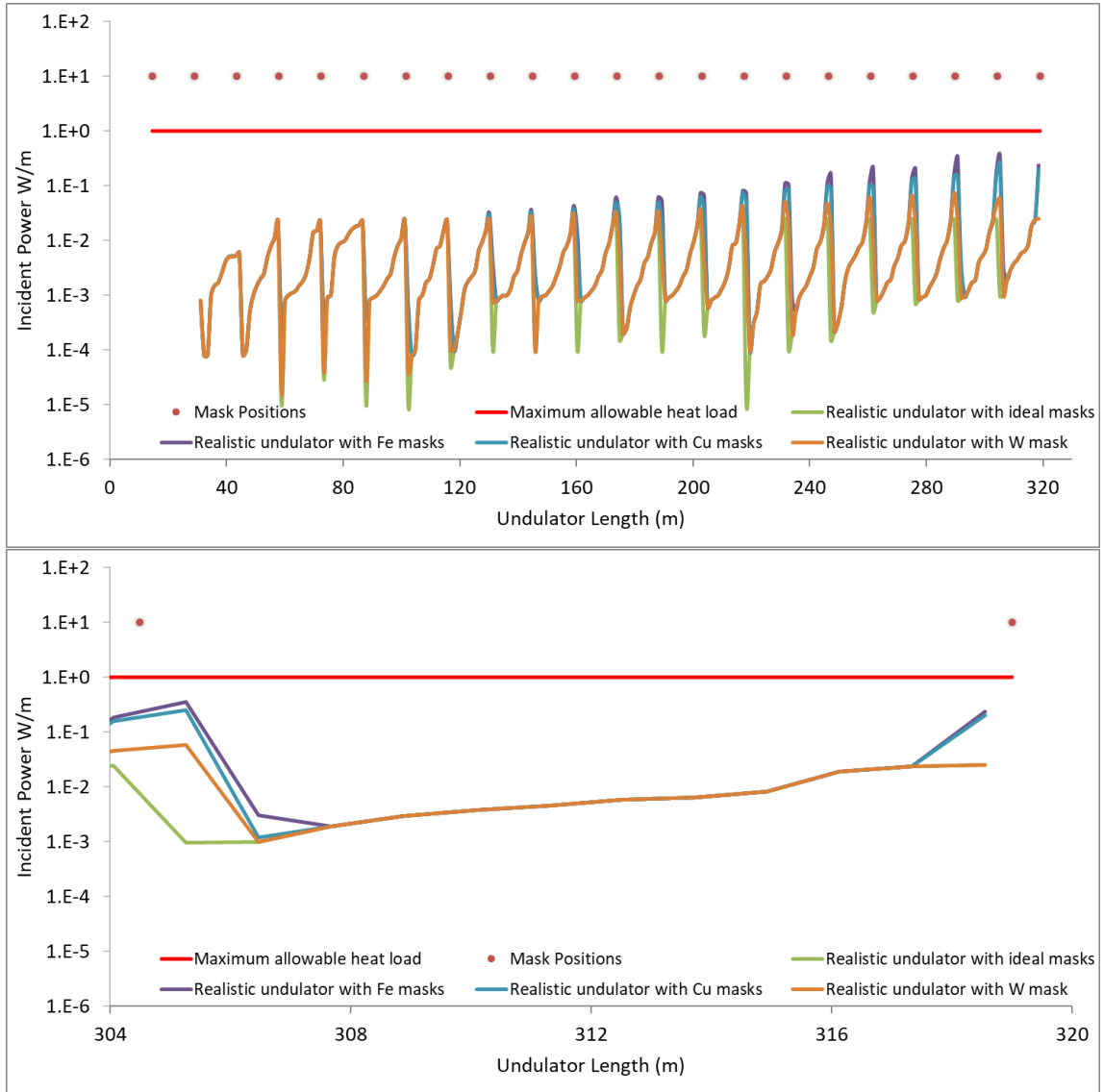


Figure 8.20: Incident power at undulator walls from the full active length of the **realistic** ILC-250. Green line represents the deposited power in undulator walls with ideal masks. Purple, blue and orange lines represent the total incident power in the wall with iron, copper and tungsten masks, respectively. Red points represent the position of the photon masks. Red line shows the acceptable limit of the incident power at the walls. Top plot shows the total incident power along the ILC-250 undulator line. Bottom plot shows the incident power between the last two masks (Mask-21 and Mask-22).

Table 8.5: Total deposited power (P_{wall}) into the first meter of the undulator wall downstream Mask-20, Mask-21 and Mask-22 for both ideal and realistic ILC-250 undulators using Fe, Cu and W material candidates.

Mask ID	Parameter	Material	Ideal	Error(%)	Real	Error(%)
20	P_{wall} (W/m)	<i>Fe</i>	0.23	5	0.32	8
		<i>Cu</i>	0.16	6	0.2	9
		<i>W</i>	0.023	21	0.024	25
21	P_{wall} (W/m)	<i>Fe</i>	0.31	5	0.36	8
		<i>Cu</i>	0.22	6	0.26	9
		<i>W</i>	0.034	30	0.035	40
22	P_{wall} (W/m)	<i>Fe</i>	0.45	4	0.46	6
		<i>Cu</i>	0.3	5	0.37	7
		<i>W</i>	0.04	12	0.042	22

material. In this case, the mask length can be reduced from 30 cm to 18 cm, keeping tapered section lengths at 5 cm for each.

8.9 Power Deposition in Photon Masks of the ILC-350 and ILC-500

Since the later stages in the ILC are to upgrade to 350 GeV and 500 GeV centre-of-mass energies, the deposited power at the photon masks of the ILC-350 and ILC-500 should be studied. In these two stages, the undulator is shorter; only 84 undulator modules are needed.

Since the opening angles of photons produced by helical undulator are determined by the energy of the electron beam, and a lower module number (84 modules) for the ILC-350 and ILC-500 options is needed to produce the required positron number compared to those needed for the ILC-250 option (132 modules), it is expected that the incident power at the photon masks for the high energy ILC options such as the ILC-350 and ILC-500 is lower than that for the ILC-250.

The ILC active undulator length is 231 m (132 modules), which is needed to produce the required positron number for the first stage (the ILC-250). For higher stages, such as the ILC-350 and ILC-500, the required active length is 147 m (84 modules). It means that operators can run any 84 undulator modules for higher stages, whether from the beginning, middle, or end. The worst result for the deposited energy at the masks is to use the first 84 modules. In contrast, the best result is to use the last 84 modules. In order to study the worst scenario of the deposited power at photon masks, the first 84 undulator modules are considered to be simulated for both ILC-350 and ILC-500 options in this study. The HUSR code is used to simulate the photon distribution produced by both ideal and realistic undulators of the ILC-350 and ILC-500.

8.9.1 Result

The deposited energy along Fe, Cu, and W Mask-22 for both ideal and realistic undulators is shown in figures 8.21 and 8.22 for the ILC-350 and ILC-500 options with the nominal parameters, respectively. In addition, figures 8.23 and 8.24 show the maximum deposited energy along both Z-direction and radial direction of the mask length in Fe, Cu, and W Mask-22 for both ideal and realistic undulators of the ILC-350 and ILC-500 with the nominal parameters, respectively. Table 8.6 summarizes the result studies.

In the case of the ILC-350, the average incident photon energies are 2.54 and 2.74 MeV for both ideal and realistic undulators, respectively. The deposited power at Mask-22 is 186 and 205 W for both ideal and realistic undulators, respectively. In the case of the ILC-500, the average incident photon energies are 1.75 and 1.86 MeV for both ideal and realistic undulators, respectively. The deposited power at Mask-22 is 21 and 23 W for both ideal and realistic undulators, respectively. In contrast, in the case of the realistic ILC-250, the deposited power and average incident photon

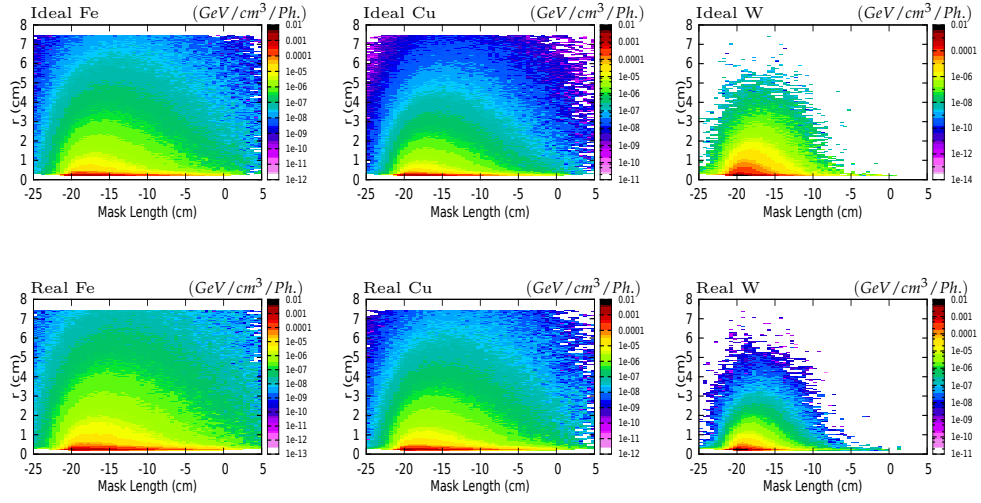


Figure 8.21: The deposited energy along the Fe , Cu and W Mask-22 for **the ILC-350**. Top (Bottom) plots show the energy deposition in case of ideal (realistic) undulators.

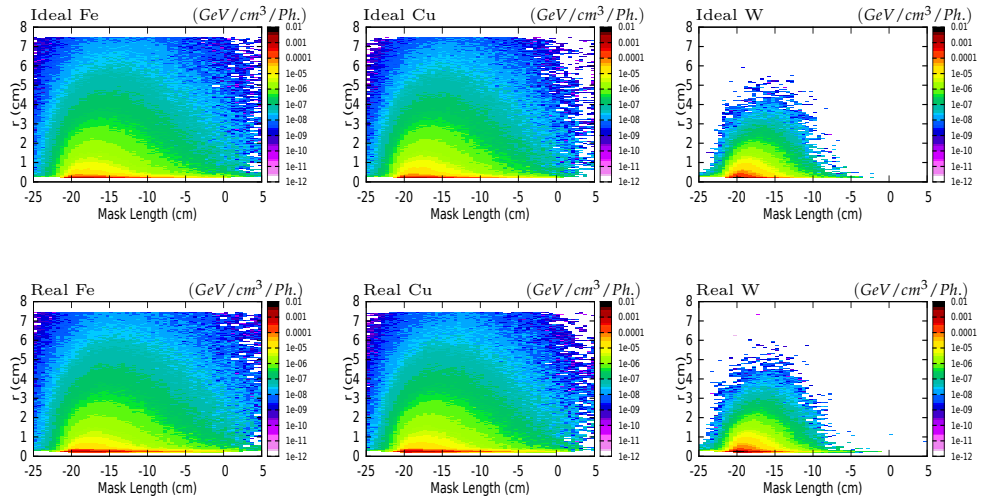


Figure 8.22: The deposited energy along the Fe , Cu and W Mask-22 for **the ILC-500**. Top (Bottom) plots show the energy deposition in case of ideal (realistic) undulators.

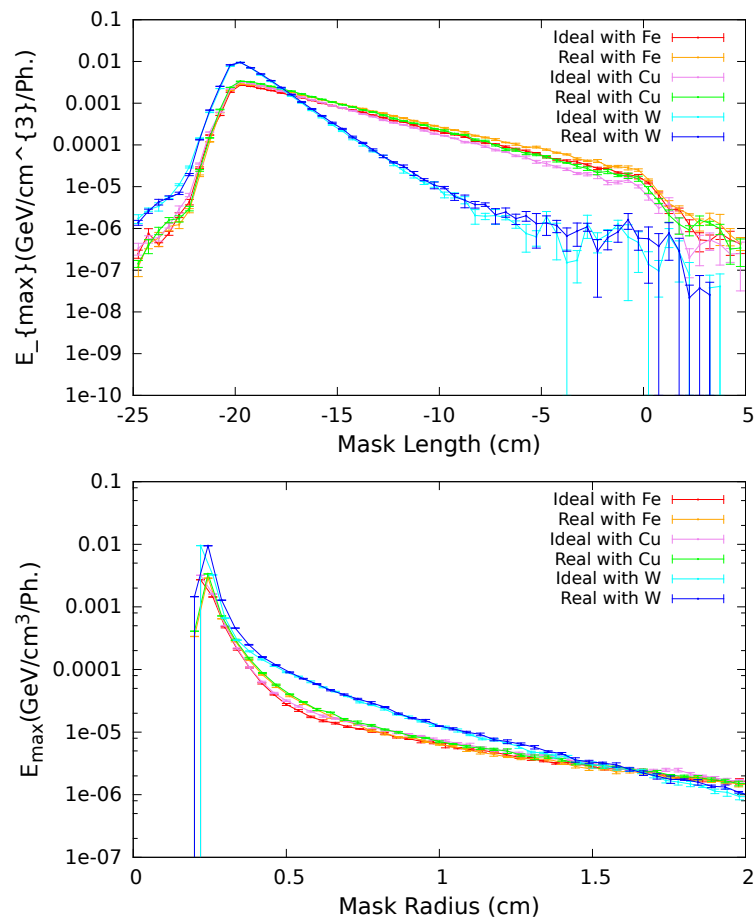


Figure 8.23: The maximum deposited energy (GeV/cm³/photon) along iron, copper and tungsten Mask-22 for both ideal and realistic undulators of **the ILC-350**. The upper (bottom) plot shows the maximum deposited energy along Z-direction (radial) mask length.

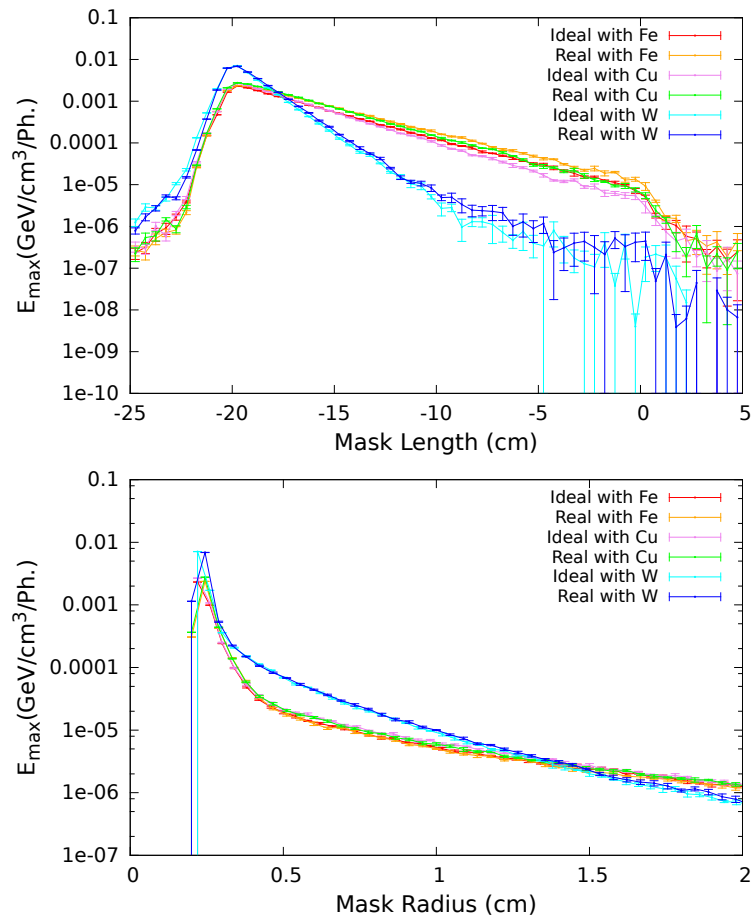


Figure 8.24: The maximum deposited energy ($\text{GeV}/\text{cm}^3/\text{photon}$) along iron, copper and tungsten Mask-22 for both ideal and realistic undulators of **the ILC-500**. The upper (bottom) figure shows the maximum deposited energy along Z-direction (radial) mask length.

Table 8.6: Average incident photon energy (E_{ave}^γ), deposited power (P_{mask}), incident photon number (N_{mask}^γ), maximum deposited energy (E_{max}), peak energy deposition density (PEDD), temperature rise (ΔT_{max}) using three different materials for Mask-22 for both ideal and realistic undulators and power stopped by these masks (P_{stop}^{mask}) for the ILC-350 and ILC-500.

Centre-of-mass energies		350 GeV		500 GeV	
Parameters	<i>Material</i>	<i>Ideal</i>	<i>Real</i>	<i>Ideal</i>	<i>Real</i>
E_{ave}^γ (MeV)		2.54	2.74	1.75	1.86
P_{mask} (W)		186	205	21	23
N_{inc}^γ per Pulse ($\times 10^{13}$)		9.16	9.34	1.48	1.56
E_{max} (MeV/cm ³ /Ph.)	<i>Fe</i>	2.7	2.9	2.3	2.4
	<i>Cu</i>	3.16	3.3	2.6	2.7
	<i>W</i>	9.4	9.5	6.9	7.0
PEDD (J/g/Pulse)	<i>Fe</i>	5.02	5.49	0.68	0.74
	<i>Cu</i>	5.17	5.50	0.69	0.75
	<i>W</i>	7.14	7.36	0.85	0.91
ΔT_{max} (K)	<i>Fe</i>	11.15	12.20	1.53	1.69
	<i>Cu</i>	13.43	14.30	1.78	1.95
	<i>W</i>	53.27	54.89	6.32	6.76

energy at Mask-22 are 361 W and 2.14 MeV, respectively.

8.10 The Deposited Power at the Undulator Walls in Case of the ILC Luminosity upgrade

The ILC luminosity upgrade is the luminosity by doubling the number of bunches per pulse from 1312 to 2625. As a result, the average photon beam power is also doubled. The changes are on the main linac RF parameters. The bunch spacing will be reduced from 554 ns to 366 ns, and this leads to an increase in beam current from 5.8 mA to 8.8 mA, and the beam pulse length is increased from 727 μ s to 961 μ s. Table 8.7 compares the main linac RF parameters for the baseline and luminosity upgrade.

Table 8.7: The main linac RF parameters for the baseline and luminosity upgrade [11].

Parameter	Unit	Baseline	Luminosity upgrade
Bunches per pulse		1312	2625
Bunch spacing	ns	554	366
Beam current	mA	5.8	8.8
Beam pulse length	s	727	961

We aim to check if the proposed ILC photon mask system can also keep the deposited power in the undulator walls below the limited level. Table 8.8 compares the highest deposited power at the realistic undulator wall of the ILC-250 for both cases; the baseline and luminosity upgrade.

Table 8.8: The deposited power at the first meter of the realistic undulator module downstream the Mask-21 in the ILC-250 for different materials for both cases; the baseline and luminosity upgrade.

	Mask material	<i>Baseline</i>	Luminosity upgrade
Deposited power (W/m)	<i>Fe</i>	0.31	0.62
	<i>Cu</i>	0.22	0.44
	<i>W</i>	0.034	0.068

The study shows that all material candidates will keep the deposited power at the realistic undulator wall of the ILC-250 below the limited level which is 1 W/m. However, the maximum instantaneous stresses in the case of the ILC luminosity upgrade are about a factor of 2 higher than that in table 8.4. The maximum instantaneous stress is still below the tensile strength of all material candidates. In other words, the studies in section 8.6 show that the stress inside the mask is below the recommended limit for the high cycle fatigue load. However, in the realistic case of the luminosity upgrade for the ILC-250 the cyclic stress in a small area of the Mask-22 reaches and could even exceed the recommended fatigue limit. Given the small size of this spot it is unlikely that the mask material will fail.

Chapter 9

The ILC Photon Beam Power and Polarization

In this chapter, simulations are conducted for the photon beam power and polarization at the target plane assuming both ideal and realistic undulators for all ILC energy options. The ILC baseline options, i.e., using the helical undulator positron source, provide a positron beam polarization of $\approx 30\%$. Comparing the photon beam polarization for ideal and realistic undulators gives a measure of how the positron beam polarization is changed for a realistic undulator. Therefore, the influence of the realistic undulator on the photon beam power and polarization for all ILC energy options is studied. In addition, the effect of placing photon masks along the undulator line on the photon beam power and polarization is investigated for both ideal and realistic undulators. To increase the positron beam polarization, it is planned to insert a photon collimator between the undulator and the target. The efficacy of such photon collimator is considered for the case of the realistic undulator.

9.1 Photon Beam Polarization

One of the most important reasons to choose the helical undulator-based positron source as the baseline in the ILC project is to produce a polarized positron beam. The circular polarization of the photon beam is transferred to the longitudinal polarization of the positron (and electron) beam [65]. This means that increasing the photon beam polarization will in turn increase the polarization of the positron beam that they create. The photon beam polarization depends on the undulator parameters. The effect of undulator parameters such as λ_u , K value and E_e on the photon beam polarization and spectrum is discussed in chapter 5.

The strong relationship between the energy, opening angle and polarization of the produced photon beam in the undulator is clear as seen in figures 7.13 and 7.14. So the photon beam with a large considered beam size has a low polarization. It means that the average photon beam polarization and the average photon beam energy can be improved by removing photons far from the undulator axis. Since the degree of the positron beam polarization depends on the degree of the photon beam polarization that hits the target, the degree of the photon beam polarization can be controlled by adjusting the photon collimator aperture. Decreasing the collimator aperture, of course, leads to a higher degree of polarization. On the other hand, the photon collimator reduces the photon intensity at the target. It means that the photon beam polarization can be increased, but at the expense of some reduction in the number of photons. Although a longer helical undulator could compensate, the load at the undulator wall, photon collimator, and target components will be high. Therefore, the photon beam polarization and intensity at the target should be discussed simultaneously.

9.2 The Photon Beam and Polarization Distribution

The HUSR code, which was introduced in chapter 7, has been used to simulate the distribution of the photon beam power and polarization at the ILC target plane. The simulation was conducted for both ideal and realistic cases of helical undulators. Tables 2.1 and 6.1 show the nominal ILC parameters that are needed to produce the required positron yield of $\approx 1.5 e^+/e^-$ at the positron DR for all three centre-of-mass energies (E_{cm}) 250 GeV, 350 GeV and 500 GeV. In all of these energy options the polarization of the resulting positron beam is about 30 % without photon collimators.

Figure 9.1 shows the distribution of the photons and polarization of the photon beam at the target plane produced by one ILC-250 undulator module with 1.75 m length for both ideal and realistic cases of undulators. The distance between this module and the target plane is 401 m. Figures 9.2 and 9.3 show the ideal and realistic photon beam distribution and polarization in 3D and contour plots, respectively, produced by the full active length of the ILC-250 helical undulator. In the case of ideal undulators, the photon beam distribution is symmetric around the center while it is no longer this way in the case of the realistic undulator. Therefore, the power, average energy and polarization of the photon beam are lower in the case of the realistic undulator compared with those in the case of the ideal undulator. Table 9.1 summarizes the study results.

Table 9.1: The power (P_{target}), average energy (E_{ave}^γ) and polarization (P_γ) of the photon beam at the ILC-250 target plane for ideal and realistic undulators with $K = 0.85$.

	$P_{target}(kW)$	$E_{ave}^\gamma(MeV)$	P_γ (%)
Ideal undulators	62.5	7.6	36.0
Realistic undulators	61.0	7.3	34.0

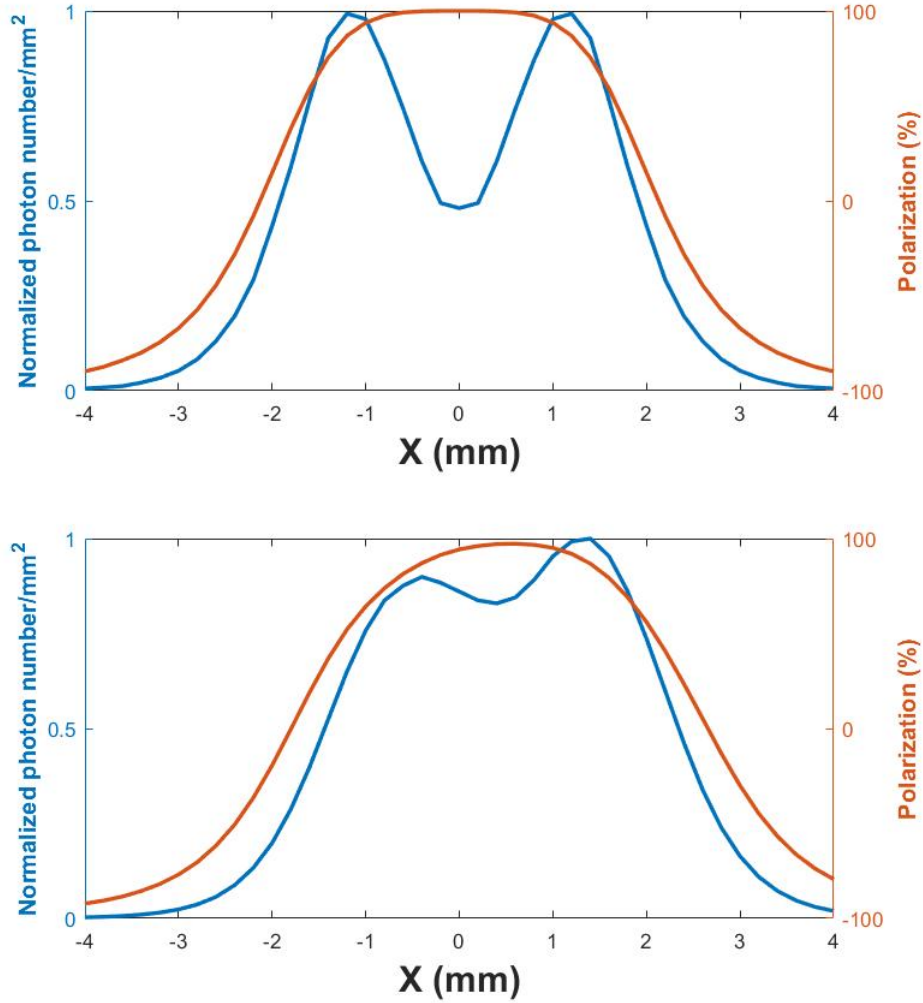


Figure 9.1: The upper (bottom) plot shows the ideal (realistic) distribution of the photon number and photon beam polarization at the target plane produced by passing an electron beam with energy of 126.5 GeV through one ILC-250 undulator module with 1.75 m length, $K = 0.85$, $B = 0.79$ T, $\lambda_u = 11.5$ mm. The distance between this module and the target plane is 401 m. These data are plotted as a function of X when $Y=0$.

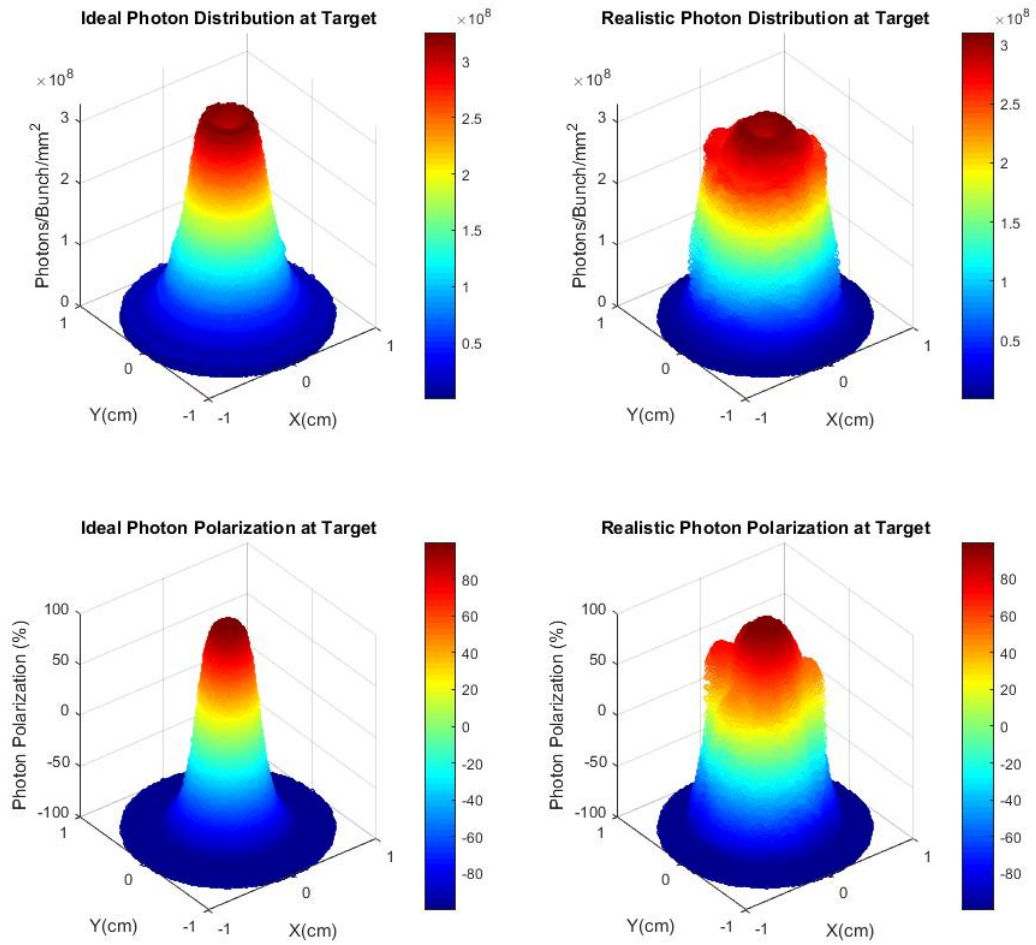


Figure 9.2: The ideal (left plots) and realistic (right plots) distributions of the photons (upper plots) and of the photon beam polarization (bottom plots) produced by the full active length undulator of the ILC-250 with $K = 0.85$ at the target plane in 3D.

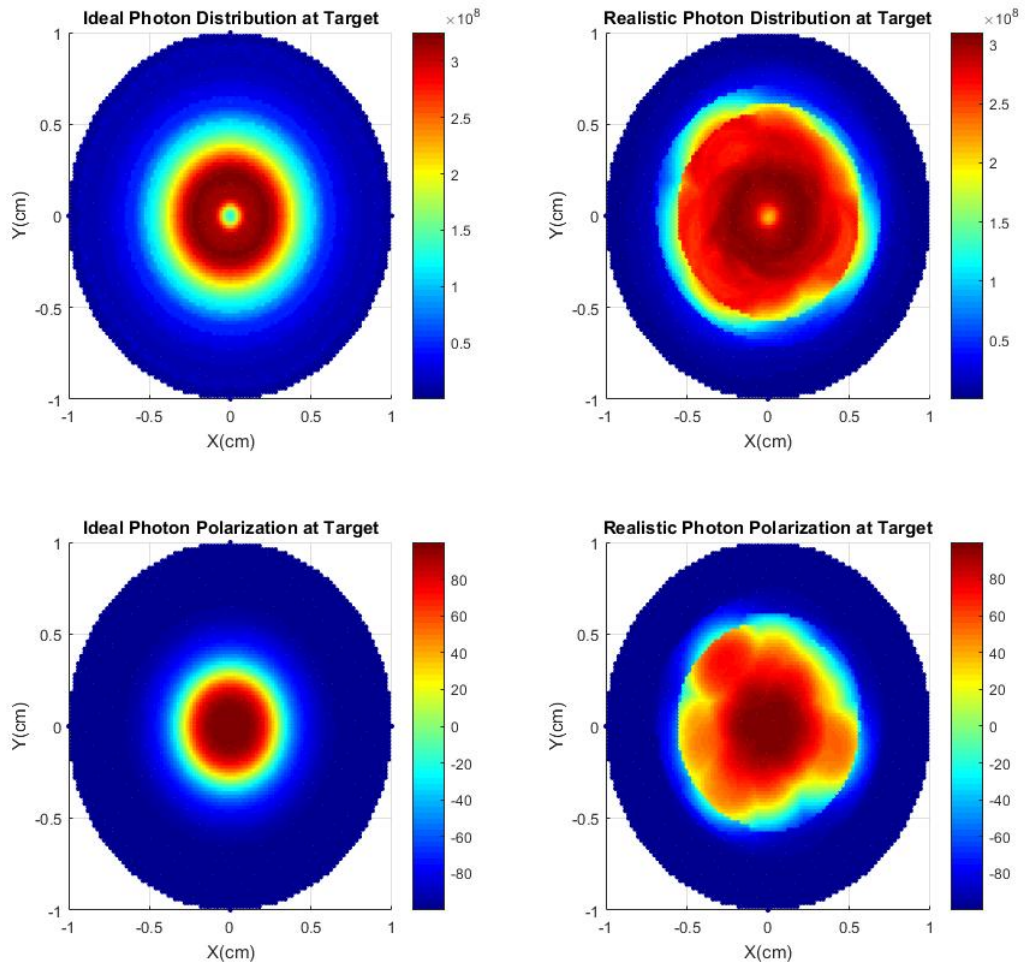


Figure 9.3: The ideal (left plots) and realistic (right plots) distributions of the photons (upper plots) and of the photon beam polarization (bottom plots) produced by the full active length undulator of the ILC-250 with K 0.85 at the target plane in contour plots.

9.3 The Effect of Photon Masks on Photon Beam Power and Polarization

The study in chapter 8 demonstrated that 22 photon masks must be placed along the undulator line to keep the deposited power at undulator walls below the maximum allowable limit. Since the photon masks must have a smaller radius than the radius of the undulator aperture, masks will stop photons that do not pass through the hole of masks, resulting in changes in the average energy, power, and polarization of the photon beam at the target. The thermal load and design of photon masks were discussed in chapter 8. Photons stopped by the photon masks will only be minor contributors to the positron production. They are usually at the very outer part of the photon beam spot. In most cases, the electron-positron pair produced by these photons is not matched with the OMD. Therefore, these masks are not very important for positron production, although they will slightly reduce the load at the target. Nevertheless, the impact of placing these masks on the average energy, power, and polarization of the photon beam at the target plane is studied here.

9.3.1 $E_{cm} = 250$ GeV Option

The initial stage of the ILC project is $E_{cm} = 250$ GeV. At this stage, the entire active length of the undulator with a K factor of 0.85 ($B_{axis} = 0.79$ T) and $\lambda_u = 11.5$ mm is used to produce the required intensity of photon beam. The rest parameters are shown in tables 2.1 and 6.1. The photon beam power and polarization of the ILC-250 were simulated before and after placing the photon mask along the undulator line.

9.3.2 $E_{cm} = 350$ GeV and 500 GeV Options

Since the later stages of the ILC project are the ILC-350 and ILC-500, the effects of the photon masks on the power and polarization of the photon beam are studied here. As shown in tables 2.1 and 6.1, only 147 m active length (84 modules) are needed to produce the required positron number in case of both stages; ILC-350 and ILC-500. Since, the total active length of the ILC undulator is 231 m (132 modules), operators should choose 84 out of 132 modules, whether from the beginning, middle, or end of the undulator line. To study the worst-case scenario of the power distribution at the target, the first 84 modules are chosen.

At the stage of $E_{cm} = 350$ GeV, a 178 GeV electron beam passes through a helical undulator with an active length of 147 m with a K factor of 0.75 ($B_{axis} = 0.698$ T) and $\lambda_u = 11.5$ mm in order to produce the required intensity of photon beam. In the case of $E_{cm} = 500$ GeV, the electron beam with an energy of 253 GeV is sent through the undulator with parameters of a K factor of

0.45 ($B_{axis} = 0.42$ T). To study the effect of the masks, the photon beam power and photon beam polarization of the ILC-350 and ILC-500 are simulated before and after placing the photon mask along the undulator line.

9.4 HUSR Photon Collimator

The photon collimator in HUSR was implemented as a simple geometric cut. The only parameter required to be added by the user of the HUSR is the collimator radius. Photons are produced when the electron beam is tracked into the helical undulator. Some of these photons will pass through the collimator aperture, and some will not. So, if a photon passes through the aperture, it will be recorded by the observation points that are present in the target plane. In contrast, if the photon does not pass through the aperture of the collimator, its energy will be added to the deposited energy at the collimator, and in this case, the tracking ends. Since HUSR can not simulate the electromagnetic shower, no secondary particles can emit from the HUSR collimator to the target.

There are some reasons for placing a photon collimator before the target. First, a protection system is needed to protect the target system against damage. Since the high photon flux may cause some problems for the target components through heating and radiation damage. Also, as we learned from the photon beam distribution, most photons with low energy (< 2 MeV) have larger opening angles. These photons will raise the energy deposition in the target, which leads to an increase in the temperature and activation.

In addition to that, these photons with a low energy will not create much positrons. Therefore, placing a photon collimator just before the target to cut off these photons may provide advantages, such as increasing the positron production efficiency with no an increase in the energy deposition. This can be done by decreasing the aperture of the photon collimator. In addition, the polarization of the outer part of the photon beam is low. Therefore, removing the outer part of the photon beam will increase the average polarization of the photon beam. This leads to increasing polarization of the produced positron beam, which can increase the effective luminosity.

The ILC TDR shows that a photon collimator is placed in front of the target. Different designs have been discussed in the past, such as in [66]. A detailed study in [67] proposed a possible photon collimator system for all ILC energy options. This study shows a multi-stage photon collimator system for three different centre-of-mass energies, including 250, 350, and 500 GeV.

The influence of different photon collimator radii on the power, average energy, and polarization of the photon beam in the target plane of all ILC energy options for both ideal and realistic undulator cases is studied.

9.5 Result

The photon beam power and polarization produced by both ideal and realistic undulators using three different centre-of-mass energies are simulated before and after placing the masks. In addition, the effect of placing a photon collimator just before the target on the photon beam power and polarization produced by all ILC options in both ideal and realistic undulator cases is shown.

9.5.1 The Effect of Photon Masks on Photon Beam Parameters

The influence of placing 22 photon masks along the ILC undulator line on the power, average energy, and polarization of the photon beam for all three ILC options for both ideal and realistic undulator cases is studied. In this section, we consider all photons that reach the target plane.

9.5.1.1 $E_{cm} = 250$ GeV Option

The simulation results of the spectrum and polarization of the photon beam at the ILC-250 target for both ideal and realistic undulators before and after placing photon masks are shown in plots in figure 9.4.

Table 9.2 summarizes the simulation results. In both ideal and realistic undulator cases, placing

Table 9.2: Power (P_{target}), average energy (E_{ave}^γ) and polarization (P_γ) of the photon beam at the ILC-250 target plane for ideal and realistic undulators with $K = 0.85$ without and with masks.

		$P_{target}(kW)$	$E_{ave}^\gamma(MeV)$	P_γ (%)
Ideal undulators	No masks	62.5	7.6	36.0
	With masks	60.2	8.0	37.3
Realistic undulators	No masks	61.0	7.3	34.0
	With masks	59.0	7.7	35.7

masks can improve the average energy of the photon beam at the target plane by ≈ 4 %, while the photon beam power decreases by ≈ 4 %. The photon masks can slightly increase the photon beam polarization from 36.0 % to 37.3 % in the ideal case and from 34.0 % to 35.7 % in the realistic case.

9.5.1.2 $E_{cm} = 350$ GeV and 500 GeV Options

The power and polarization of the photon beam at the target plane produced by both ideal and realistic ILC-350 and ILC-500 undulators before and after placing the photon masks are simulated to investigate the influence of the photon masks on the photon beam parameters.

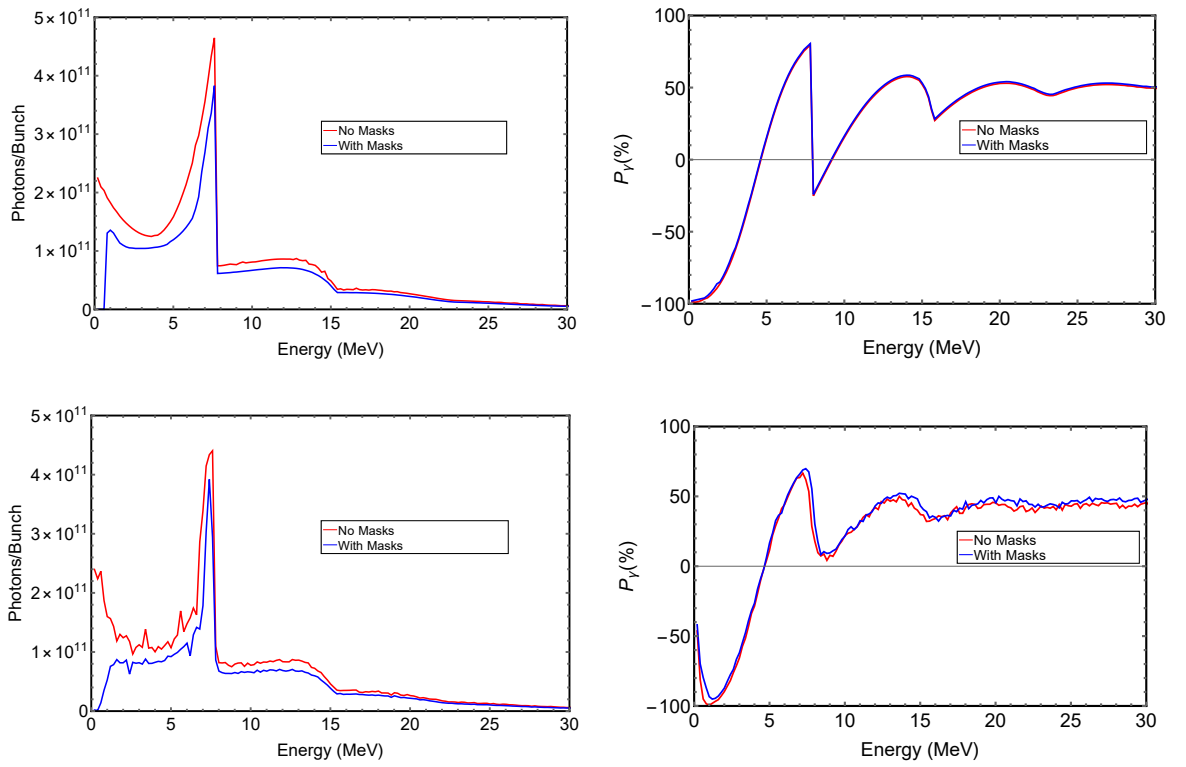


Figure 9.4: The ideal (top) and realistic (bottom) spectrum (left) and circular polarization (right) of the photon beam at the **ILC-250** target plane. A 128 GeV electron beam passes through an undulator with 231 m active length, $K = 0.85$, $B = 0.79$ T, $\lambda_u = 11.5$ mm. The red (blue) line shows the photon beam spectrum and polarization before (after) placing photon masks.

Plots in figure 9.5 show the energy spectrum and polarization of the photon beam at the target for 350 GeV centre-of-mass energy before and after placing photon masks produced by both ideal and realistic undulators with $K = 0.75$, respectively. Plots in Figure 9.6 show the same, but in the case of the ILC-500.

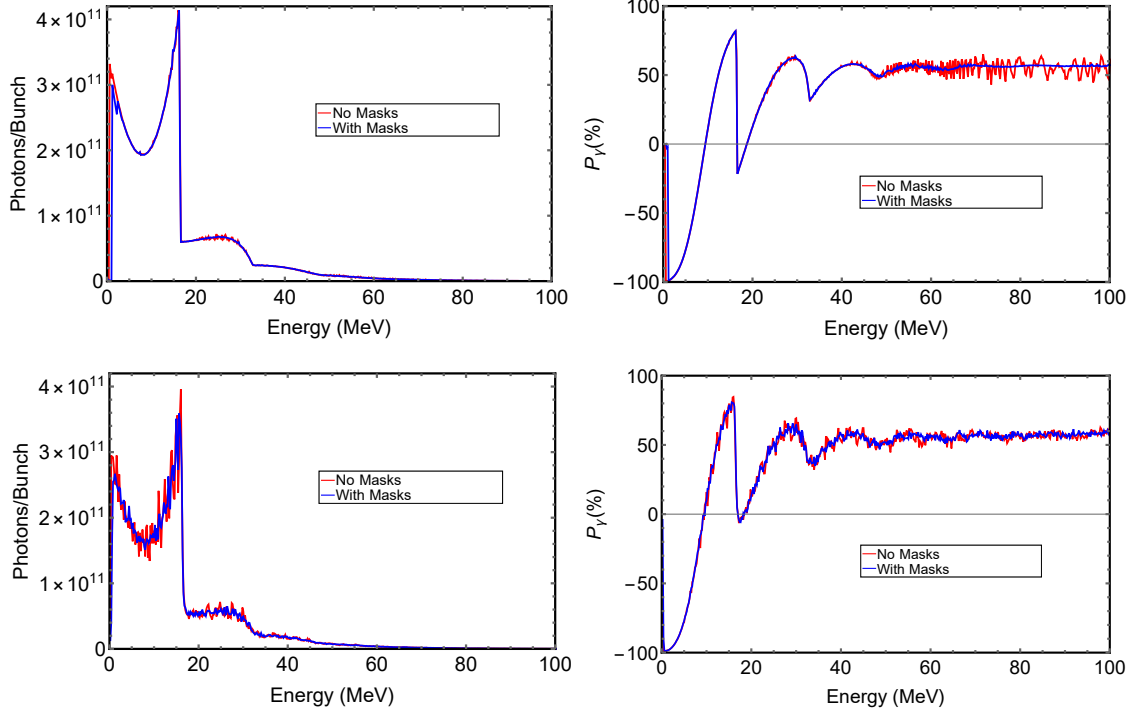


Figure 9.5: The ideal (top) and realistic (bottom) spectrum (left) and circular polarization (right) of the photon beam at the **ILC-350** target plane. A 173 GeV electron beam passes through an undulator with 147 m active length, $K = 0.75$, $B = 0.70$ T, $\lambda_u = 11.5$ mm. The red (blue) line shows the photon beam spectrum and polarization before (after) placing photon masks.

Tables 9.3 and 9.4 show the average energy, power, and polarization of the photon beam at the target before and after placing photon masks produced by both ideal and realistic undulators for both ILC-350 and ILC-500, respectively.

Table 9.3: Power (P_{target}), average energy (E_{ave}^γ) and polarization (P_γ) of the photon beam at target plane for ideal (realistic) undulators with $K = 0.75$ without and with masks for the ILC-350.

		$P_{target}(kW)$	$E_{ave}^\gamma(MeV)$	$P_\gamma(\%)$
Ideal undulators	No masks	60.0	14.0	38.0
	With masks	59.2	14.3	38.2
Realistic undulators	No masks	58.2	13.6	37.9
	With masks	57.0	13.8	38.0

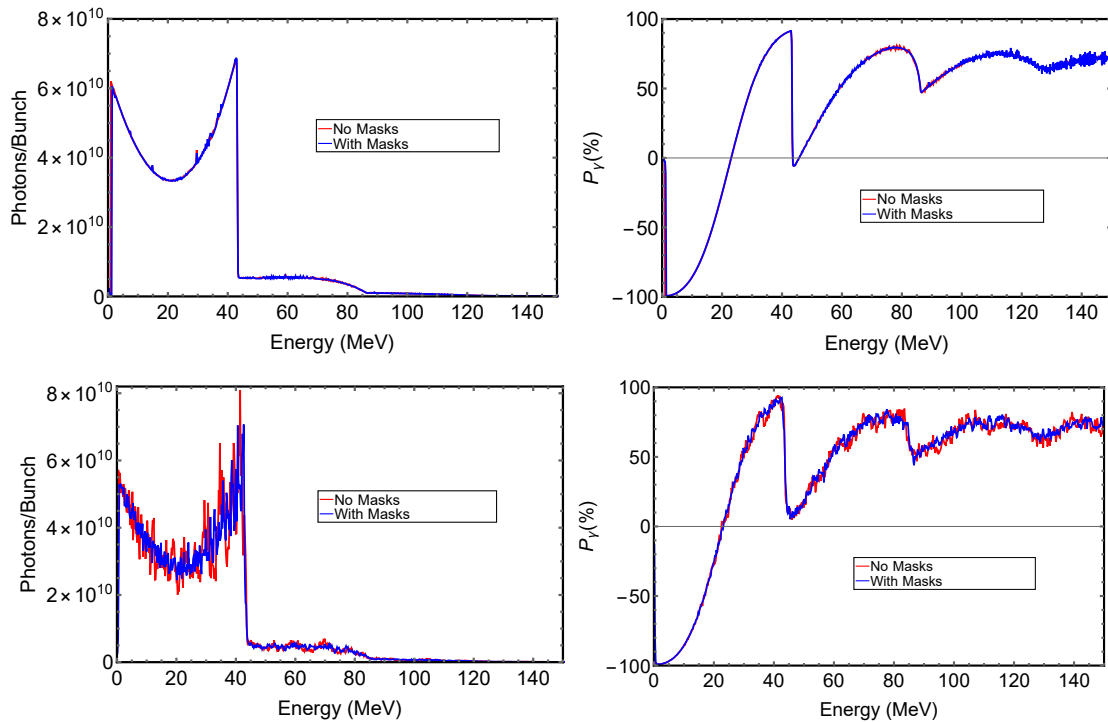


Figure 9.6: The ideal (top) and realistic (bottom) spectrum (left) and circular polarization (right) of the photon beam at the **ILC-500** target plane. A 253 GeV electron beam passes through an undulator with 147 m active length, $K = 0.45$, $B = 0.42$ T, $\lambda_u = 11.5$ mm. The red (blue) line shows the photon beam spectrum and polarization before placing photon masks.

Table 9.4: Power (P_{target}), average energy (E_{ave}^γ) and polarization (P_γ) of the photon beam at target plane for ideal (realistic) undulators without and with masks for the ILC-500 with $K = 0.45$.

		$P_{target}(kW)$	$E_{ave}^\gamma(MeV)$	P_γ (%)
Ideal undulators	No masks	43.4	26.5	43.9
	With masks	43.3	27.0	44.1
Realistic undulators	No masks	43.1	25.4	43.5
	With masks	42.8	25.7	43.1

The results in this study show that the influence of the photon masks on the photon beam parameters in the target plane of all ILC energy options is negligible for the positron production.

9.5.2 The Effect of the Photon Collimator on Photon Beam Parameters

A photon collimator with different diameters is used for all ILC energy options to investigate the influence of the diameter of the photon collimator on the photon beam parameters.

Plots in figure 9.7 show the spectrum and polarization of the photon beam at the ILC-250 target plane for both ideal and realistic undulator cases using a photon collimator with different radii. Plots in figures 9.8 and 9.9 show the spectrum and polarization of the photon beam at the ILC-350 and ILC-500 target plane for both ideal and realistic undulator cases using a photon collimator with different radii including 1, 2, 5 and 10 mm.

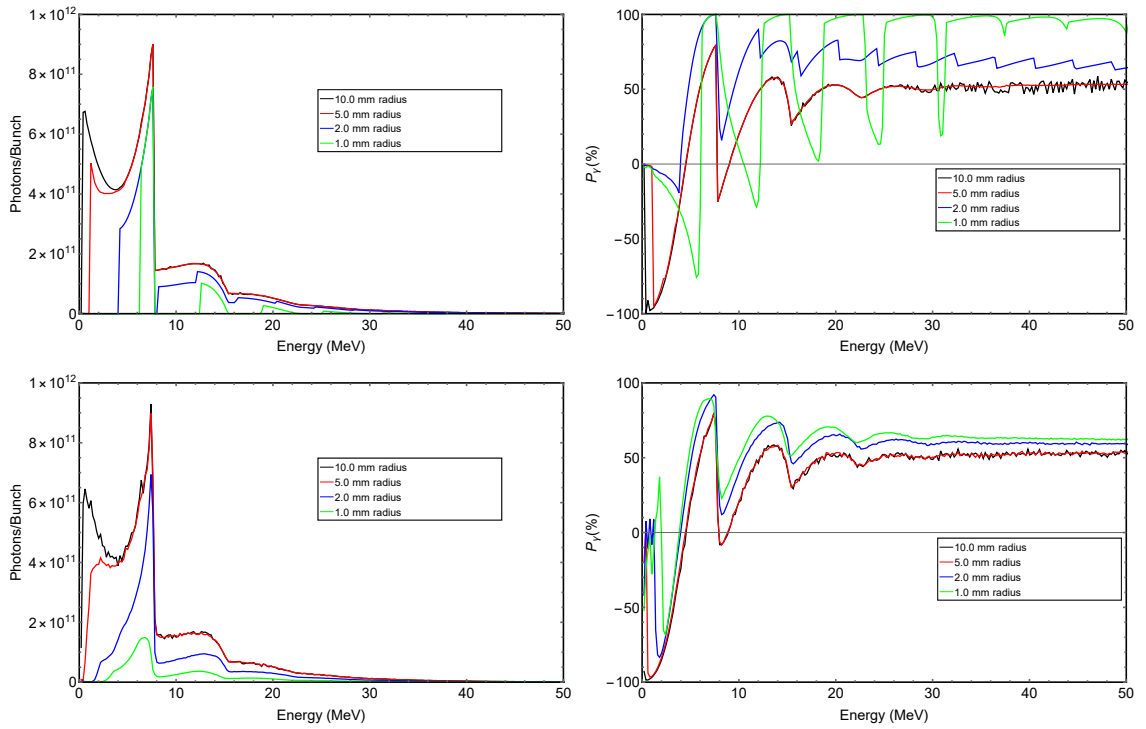


Figure 9.7: The ideal (top) and realistic (bottom) spectrum (left) and circular polarization (right) of the photon beam produced by the **ILC-250** undulator with K 0.85 at the target plane with different photon collimator apertures. Each colour represents a different photon collimator radius, including 10, 5, 2 and 1 mm.

Tables 9.5 and 9.6 summarize the study results. For ILC-250, a collimator radius below 5 mm will influence considerably the photon beam polarization, for ILC-350 a radius below 3 mm and for ILC-500 a radius below 2 mm are necessary.

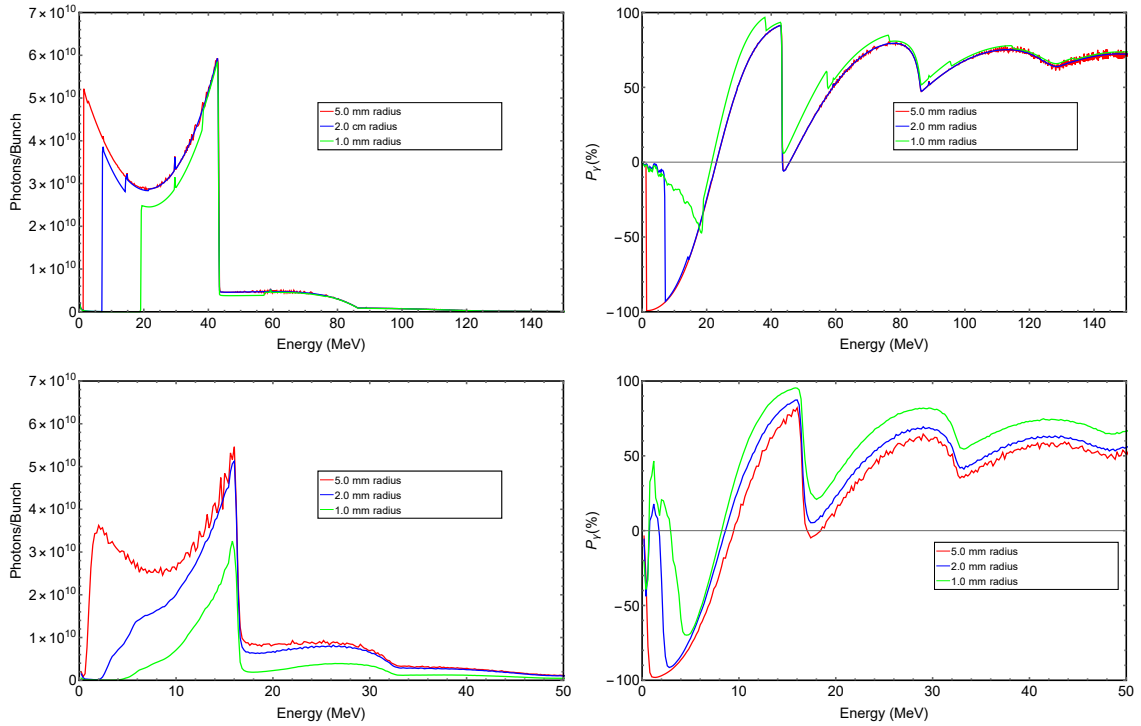


Figure 9.8: The ideal (top) and realistic (bottom) spectrum (left) and circular polarization (right) of the photon beam produced by the **ILC-350** undulator with $K = 0.75$ at the target plane with different photon collimator apertures. Each colour represents a different photon collimator radius, including 5, 2 and 1 mm.

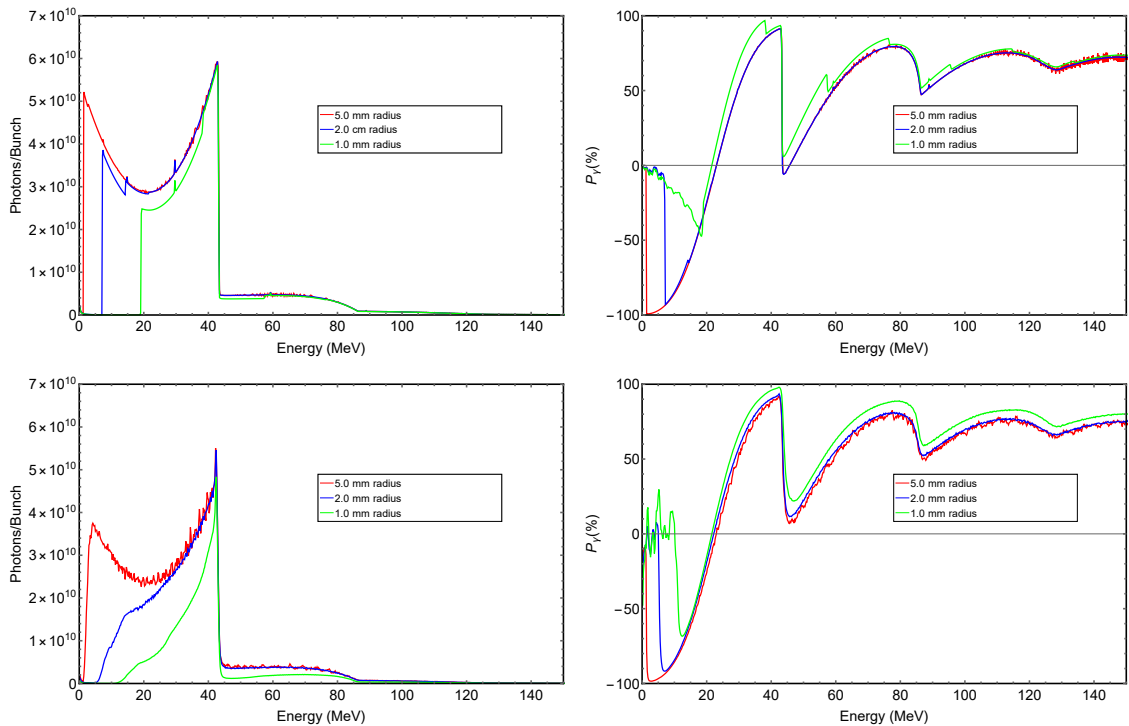


Figure 9.9: The ideal (top) and realistic (bottom) spectrum (left) and circular polarization (right) of the photon beam produced by the **ILC-500** with $K = 0.45$ at target plane with different photon collimator apertures. Each colour represents a different photon collimator radius, including 5, 2 and 1 mm.

Table 9.5: The power (P_{target}), average energy (E_{ave}^γ) and polarization (P_γ) of the photon beam at target plane for ideal and realistic undulators with different photon collimator radii (10.0 mm up to 4.0 mm) for three different ILC energy options; ILC-250 with $K = 0.85$, ILC-350 with $K = 0.75$ and ILC-500 with $K = 0.45$.

Photon collimator		Centre-of-mass energy (GeV)					
		250		350		500	
radius (mm)	<i>Parameters</i>	<i>Ideal</i>	<i>Real</i>	<i>Ideal</i>	<i>Real</i>	<i>Ideal</i>	<i>Real</i>
10.0	$E_{ave}(MeV)$	7.7	7.5	14.1	13.7	27.4	25.9
	$P_\gamma(\%)$	36.6	35.4	38.0	36.9	44.6	43.5
	$P_{target}(kW)$	61.5	60.0	59.4	58.0	43.2	40.8
9.0	$E_{ave}(MeV)$	7.9	7.6	14.2	13.7	27.5	26.0
	$P_\gamma(\%)$	36.94	35.5	38.1	36.9	44.7	43.6
	$P_{target}(kW)$	61.2	59.7	59.3	57.9	43.2	40.7
8.0	$E_{ave}(MeV)$	8.0	7.7	14.3	13.8	27.6	26.1
	$P_\gamma(\%)$	37.3	35.7	38.2	37.0	44.8	43.7
	$P_{target}(kW)$	60.5	59.0	59.2	57.0	43.2	40.6
7.0	$E_{ave}(MeV)$	8.2	7.9	14.5	14.55	27.7	26.2
	$P_\gamma(\%)$	37.5	37.0	38.6	37.6	44.9	43.8
	$P_{target}(kW)$	60.2	58.9	59.1	56.9	43.2	40.5
6.0	$E_{ave}(MeV)$	8.4	8.1	14.7	14.86	28.0	26.3
	$P_\gamma(\%)$	37.8	37.7	38.8	37.7	45.0	43.9
	$P_{target}(kW)$	60.0	58.3	59.0	56.7	43.2	40.3
5.0	$E_{ave}(MeV)$	8.6	8.4	15.0	15.16	28.4	26.5
	$P_\gamma(\%)$	38.9	39.3	39	37.9	45.1	44.0
	$P_{target}(kW)$	59.8	58.0	58.9	56.6	43.1	40.2
4.0	$E_{ave}(MeV)$	9.2	8.8	15.9	15.71	29.2	27.8
	$P_\gamma(\%)$	42.0	43.8	40.0	38.8	45.4	44.2
	$P_{target}(kW)$	59.1	57.2	58.6	56.5	43.0	40.1

Table 9.6: The power (P_{target}), average energy (E_{ave}^γ) and polarization (P_γ) of the photon beam at target plane for ideal and realistic undulators with different photon collimator radii (3.0 mm up to 1.0 mm) for three different ILC energy options; ILC-250 with $K = 0.85$, ILC-350 with $K = 0.75$ and ILC-500 with $K = 0.45$.

Photon		Centre-of-mass energy (GeV)					
collimator		250		350		500	
radius (mm)	Parameters	<i>Ideal</i>	<i>Real</i>	<i>Ideal</i>	<i>Real</i>	<i>Ideal</i>	<i>Real</i>
3.0	$E_{ave}(MeV)$	10.0	9.6	17.1	16.9	30.7	28.6
	$P_\gamma(\%)$	51.3	52.6	43.0	42.0	46.4	44.9
	$P_{target}(kW)$	54.7	50.7	57.4	54.3	42.7	39.8
2.0	$E_{ave}(MeV)$	10.7	9.9	19.3	18.5	34.0	31.8
	$P_\gamma(\%)$	76.1	62.1	55.0	52.0	51.3	48.6
	$P_{target}(kW)$	41.4	33.0	52.0	49.4	41.3	38.4
1.8	$E_{ave}(MeV)$	10.6	10.0	19.8	18.9	35.1	32.8
	$P_\gamma(\%)$	87.8	63.7	60.0	57.0	53.8	50.3
	$P_{target}(kW)$	36.9	28.5	49.5	47.0	40.5	38.2
1.6	$E_{ave}(MeV)$	10.4	10.1	20.2	19.2	36.4	34.4
	$P_\gamma(\%)$	92.4	65.0	67.0	61.0	57.3	52.0
	$P_{target}(kW)$	31.6	23.9	46.1	44.3	39.4	37.1
1.4	$E_{ave}(MeV)$	10.1	10.2	20.6	19.4	37.9	35.7
	$P_\gamma(\%)$	95.8	65.7	75.0	66.0	62.4	56.0
	$P_{target}(kW)$	25.8	19.3	41.6	40.0	37.9	35.6
1.2	$E_{ave}(MeV)$	9.8	10.4	20.5	19.6	39.4	37.2
	$P_\gamma(\%)$	97.9	66.6	84.0	70.0	69.4	61.3
	$P_{target}(kW)$	19.8	14.9	35.6	34.5	35.6	33.4
1.0	$E_{ave}(MeV)$	9.3	10.6	20.3	19.8	41.1	38.8
	$P_\gamma(\%)$	97.9	66.9	91.0	73.0	78.1	68.7
	$P_{target}(kW)$	14.0	10.8	28.3	26.9	32.1	30.2

9.6 Polarization Upgrade of ILC-500

All ILC energy options with nominal parameters of the helical undulator-based positron source and without photon collimators generate a positron yield of 1.5 per electron with a polarization of 30 %. Some previous studies on the polarization upgrade for the ILC have been conducted such as in [68, 69].

As discussed above, a photon collimator can be used for upgrading the polarization. Here, the power and the polarization of the photon beam at the target plane of the ILC-500 with different photon beam radii are calculated. The used parameters are shown in tables 2.1 and 6.1. The active undulator length is 147 m and the distance between the center of the undulator to the target plane is 461 m. Figure 9.10 shows the ideal spectrum and polarization of the photon beam produced by passing an electron beam with an energy of 253 GeV, taking into account the loss beam energy, through an ideal helical undulator with K value of 0.45. The considered photon beam radius is 2.0 mm.

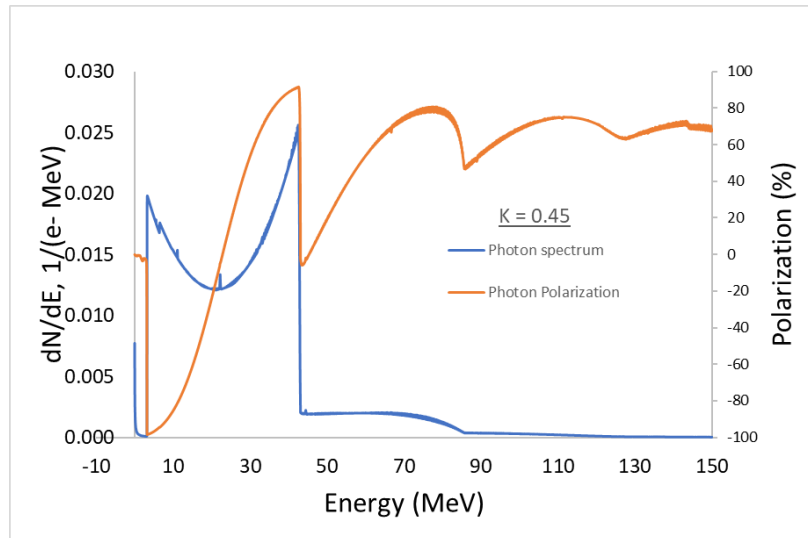


Figure 9.10: Photon beam spectrum and polarization produced by 253 GeV electron beam with K value of 0.45. The blue line represents the photon spectrum and the orange line represents the photon beam polarization. The considered photon spot radius in this plot is 2.0 mm.

The average energy, polarization and power of the photon beam at the target plane considering the photon beam radius of 2.0 mm and the K value of 0.42, are 34.0 MeV, 51.3 % and 41.3 kW respectively. Cutting the outer part of the photon beam by considering a smaller photon beam radius will increase the polarization of the photon beam, but this is at the expense of the photon number (power). If the considered photon beam radius is reduced to 1.0 mm, the average energy and polarization of the photon beam at the target plane increase to 41.1 MeV and 78.0 %, respectively. In contrast, the power of the photon beam decreases to 32.1 kW. To compensate the decrease in

photon number, a higher K value is used. Figure 9.11 shows the ideal spectrum and polarization of the photon beam produced by passing an electron beam with an energy of 253 GeV, taking into account the loss beam energy, through an ideal helical undulator with K value of 0.92. The considered photon beam radius is 2.0 mm.

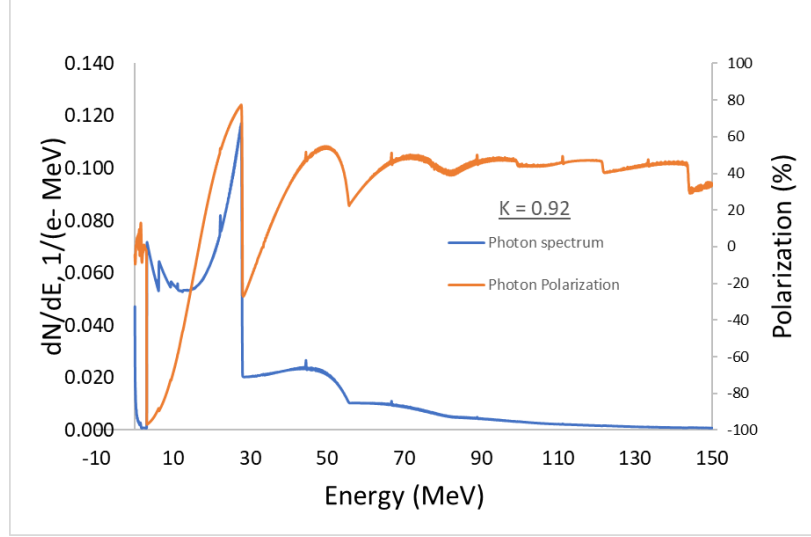


Figure 9.11: Photon beam spectrum and polarization produced by 253 GeV electron beam with K value of 0.92. The blue line represents the photon spectrum and the orange line represents the photon beam polarization. The considered photon spot radius in this plot is 2.0 mm.

The power and polarization of the photon beam at the target plane of the ILC-500 with different photon beam radii and K values are calculated in order to investigate its influence on the photon beam power and polarization. Table 9.7 summarizes the results of the study.

Table 9.7: Energy cutoff of the first harmonic (E_{1st}), average energy (E_{ave}), power (P_{target}) and average polarization (P_γ) of the photon beam at the target plane produced by passing a 253 GeV electron beam through the ILC-500 147 m ideal undulator length with different K values and different considered photon spot radii.

Final Beam Energy (GeV)	250											
Act. Und. Length (m)	147					147						
K Value	0.45					0.92						
E_{1st} (MeV)	43.3					28.2						
Beam Radius (mm)	2.0	1.6	1.0	0.7	2.0	1.6	1.0	0.7	2.0	1.6	1.0	0.7
E_{ave} (MeV)	34.0	36.4	41.1	43.1	38.9	41.2	41.0	37.0	34.0	36.4	41.1	43.1
P_γ (%)	51.3	57.3	78.0	91.4	44.6	55.6	86.0	96.2	51.3	57.3	78.0	91.4
P_{target} (kW)	41.3	39.4	32.1	23.8	167.0	152.0	95.3	51.6	41.3	39.4	32.1	23.8

Results show that the power of the photon beam of the ILC-500 with the photon beam radius of 1.0 mm and K value of 0.45 could not produce the required positron beam. Therefore, in order to

compensate the decrease in the photon number, a K value of 0.92 is proposed. In this case, the photon beam of the ILC-500 with the photon beam radius of 1.0 mm and K value of 0.92 could produce the required positron beam with a polarization of $\approx 50\%$ assuming a flux concentrator (FC) as an OMD as studied in [67]. However, this reference assumes an ideal undulator. For a realistic undulator as considered in this thesis the photon beam polarization is lower, and the collimation of the photon beam will be less efficient, especially for higher K values. Based on the results in this thesis it is expected that the polarization of the photon beam generated in a realistic undulator decreases by $\approx 10\%$ compared with that from an ideal undulator. This propagates to the polarization of the positron beam. Since a high positron beam polarization is desired for ILC-350 and ILC-500, the K value, K value fluctuation and the length of a realistic undulator should be optimized for the final polarization upgrade. The positron yield depends strongly on the performance of the OMD which is currently under discussion and development. A robust and comprehensive study should start with the recommended OMD design. A disadvantage of the ILC-500 with $K = 0.92$ is the high power that gets removed by the photon collimator. It means that, although the heat load in case of a high K value distributes over a larger volume, there is a huge thermal load that will deposit at the material of the collimator, which leads to a high PEDD at the photon collimator as studied in [67]. More detail about the polarization upgrade can be found in [67, 68, 69].

Chapter 10

Synchrotron Radiation Power

Incident on the Undulator Walls of the ILC GigaZ Option

The ILC-TDR in 2012 concentrated on centre-of-mass energies between 250 and 500 GeV (up to 1 TeV). Since the ILC positron beam is polarized, operating the ILC at lower energies, such as the GigaZ option (91.2 GeV) and W-pair threshold (160 GeV), have always been discussed as important options for the ILC operation in the earlier stages of designing the ILC. The current status of operating the ILC at these low energies can be found in [12, 70]. This chapter aims to study the power incident due to the synchrotron radiation on the undulator walls of the ILC GigaZ option.

10.1 Incident Power at Undulator Walls of the GigaZ Option

The aim of the ILC GigaZ option is to collide a polarized positron beam with a polarized electron beam. As discussed in chapter 4, to produce a positron beam with a polarization of $\approx 30\%$, a very intense electron beam should be sent through a very long helical undulator. Since the energy of the electron beam at the GigaZ option is 45.6 GeV, an additional electron beam with an energy of, at least, 125 GeV is needed to produce the required photon beam with the required energy that can produce the required e^+ beam [12]. It means that in the GigaZ option, two electron beams are needed; one serves to produce positrons, and another is for the collision experiment with a $3.7 + 3.7$ Hz scheme. The $3.7 + 3.7$ Hz scheme means that the electron linac is operated at 7.4 Hz: 3.7 Hz to

accelerate the electron beam to 125 GeV, which will be used to produce an e^+ beam, and another 3.7 Hz to accelerate the electron beam to 45.6 GeV for the collision experiment.

One bypass will be sufficient if two electron beams pass through the helical undulator, which is possible [12]. For producing positrons at the GigaZ option, the parameters of the used beam are identical to the parameters of the ILC-250 beam, see table 6.1, except for the repetition rate, which is 3.7 Hz. The proposed parameters of the RF system for both beams for operation at the GigaZ option were discussed in more detail in [12]. Table 10.1 summarizes these parameters.

Table 10.1: The proposed parameters of the RF system for alternating operation of 125 GeV and 45.6 GeV for the GigaZ option [12] and the parameters of the ILC-250.

Parameters	Unit	ILC-250	ILC GigaZ option	
			e^+ production beam	collision beam
Final beam energy	GeV	125	125	45.6
Repetition rate	Hz	5	3.7	3.7

Since the opening angle of the photon beam produced by a helical undulator increases when the electron beam decreases, more photons will deposit at the undulator wall, but of course, with lower average energy compared with that at the ILC-250. Therefore, the deposited power at the undulator wall due to the photon beam produced by both electron beams should be calculated.

Using parameters in tables 6.1 and 10.1, the deposited power due to the photon beam at undulator walls is simulated and shown in figure 10.1. The synchrotron radiation power incident by the first module (1.75 m long) is plotted separately to show the worst-case scenarios of the deposited power by one single undulator module at the undulator wall. Due to the big opening angle of photons that is produced by the collision beam, these photons deposit a higher power than what photons produced by the beam of the e^+ production in the first half of the undulator line. While in the second half, photons produced by the beam of the e^+ production deposit higher power than what photons produced by the collision beam deposit. The maximum power incident per meter is always at the last meter of the undulator line. Since two beams pass through the undulator, the maximum deposited power from the first undulator module (1.75 m long) is 0.89 W/m and 0.17 W/m by photons produced by the e^+ production beam and the collision experiment beam, respectively. Therefore, the total is 1.06 W/m by both beams by the first module. It is $\approx 12\%$ lower than that deposited by the first module (1.75 m long) of the ILC-250, which is 1.2 W/m.

The peak of the deposited power due to the full active undulator length (231 m) for the ILC GigaZ option is ≈ 3 W/m by photons produced by the collision beam and 18.5 W/m by photons produced by both beams at the last meter of the undulator line compared with 21 W/m for the ILC-250 with the same active length. While the maximum allowable heat load is 1 W/m. Therefore, the proposed mask system for the undulator protection for the ILC discussed in section 8.3 can also

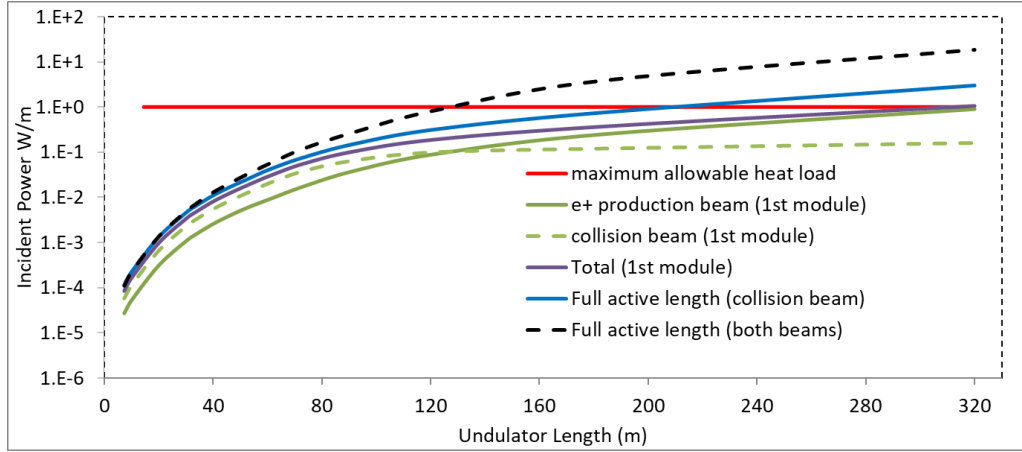


Figure 10.1: Synchrotron radiation power incident per meter on the undulator walls of the GigaZ Option along the total undulator length (320 m). The solid green (dashed green) line represents the incident power by the first undulator module due to the e^+ production (the collision) beam. The solid purple line represents the total deposited power by two beams produced by the first module (1.75 m long). The solid blue line represents the total deposited power by the collision beam passing the full active undulator length (231 m long). The dashed black line represents the total incident power at the undulator walls by both beams passing the full active undulator length (231 m long) of the ILC GigaZ option. The solid red line represents the maximum allowable incident power into the undulator wall.

keep the deposited power in the ILC GigaZ stage with these particular beam parameters below the acceptable level. For comparison, the incident power at the undulator wall of the ILC GigaZ option and ILC-250 is shown in figure 10.2. As discussed in chapter 9, since the beam of the ILC-250 will be used to create the photon beam to produce the e^+ beam of the GigaZ option, the produced positron beam of the GigaZ option will have a polarization of about 30 %.

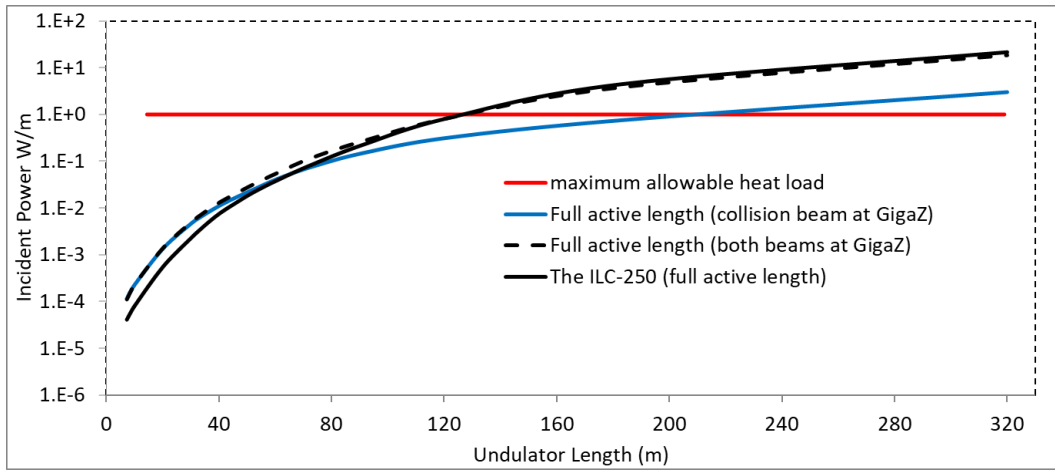


Figure 10.2: Synchrotron radiation power incident per meter on the undulator walls of the GigaZ option and of the ILC-250 along the total undulator length (320 m). The solid black line represents the total incident power at the undulator walls by the full active undulator length (231 m long) of the ILC-250. Other lines have the same meaning as in figure 10.1. Used parameters are shown in table 6.1 and 10.1 for the ILC-250 and GigaZ option, respectively.

Chapter 11

Summary

This thesis has focused on some issues related to the ILC helical-undulator-based positron source. This source is chosen as the baseline design for the positron production in the future ILC project. The ILC requires a long helical undulator (up to 231 m active length) to produce a high-intensity photon beam that is needed to produce the required positron number at the IP of the ILC.

Since the spectrum of the produced positron beam is based on the spectrum of the photon beam created by the helical undulator, the photon spectrum has been discussed depending on the undulator parameters in chapter 5. The HUSR software, which is used to simulate the photon spectrum produced by a helical undulator, has the ability to calculate the non-ideal spectrum and the polarization of the photon beam produced by a non-ideal helical undulator. The non-ideal (realistic) studies are based on the measured B-fields of the ILC helical undulator prototypes which were designed and tested at Daresbury Laboratory and Rutherford Appleton Laboratory in the UK. The calculated photon spectrum of the helical undulator prototypes is used to evaluate the realistic simulation of the HUSR code as shown in chapter 7. Based on these evaluations, the HUSR code is chosen to simulate the realistic spectrum and polarization of the photon beam produced by a realistic helical undulator in this thesis and the considered error sizes on the B-field and period are $\pm 4\%$.

The ILC superconducting helical undulator produces photons with an energy of few MeV to few tens MeV with an opening angle that is proportional to $\frac{1}{\gamma}$. Some of these photons will hit the walls of the long superconducting undulator. Therefore, chapter 8 discusses the problem of the power deposited by the synchrotron radiation at the undulator walls which must not exceed 1 W/m. This problem is studied for an ideal helical undulator as well as for a realistic one taking into account a variation of the undulator strength along the undulator. In case of the nominal ILC-250 option, the maximum deposited power at the ideal (realistic) undulator wall with $K = 0.85$ is ≈ 21 W/m (≈ 23.5 W/m) at the last meter of the helical undulator length. This heat load is too high for the

vacuum. Therefore, 22 photon masks are proposed to be placed along the undulator line to keep the heat load below the acceptable limit. For the current design and parameters, I proposed a design for the photon mask that has an inner radius of 4.4 mm, a length of 30 cm and is placed downstream of each quadruple. The photon masks are designed to stop both primary and secondary particles as much as possible. Perfect photon masks decrease the maximum deposited power, which is at the last meter of the undulator upstream Mask-22, by approximately 2 orders of magnitude to ≈ 0.021 W/m (0.025 W/m) for the ideal (realistic) undulators.

In the case of realistic masks, secondary particles with enough energy leave the masks and hit the undulator wall. Therefore, the deposited power at the undulator wall due to secondary particles is studied. A possible photon mask geometry with a high photon absorption efficiency was proposed in this thesis with three various material candidates, including copper, iron, and tungsten. The deposited power at the masks produced by both ideal and realistic undulators is simulated to determine the secondary particles leaving the masks, the Peak Energy Deposition Density (PEDD), the instantaneous temperature rise, and stress in these masks using the different material candidates.

Regarding the deposited power at the undulator walls, the studies show that all material candidates of the photon masks will keep the deposited power at the undulator wall below the acceptable level in all nominal ILC options. In addition, the results show that iron, copper, and tungsten masks can stop between 96.5% and 99.5 % of the deposited power. In case of the nominal ILC-250 option, the maximum deposited power is at the first meter of the undulator walls downstream Mask-21 and reaches 0.31 W/m for the iron mask, 0.22 W/m for the copper mask, and 0.034 W/m for the tungsten mask compared with 0.021 W/m which assumes the perfect mask characteristics. In the case of the ILC luminosity upgrade, which means the double luminosity, these values are doubled, and the proposed masks will also keep the maximum deposited power at the undulator wall below the limit for all ILC luminosity upgrade options.

The PEDD, temperature increase, and instantaneous maximum stress were studied in order to check whether the mask material has overloaded hot spots for the cyclic load. The results proved that the masks are safe for all three considered materials, and the copper is the best material candidate for the current parameters of the ILC positron source. According to the radiation length, an appropriate option is to use a tungsten mask since its length can be shorter, which saves space when implementing the masks into the undulator line.

The average energy, power, and polarization of the photon beam at the target plane of all ILC energy options before and after placing photon masks were studied for both ideal and realistic undulator cases in chapter 9. Results from the study showed that, in the ideal (realistic) case of the nominal ILC-250 and before placing the masks, the average energy, power, and polarization of the photon beam at the target plane are 7.6 MeV (7.3 MeV), 62.5 kW (61.0 kW), and 36 % (34%),

respectively. After placing photon masks, the power of the photon beam decreases to 60.2 kW (59.0 kW) in the case of ideal (realistic) undulators. In contrast, these masks will increase the average energy and polarization of the photon beam to 8.0 MeV (7.7 MeV) and 37.3 % (35.7 %), respectively, in the case of ideal (realistic) undulators. In other words, the proposed photon masks, in general, would decrease the photon beam power at the target by $\approx 6\%$ and slightly increase the average energy and polarization of the photon beam at the target by $\approx 5\%$ in case of both ideal and realistic undulators.

The photon beam parameters that allow a high photon beam polarization at the target plane of all ILC energy options were studied in chapter 9. Results showed that decreasing the photon beam size at the target plane will increase the photon beam polarization and decrease the photon beam power, leading to a decrease in the produced positron number. A high K value with a small photon beam size can produce a positron beam with high polarization. Therefore, the power and polarization of the photon beam at the target plane of the ILC-500 were discussed using a high K value and considering different beam sizes. Result studies showed that increasing K value from 0.45 to 0.92 and collimating the photon beam radius to 1 mm creates the required photon beam intensity and increases the photon beam polarization from 78.0 % to 86.0 %, will produce the required positron beam with the polarization of about 50 % in the ideal case as shown in [67]. Since in the realistic case the photon beam polarization will be lower, the undulator parameters, especially the K value, as well as that of the photon collimator should be re-optimized taking into account a realistic undulator as well as the updated OMD performance.

In the case of the GigaZ option, the energy of the electron beam is about 46.5 GeV which is too low to generate the required photon beam for the positron production. Therefore, an additional electron beam with an energy of, at least, 125 GeV passing through the helical undulator with an active length of 231 m and K value of 0.85 is needed to produce the required positron beam with $\approx 30\%$ polarization. Using the current GigaZ parameters the study showed that both beams can pass the undulator. Chapter 10 shows that the maximum deposited power at the undulator wall of the ILC GigaZ option due to the photons produced by both electron beams is slightly below that for the nominal case of ILC-250. Regarding the the power incident at the undulator wall of the ILC GigaZ option, it is not necessary to use a bypass for the 46.5 GeV electron beam.

Appendix A

Electron-Positron Collider

A.1 Positron Production

In this section the methods of the positron production as well as the polarization of the positron beam are briefly discussed.

A.1.1 Electromagnetic Cascades

When high-energy electron (or positron) passes through matter, it loss energy by emitting a photon (bremsstrahlung) as a result of the coulomb interactions with the electric field of atomic nuclei. This photon, which in average has the half energy of the electron (or positron), must have at least 1.02 MeV in order to produce electron-positron pair as a result of the interaction between this photon and the coulomb fields of the nuclei in the matter. The electron and positron will loss energy again by emitting two (one photon form each particle) photons and collision with the atoms of the matter. This sequence continues with the original electron (or positron) energy eventually manifesting itself as many particles.

As long as these particles have enough energy and traveling through the matter, the number of electrons, positrons and photons increases exponentially, while the average energy of these particles decreases. Figure [A.1](#) shows schematically these processes.

Due to the ionization losses, the shower development is limited. So when the average energy of these charged particles hit the critical energy E_c , the electromagnetic shower starts to decay. It means that particles (electrons and positrons) which have energies above the critical energy (E_c) will produce bremsstrahlung radiation, while particles with energy below the critical energy will do ionization losses. It means that when the energy of charged particles become below the critical energy (E_c) no further photons are produced which means no further electron-positron pairs are

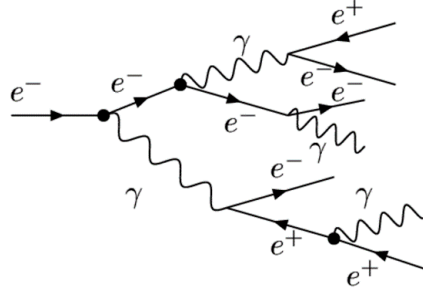


Figure A.1: Electromagnetic shower. A High energy electron creates a photon by bremsstrahlung, which then produces positron and electron by pair production.

produced.

So, the E_c is the energy where:

$$-\frac{dE}{dx}|_{brems} = -\frac{dE}{dx}|_{ion} \quad (\text{A.1})$$

The E_c depends on the type of the atomic number (Z) of the matter. For example E_c is ≈ 8 MeV for tungsten as shown in figure A.2. The E_c is approximately given by [71]:

$$E_c = \frac{610 \text{ MeV}}{Z + 1.24} \quad (\text{A.2})$$

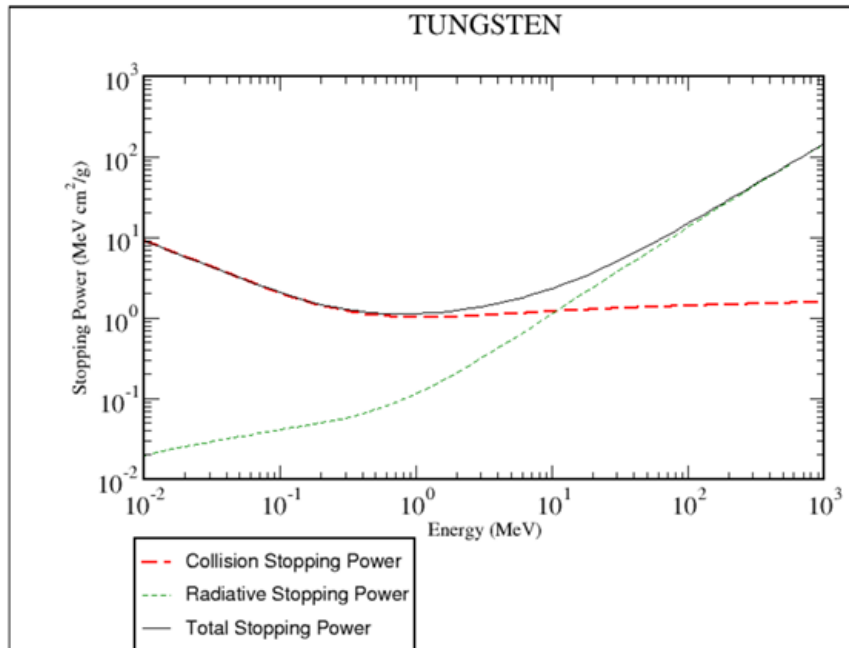


Figure A.2: Mass radiation stopping power for electrons in tungsten. Data were obtained from the NIST [72].

The maximum number of particles N_{max} in the shower occurs when the average energy of electrons and critical energy become equal to each other. N_{max} is when $\frac{E}{E_c} = 1$ and is given by:

$$N_{max} = N_{e^+} + N_{e^-} + N_\gamma \quad (\text{A.3})$$

Where N_{e^+} , N_{e^-} and N_γ are the number of positrons, electrons and photons, respectively. E is the average energy of the electron (or positron).

Figure A.3 shows the Feynman graphs for pair production and bremsstrahlung. It is clear that they are basically inverse processes. They can be characterized by the radiation length (X_0).

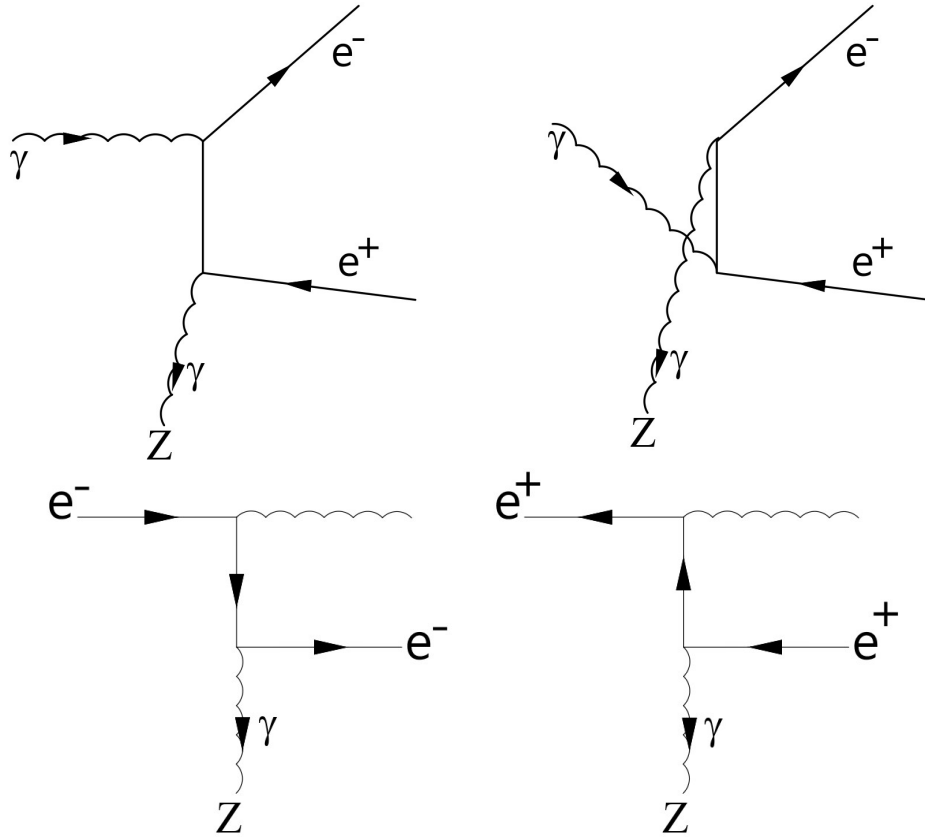


Figure A.3: Feynman graphs for pair production (upper) and bremsstrahlung (bottom).

The X_0 defines as:

- The length of a material is where a photon produces on the average an electron-positron pair.
- The radiation length of a material where the energy of electron (or positron) loss on the average all but a fraction of $\frac{1}{e}$ of its energy.

The X_0 depends on the material properties such as the atomic weight (A), the atomic charge (Z) and the density of material (ρ). Tables in [71] show the radiation length for various materials. The radiation length can be approximated by:

$$X_0^{-1}[cm^{-1}] = \frac{4N_A\alpha\rho r_e^2}{A}Z(Z+1)\ln\left(\frac{183}{Z^{-\frac{1}{3}}}\right) \quad (\text{A.4})$$

Here, N_A is Avogadro's number, A is atomic weight, Z is the atomic charge, r_e is the classical electron radius ($2.82 \times 10^{-15}m$), $\alpha = \frac{1}{137}$, ρ is the density of material.

The required positron yield in the ILC is $\approx 2 \times 10^{14}$ positrons per second. There are two relevant schemes that can be used to produce the positron beam for the ILC. One is to use an initial high energy electron beam which interact with a thick material to produce photons (bremsstrahlung radiation) which then will interact with the atom of the material to produce electron-positron pairs. This approach is known as Electron Driven (e-Driven) source. The second scheme is done in two steps. Firstly, photons are produced outside the conventional target and then letting these photons interacting with a thin target to produce electron-positron pairs. This can be done by using undulator-based positron source. These two approaches are discussed with more detail in chapter 4. In the following, the basic of these two approaches is discussed.

A.1.1.1 Photon Interactions with Matter

There are three main processes in which photons interact with matter, including the photoelectric effect, Compton scattering and pair production. In addition, there are another three processes; namely, coherent scattering (Rayleigh scattering), photonuclear absorption and pair production through the electron field which can be neglected for our purpose.

- **Photoelectric Absorption:** It is the dominant process at low energy up to the MeV. During this process, the incident photon which must have energy higher than the electronic binding energy is completely absorbed by the absorbed and an electron is released with a kinetic energy [73].
- **Compton Scattering:** The Compton scattering is the dominant process also at low energies up to few hundred keV. During this process, the incoming photon with energy of E_γ will scatter on an electron in the atomic shell with energy of E_γ and the electron leaves its shell with kinetic energy E_e^{kn} [73].
- **Pair Production:** This process is dominant at high energies starting from, at least, $1.022 \text{ MeV} = 2m_e c^2$. During this process, the incoming photon with energy of E_γ will be completely absorbed by the medium and electron-positron pairs is produced [73].

Figure A.4 shows the total cross section of photon as a function of the energy in Titanium for all three main interaction processes.

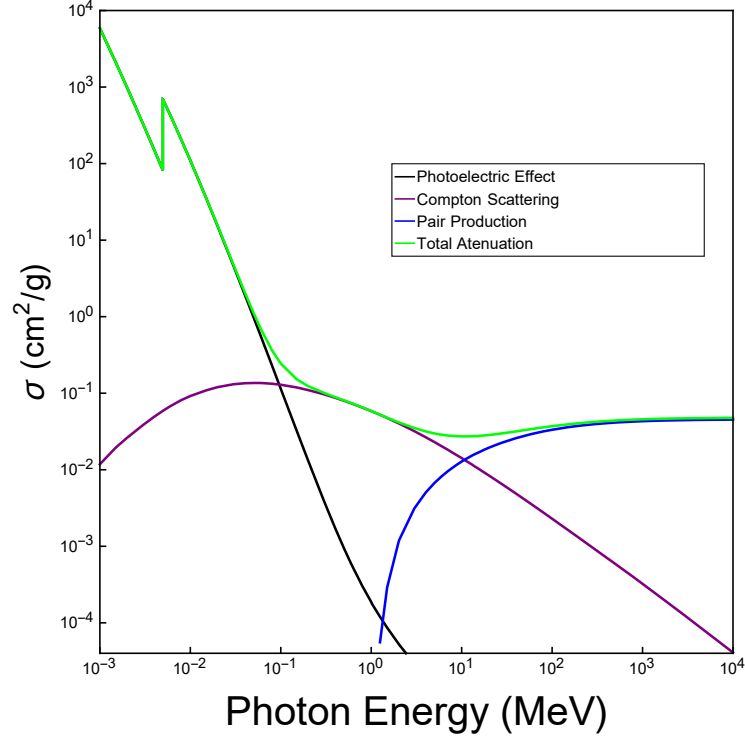


Figure A.4: The cross section of photon as a function of the photon energy in titanium. Data were obtained from XCOM [22] and plotted by Mathematica.

In order to produce pair production, the incoming photon must have energy E_γ , at least, ≥ 1.022 MeV which is the rest energy of electron and positron ($2m_e c^2$). The kinetic energy of the electron (T^-) and the kinetic energy of the positron (T^+) is given by [73]:

$$E_\gamma = 2m_e c^2 + T^- + T^+ \quad (\text{A.5})$$

It is not necessary that electron and positron have the same kinetic energy, but the average kinetic energy (\bar{T}) for each particle can be given by:

$$\bar{T} = \frac{E_\gamma - 1.022 \text{ MeV}}{2} \quad (\text{A.6})$$

For higher E_γ , the electron and positron are forward directed. The average angle $\bar{\theta}$ of the electron and positron departure depends on the direction of the incoming photon and is approximately given by:

$$\bar{\theta}(\text{radians}) \approx \frac{m_e c^2}{T} \quad (\text{A.7})$$

For energies between 1.022 MeV up to few ten MeV, the cross section of the pair production (σ_{pair}) increases with the energy, while at high energies, the (σ_{pair}) is constant as shown in figure A.4. It means that as long as photons with high energy increase the probability (P) of producing

positrons increases. The probability (P) of a pair production by a photon with high energy passing through a material with a thickness of x is given by:

$$P = 1 - e^{(-xn\sigma_{pair})} \quad (\text{A.8})$$

Where, n is the number of atoms per unit volume $n = \frac{\rho N_A}{A}$,

As shown in figure A.4, the probability of producing pairs increases with the energy of the photons. However, the pair production process is dominant at high energy, the particles from Compton Scattering process, which may only increase the stress on the target, is there. Therefore, the parameters should be optimized in order to produce required positron number with an appropriate energy and in the same time avoiding a high stress on the target. In this case, photons with energy of a few MeV can be used to hit a thin high Z target to produce electron-positron pairs. Optimizing a target with 1 or 0.5 Radiation length.

A.1.1.2 Electron Interactions

The second approach is to use electrons as the initial beam. As mentioned earlier, when a charged particle such as an electron with high energy deviates from its direction due to a collision with a nucleus, a bremsstrahlung radiation (a photon) is emitted. The peak of this emitted radiation is in the same trajectory of the electron. While the low-energy charged particle lose energy by ionization.

Generally, during the process of bremsstrahlung, the emitted photon gets a fraction of the energy of the electron (or positron).

At low energies, ionization losses is the dominating process, while at high energies the bremsstrahlung is the dominating process. Ionization losses decrease logarithmically with energy, while bremsstrahlung increases approximately linear with the energy as shown in figure A.2.

The probability $\frac{\Phi(E, E_\gamma)}{dx dE_\gamma}$ of emitting a photon with an energy of E_γ when an electron with high energy E passes through a material layer of thickness dx is given by:

$$\frac{\Phi(E, E_\gamma)}{dx dE_\gamma} = \frac{1}{X_0} \frac{1}{E_\gamma} F(E, E_\gamma) \quad (\text{A.9})$$

Where,

$$F(E, E_\gamma) \approx 1 + \left(\frac{E - E_\gamma}{E}\right)^2 + \frac{2}{3} \left(\frac{E - E_\gamma}{E}\right) \quad (\text{A.10})$$

During bremsstrahlung process, the average energy loss in a thickness of material dx for an

electron (or positron) is given by:

$$-\frac{dE}{dx} = \int_{E_\gamma=0}^{E_\gamma=E} \frac{\Phi(E, E_\gamma)}{dx dE_\gamma} E_\gamma dE_\gamma \quad (\text{A.11})$$

Which is given by:

$$-\frac{dE}{dx} = \frac{E}{X_0} \quad (\text{A.12})$$

The mass stopping power (the rate of bremsstrahlung production) S can be calculated by dividing equation A.12 by the density ρ of the absorber. Here the unit of the mass stopping power (energy loss) is $(\text{MeVcm}^2/\text{g})$. The S is given by [74]:

$$S(\text{MeVcm}^2/\text{g}) = N_a \sigma_{rad} E_i \quad (\text{A.13})$$

Where, $N_a = \frac{N_A}{A}$ is the atomic density, σ_{rad} is the cross section for the emission of the bremsstrahlung and $E_i = (E_K)_{int} + m_e c^2$ which is the initial total energy of the charged particle (electron). $(E_K)_{int}$ represents the initial kinetic energy of electron.

$$S(\text{MeVcm}^2/\text{g}) = N_a \sigma_{rad} E_i \quad (\text{A.14})$$

In 1930s, the cross section for the emission of the bremsstrahlung (σ_{rad}) has been shown by Hans Bethe and Walter Heitler and is given by [74]:

$$\sigma_{rad} \propto r_e^2 \alpha Z^2 (\text{cm}^2/\text{nucleus}) \quad (\text{A.15})$$

The symbols in equation A.15 have the same meaning as in equation A.4. The σ_{rad} varies with $(E_K)_{int}$ and is given by [74]:

$$\sigma_{rad} = \begin{cases} \frac{16}{3} \alpha r_e^2 Z^2, & \text{for } (E_K)_{int} \ll m_e c^2 \\ 8Z^2 r_e^2 \left[\ln\left(\frac{E_i}{m_e c^2}\right) - \frac{1}{6} \right], & \text{for } m_e c^2 \leq (E_K)_{int} \leq \frac{m_e c^2}{\alpha Z^{\frac{1}{3}}} \\ 4Z^2 r_e^2 \alpha \left[\ln\left(\frac{183}{Z^{\frac{1}{3}}} + \frac{1}{18}\right) \right], & \text{for } (E_K)_{int} \gg \frac{m_e c^2}{\alpha Z^{\frac{1}{3}}} \end{cases}$$

Figure A.2 shows the S for electron in tungsten.

Since the X_0 is proportional to $(Z^2 \cdot \rho)^{-1}$, it means that a high Z material has a small X_0 . Therefore, the ionization loss per X_0 becomes small (large) for a high (low) Z material.

The collisions between charged particles and the nuclei cause changes on the direction of the charged particles. The change in the angle for a charged particle traveling through a material with

Z atomic number and a thickness of S is given by the root mean square (r.m.s) as follow:

$$\sqrt{\Theta^2} = \frac{Z}{Pc\beta} 20(\text{MeV}) \sqrt{\frac{S}{X_0}} \quad (\text{A.16})$$

Here Θ is the scattering angle (in radians) relative to the incoming particle, P is momentum of the incoming particle, c is the speed of light and $\beta = \frac{v}{c}$, where v is the particle speed.

- **Producing Positron by Bremsstrahlung Radiation in the ILC.**

So, as discussed earlier, when an electron with few GeV energy passes through the first radiation length of a medium, a photon with energy of, in average, half of the initial electron energy is emitted. In the second radiation length, this electron emits another photon and the photon emitted in the first radiation length is completely absorbed, and electron-positron pairs is produced. The pair production is discussed with more detail in section [A.1.1.1](#).

In general, when the initial electron energy (E_{in}) is high, then:

- After the first radiation length, there will be two particles, one is electron and one is photon, with an average energy of $\frac{E_{in}}{2}$.
- After the second radiation length, there will be four particles, two electrons and one photon and one positron, with an average energy of $\frac{E_{in}}{4}$.
- After the k radiation length, the total particle number $N_{total} = 2^k$, each particle has energy of, in average, $\frac{E_{in}}{2^k}$.

Since the total number of particles is given by 2^k , the total number of positrons N_{e^+} is given by:

$$N_{e^+} = \frac{N_{total}}{3} = \frac{2^k}{3} \quad (\text{A.17})$$

Figure [A.5](#) simplifies this process.

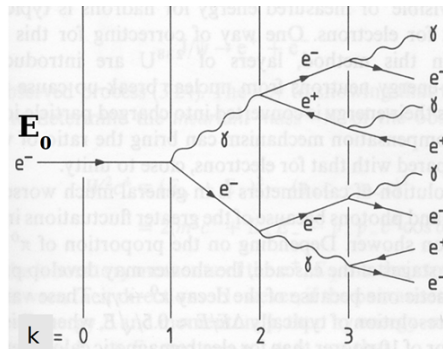


Figure A.5: Schematic of the electron shower passing through 3 radiation length of a material.

The required positron yield at the damping ring in the ILC is 1.5 (e^-/e^+). Therefore, in order to get the required positron yield by using e-Driven source (which is the alternative positron source in the ILC. For more details see section 4.2), the atomic number (Z) of the target material should be high and the thickness of the material must be few radiation lengths. In the same time, the incoming electron should have enough energy, so that the produced positrons can receive enough energy in order to leave the target. In addition, the positron should have an angle distribution as small as possible in order to be captured by the matching device which is placed directly after the target. Therefore, the initial electron energy should have few GeV.

The most serious problem in the e-Driven source is that the deposited energy of the shower causes stress inside the target. This problem can be avoided by producing photons with high energy outside the target and that can be done by the undulator.

A.2 Positron Polarization

In the general law of physics, the polarization is conserved. Therefore, the positron beam produced by a polarized beam whether an electron or photon beam is polarized. It means that if the initial beam that is used to produce the positron is polarized, the positron produced by that beam inherit its polarization. The polarization transfer can be calculated by using the transformation matrix introduced by McMaster in (his paper [75]).

A.2.1 Polarization

Polarization is one of the important property of electromagnetic waves. The polarization of a transverse wave depicts the oscillations of their transverse electric (magnetic) field. The total electric field of a plane wave propagating in z-direction is given as follow:

$$\vec{E}(\vec{r}, t) = E_{ox}e^{i(kz-\omega t)} + E_{oy}e^{i(kz-\omega t)} \quad (\text{A.18})$$

Equation A.18 can be rewritten as a column vector:

$$\vec{E}(\vec{r}, t) = \begin{pmatrix} E_{ox} \\ E_{oy} \end{pmatrix} e^{i(kz-\omega t)} \quad (\text{A.19})$$

A.2.2 Parameterization of Polarization

A.2.2.1 The Jones Vector

There are three types of polarization; the linear, the circular, and the elliptical polarization.

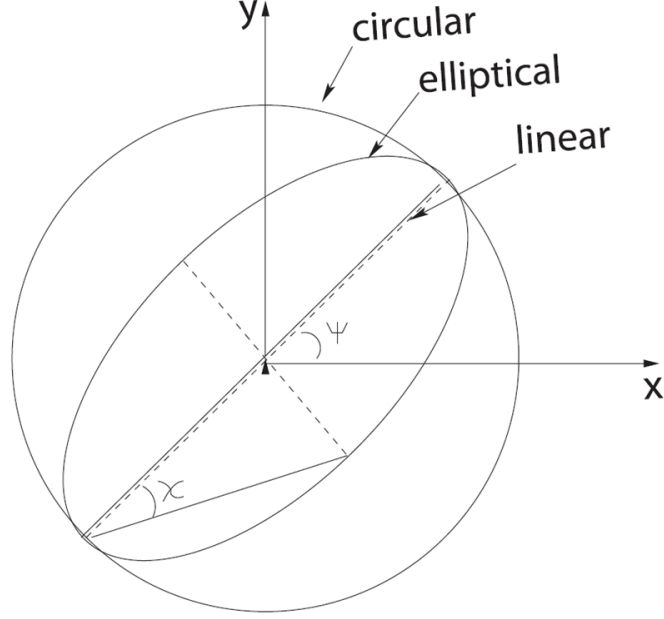


Figure A.6: The electric field vector in the x-y plan.

A.2.3 Stokes Parameters from Jones Vector

If an orthogonal right-handed coordinate system is introduced in a wave that is traveling in the positive z-direction, Stokes parameters can be defined as follow:

The I_0 represents the total intensity of the wave. The $\zeta_1 = \frac{I_x - I_y}{I_0}$ represents the linear polarization degree with respect to the axis of x and y . The $\zeta_2 = \frac{I_{45} - I_{135}}{I_0}$ represents the linear polarization degree with respect to the axes oriented at 45° to the right of the previous axis of x - and y -. The $\zeta_3 = \frac{I_l - I_r}{I_0}$ represents the circular polarization rate. The I_l and I_r represent the left and right intensities of the circular polarization, respectively.

With regards to the Jones Vector, the stokes parameters can be introduced by using the matrix unit (σ_0) and the Pauli matrices as follow:

$$I_0 = a_1^* a_1 + a_2^* a_2 = \vec{a}^\dagger \sigma_0 \vec{a} \quad (\text{A.20})$$

$$\zeta_1 = (a_1^* a_1 - a_2^* a_2) / I_0 = (\vec{a}^\dagger \sigma_1 \vec{a}) / I_0 \quad (\text{A.21})$$

$$\zeta_2 = (a_1^* a_2 + a_2^* a_1) / I_0 = (\vec{a}^\dagger \sigma_2 \vec{a}) / I_0 \quad (\text{A.22})$$

$$\zeta_3 = -i(a_1^* a_2 - a_2^* a_1) / I_0 = (\vec{a}^\dagger \sigma_3 \vec{a}) / I_0 \quad (\text{A.23})$$

Where:

$$\sigma_0 = \begin{pmatrix} 1 & 0 \\ 0 & 1 \end{pmatrix} \quad \sigma_1 = \begin{pmatrix} 1 & 0 \\ 0 & -1 \end{pmatrix} \quad \sigma_2 = \begin{pmatrix} 0 & 1 \\ 1 & 0 \end{pmatrix} \quad \sigma_3 = \begin{pmatrix} 0 & -i \\ i & 0 \end{pmatrix}$$

In the more compact form of a single particle, the Stokes parameters can be written as four vector that are known as a Stokes vector.

$$\begin{pmatrix} I_0 \\ \zeta_1 \\ \tilde{\zeta} \\ \zeta_3 \end{pmatrix} = \begin{pmatrix} I_0 \\ \zeta_1 \\ \zeta_2 \\ \zeta_3 \end{pmatrix}, \quad (\text{A.24})$$

For a single particle with a polarization of 100 %, it takes the following condition:

$$\zeta_1^2 + \zeta_2^2 + \zeta_3^2 = 1 \quad (\text{A.25})$$

In the Stokes formalism, the polarization state of any electromagnetic wave, the polarization of a single electron (or positron), as well as the linear and circular polarization of a single photon, can be characterized by three parameters (real numbers). In order to calculate the average polarization rate, the Stokes vector can be extended from the description of the polarization of a single particle to the description of the polarization of a beam. In this case, equation A.25 becomes an inequality.

A.2.4 Transfer Matrix

Assuming a particle undergoes an electromagnetic process, the initial state of the polarization is transformed in a convenient way into a new set of parameters by using the transformation matrices that are introduced by McMaster [75]. The polarization transfer from the initial state ($\vec{\zeta}$) to one final state particle ($\vec{\zeta}'$) and the differential cross section are shown in a 4×4 interaction matrix (T) characterizing the interaction. Generally, the T depends on the kinematical variables and the polarized cross section, in case of both initial and target particles are polarized. In this context, the general mathematical formulation of the T is given by the following form:

$$T = \begin{pmatrix} S & A_1 & A_2 & A_3 \\ P_1 & M_{11} & M_{21} & M_{31} \\ P_2 & M_{12} & M_{22} & M_{32} \\ P_3 & M_{13} & M_{23} & M_{33} \end{pmatrix}. \quad (\text{A.26})$$

where, S represents the unpolarized differential cross section, A_j represents the differential cross section dependent on the polarization, P_i represents the (de)polarization effects, and M_{ij} represents the polarization transfer to secondaries.

By using the complete matrix, all polarization effects can be considered. In case of an initial

particle that interacts through an electromagnetic process, the final state of the polarization can be got by applying the interaction matrix to the initial state of the polarization. It is given by:

$$\begin{pmatrix} I \\ \vec{\zeta}^{(1)} \end{pmatrix} = T \begin{pmatrix} I_0 \\ \vec{\zeta}^{(1)} \end{pmatrix} \quad (\text{A.27})$$

Where, I_0 and I represent the intensity of the incoming and outgoing beams, respectively. The exponent (1) in Stokes vectors of the initial $\vec{\zeta}^{(1)}$ and final $\vec{\zeta}^{(1)}$ states of particles stands for the primary particle.

In the same way, if secondaries are created in an interaction, a matrix can be defined to describe the polarization transfer to those secondaries. In this case, it is given as follows:

$$\begin{pmatrix} I' \\ \vec{\zeta}^{(2)} \end{pmatrix} = T' \begin{pmatrix} I_0 \\ \vec{\zeta}^{(1)} \end{pmatrix} \quad (\text{A.28})$$

Where, I' represents the intensity of the outgoing secondary beam. The exponent (1) and (2), in Stokes parameters of the incoming ($\vec{\zeta}^{(1)}$) and the secondary ($\vec{\zeta}^{(2)}$) particle polarization state, stand for the primary particle and a produced secondary particle, respectively.

A.3 Bremsstrahlung Radiation and Pair Production

As discussed earlier, bremsstrahlung radiation is created when an electron (or positron) is accelerated or decelerated. While the pair production process is the creation of the electron and positron by a photon. This process happens when the photon with an energy above the threshold which is the total rest mass of both electron and positron interacts with the field of an atomic nucleus.

In the following the polarization transfer in both processes are discussed.

A.3.1 Polarized Bremsstrahlung

A.3.1.1 Polarization Transfer from a Lepton (an Electron or Positron) to a Photon

The basic formulas of polarization transfer from an electron (or positron) to a photon in a bremsstrahlung process, that were calculated by Olsen and Maximon in [23], are described in this section. Both

Coulomb and screening effects were considered in this calculation. In the Stokes formalism, the polarization of an Electron (e^-) (or a positron (e^+)) is transferred to the finale state of a photon through an interaction matrix T_γ^b . In this case, the polarization transfer is given by:

$$\begin{pmatrix} I \\ \vec{\zeta}^{(2)} \end{pmatrix} = T_\gamma^b \begin{pmatrix} I_0 \\ \vec{\zeta}^{(1)} \end{pmatrix} \quad (\text{A.29})$$

and the matrix of the interaction is given by:

$$T_\gamma^b = \begin{pmatrix} 1 & 0 & 0 & 0 \\ D & 0 & 0 & 0 \\ 0 & 0 & 0 & 0 \\ 0 & T & 0 & L \end{pmatrix}, \quad (\text{A.30})$$

$$I = (\epsilon_1^2 + \epsilon_2^2)(3 + 2\Gamma) - 2\epsilon_1\epsilon_2(1 + 4u^2\hat{\zeta}^2\Gamma) \quad (\text{A.31})$$

$$D = \{8\epsilon_1\epsilon_2u^2\hat{\zeta}^2\Gamma\}/I \quad (\text{A.32})$$

$$T = \{-4k\epsilon_2\hat{\zeta}(1 - 2\hat{\zeta})u\Gamma\}/I \quad (\text{A.33})$$

$$L = k\{(\epsilon_1^2 + \epsilon_2^2)(3 + 2\Gamma) - 2\epsilon_2(1 + 4u^2\hat{\zeta}^2\Gamma)\}/I \quad (\text{A.34})$$

where, ϵ_1 and ϵ_2 represent the total energy of the incoming and outcoming lepton e^+ (e^-) in units $m_e c^2$, respectively. The \vec{p} represents the electron (positron) initial momentum in units $m_e c$. The \vec{k} represents the bremsstrahlung photon momentum in units $m_e c$. The \vec{u} shows the component of \vec{p} perpendicular to \vec{k} in units $m_e c$ and $u = |\vec{u}|$. The $k = (\epsilon_1 - \epsilon_2)$ represents the energy of the bremsstrahlung photon in units of $m_e c^2$.

So the photon polarization ($\vec{\zeta}^{(2)}$) is :

$$\vec{\zeta}^{(2)} = \begin{pmatrix} \zeta_1^{(2)} \\ \zeta_2^{(2)} \\ \zeta_3^{(2)} \end{pmatrix} = \begin{pmatrix} D \\ 0 \\ \vec{\zeta}_1^{(1)}L + \vec{\zeta}_2^{(1)}T \end{pmatrix}, \quad (\text{A.35})$$

A.3.2 Pair Production

The pair production process is essentially the inverse process of the bremsstrahlung. In addition, the interaction matrix is given by inverting the rows and columns of the bremsstrahlung matrix and

changing the sign of ϵ_2 as have been described in section [A.3.1.1](#).

A.3.2.1 Polarization Transfer from the Photon to two Leptons (e^- and e^+)

The basic formulas of the polarization transfer from the photon to the positron (and electron) are described in this section. These were calculated by Olsen and Maximon in [\[23\]](#). This calculation shows that the polarization state $\vec{\zeta}^{(1)}$ of a positron (electron) after the pair production is given by:

$$\begin{pmatrix} I \\ \vec{\zeta}^{(1)} \end{pmatrix} = T_I^b \begin{pmatrix} I_0 \\ \vec{\zeta}^{(1)} \end{pmatrix} \quad (\text{A.36})$$

and the interaction matrix is given by:

$$T_I^c = \begin{pmatrix} 1 & D & 0 & 0 \\ 0 & 0 & 0 & T \\ 0 & 0 & 0 & 0 \\ 0 & 0 & 0 & L \end{pmatrix}, \quad (\text{A.37})$$

$$I = (\epsilon_1^2 + \epsilon_2^2)(3 + 2\Gamma) + 2\epsilon_1\epsilon_2(1 + 4u^2\hat{\xi}^2\Gamma) \quad (\text{A.38})$$

$$D = \{-8\epsilon_1\epsilon_2u^2\hat{\xi}^2\Gamma\}/I \quad (\text{A.39})$$

$$T = \{-4k\epsilon_2\hat{\xi}(1 - 2\hat{\xi})u\Gamma\}/I \quad (\text{A.40})$$

$$L = k\{(\epsilon_1^2 + \epsilon_2^2)(3 + 2\Gamma) - 2\epsilon_2(1 + 4u^2\hat{\xi}^2\Gamma)\}/I \quad (\text{A.41})$$

where, the ϵ_1 and ϵ_2 represent the total energy of the first and the second lepton $e^+(e^-)$ in units $m_e c^2$, respectively. The $k = (\epsilon_1 + \epsilon_2)$ represents the energy of the incoming photon in units of $m_e c^2$ and the u represents the initial momentum of the electron (positron) in units $m_e c$. The $\hat{\xi}$ is given by $= 1/(1 + u^2)$

Using equation [A.36](#) and the transfer matrix in equation [A.37](#), the $\vec{\zeta}^{(1)}$ is given by:

$$\vec{\zeta}^{(1)} = \begin{pmatrix} \zeta_1^{(1)} \\ \zeta_2^{(1)} \\ \zeta_3^{(1)} \end{pmatrix} = \begin{pmatrix} \vec{\zeta}_3^{(1)} T \\ 0 \\ \vec{\zeta}_3^{(1)} L \end{pmatrix}, \quad (\text{A.42})$$

A.3.2.2 Transferring the Circular Polarization from the Photon to the Longitudinal Polarization for the two Leptons (e^- and e^+)

If the photon is circular polarized, the electron (and positron) can be created with longitudinally polarization. In this case, the interaction matrix is given by:

$$T_I^c = \begin{pmatrix} 1 & -D & 0 & 0 \\ 0 & 0 & 0 & -L \\ 0 & 0 & 0 & -T \\ 0 & 0 & 0 & 0 \end{pmatrix}, \quad (\text{A.43})$$

$$I = (\epsilon_1^2 + \epsilon_2^2)(3 + 2\Gamma) + 2\epsilon_1\epsilon_2(1 + 4u^2\zeta\Gamma) \quad (\text{A.44})$$

$$D = \{8\epsilon_1\epsilon_2u^2\zeta\Gamma\}/I \quad (\text{A.45})$$

$$L = k\{(\epsilon_1 - \epsilon_2)(3 + 2\Gamma) + 2\epsilon_2(1 + 4u^2\zeta^2\Gamma)\}/I \quad (\text{A.46})$$

$$T = \{4k\epsilon_2\zeta(1 - 2\zeta)\Gamma\}/I \quad (\text{A.47})$$

$$k = (\epsilon_1 + \epsilon_2) \quad (\text{A.48})$$

where, the ϵ_1 and ϵ_2 represent the total energy of the first and second lepton e^+ (e^-) in units $m_e c^2$, respectively. The $k = (\epsilon_1 + \epsilon_2)$ represents the energy of the incoming photon in units of $m_e c^2$ and the u represents the initial momentum of electron (positron) in units $m_e c$. The $\hat{\zeta}$ is given by $= 1/(1 + u^2)$.

Using equation A.36 and the transfer matrix in equation A.43, the $(\vec{\zeta}^{(1)})$ is given by:

$$\vec{\zeta}^{(1)} = \begin{pmatrix} \zeta_1^{(1)} \\ \zeta_2^{(1)} \\ \zeta_3^{(1)} \end{pmatrix} = \begin{pmatrix} -\vec{\zeta}_3^{(1)} L \\ -\vec{\zeta}_3^{(1)} T \\ 0 \end{pmatrix}, \quad (\text{A.49})$$

A.3.2.3 Simulating the Polarization Transfer

There are some simulation tools which were developed in the last three decades take into account polarization effects. One of these interesting tools was developed by K. Flottmann in Electron Gamma Shower (EGS) Code [29]. This code could track the polarization state of particles in the electromagnetic interaction with matter by using the Stokes formalism to describe the polarization state of particles. More detail can be found in [29].

Another possible code is GEANT4. The implementation of polarization in the library in this code was developed by E-166/EUROTEV groups in DESY and the Humboldt University and follows very closely the approach by McMaster [McMaster(1961)]. Figure A.7 represents the energy spectrum and degree of polarization for photons produced by a 1 m helical undulator with strength $K = 1$ and period $\lambda_u = 1$ cm, as well as the corresponding energy and polarization spectra for the created positrons [76].

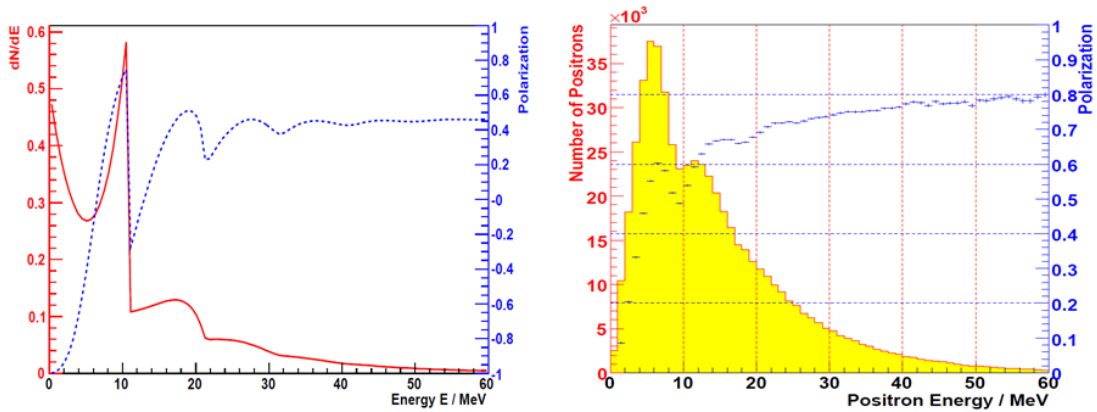


Figure A.7: Left plot: Solid line shows the energy of photon and dashed line represents polarization of photons produced by a helical undulator. Right plot: Energy (histogram) and polarization of positrons which are produced by these photons after the production target [76].

Appendix B

The ILC Photon Beam Power and Polarization

B.1 The Effect of the Photon Collimator on Photon Beam Parameters

The influence of different photon collimator radii on the power, average energy, and polarization of the photon beam in the target plane of all ILC energy options for both ideal and realistic undulator cases is studied as in seen in chapter 9.

As seen in tables 9.5 and 9.6 which summarize the study results, plots in figure B.1, B.2 and B.3 show the spectrum and polarization of the photon beam at the ILC-250 target plane for both ideal and realistic undulator cases using a photon collimator with different radii.

As seen in plots in figures B.1, B.2 and B.3, by decreasing the aperture of the photon collimator, the outer part of the photon beam, which has a low polarization, is removed. The result is that the average polarization of the photon beam increases. This leads to increasing the polarization of the produced positron beam, which can increase the effective luminosity. On the other hand, there is a reduction in the yield of the photon, resulting a decrease on the positron yield as seen the plots of the photon spectrums.

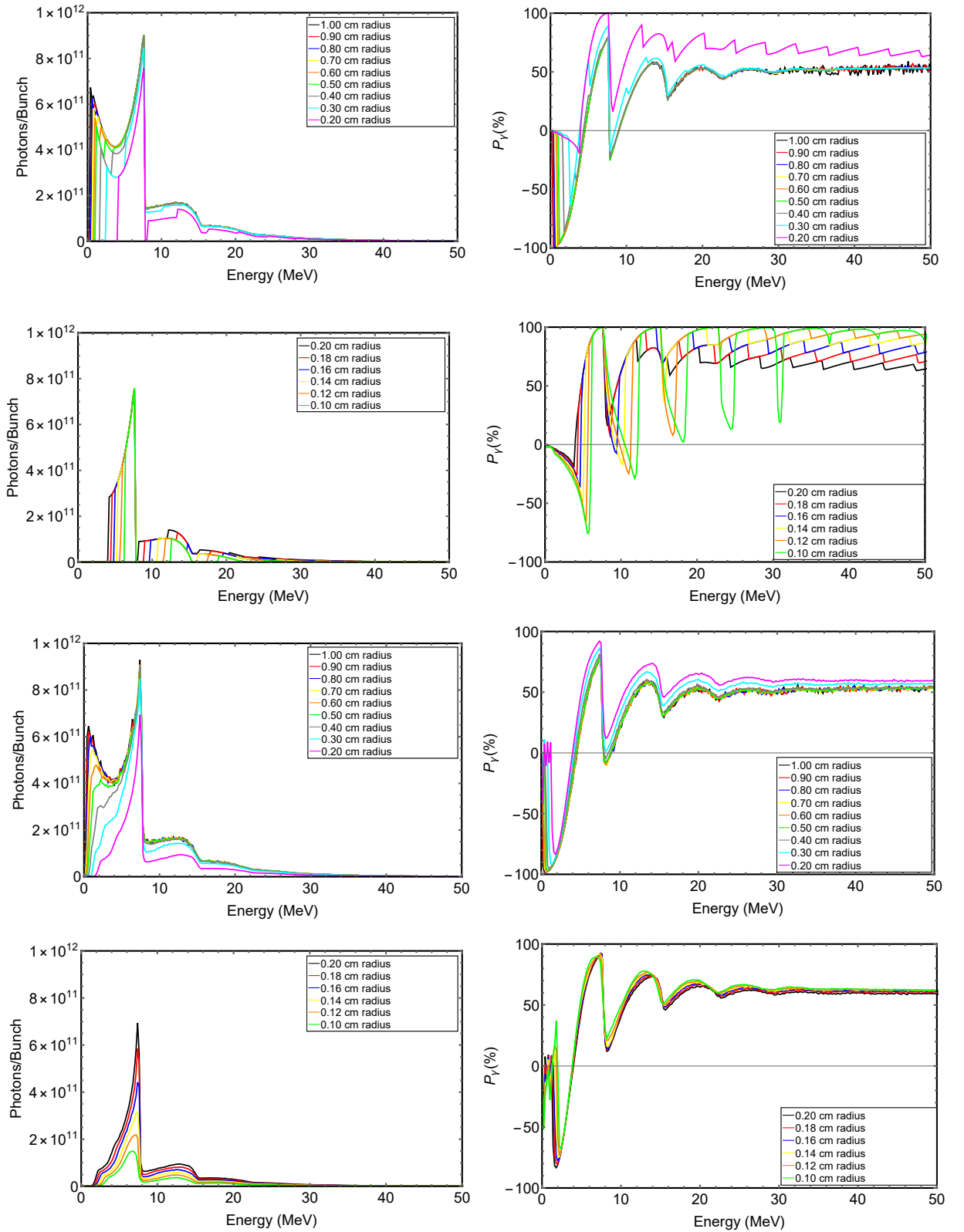


Figure B.1: Ideal (top) and realistic (bottom) spectrum (left) and circular polarization (right) of the photon beam produced by the **ILC-250** undulator with K 0.85 at the target plane with different photon collimator apertures. Each colour represents a different photon collimator aperture.

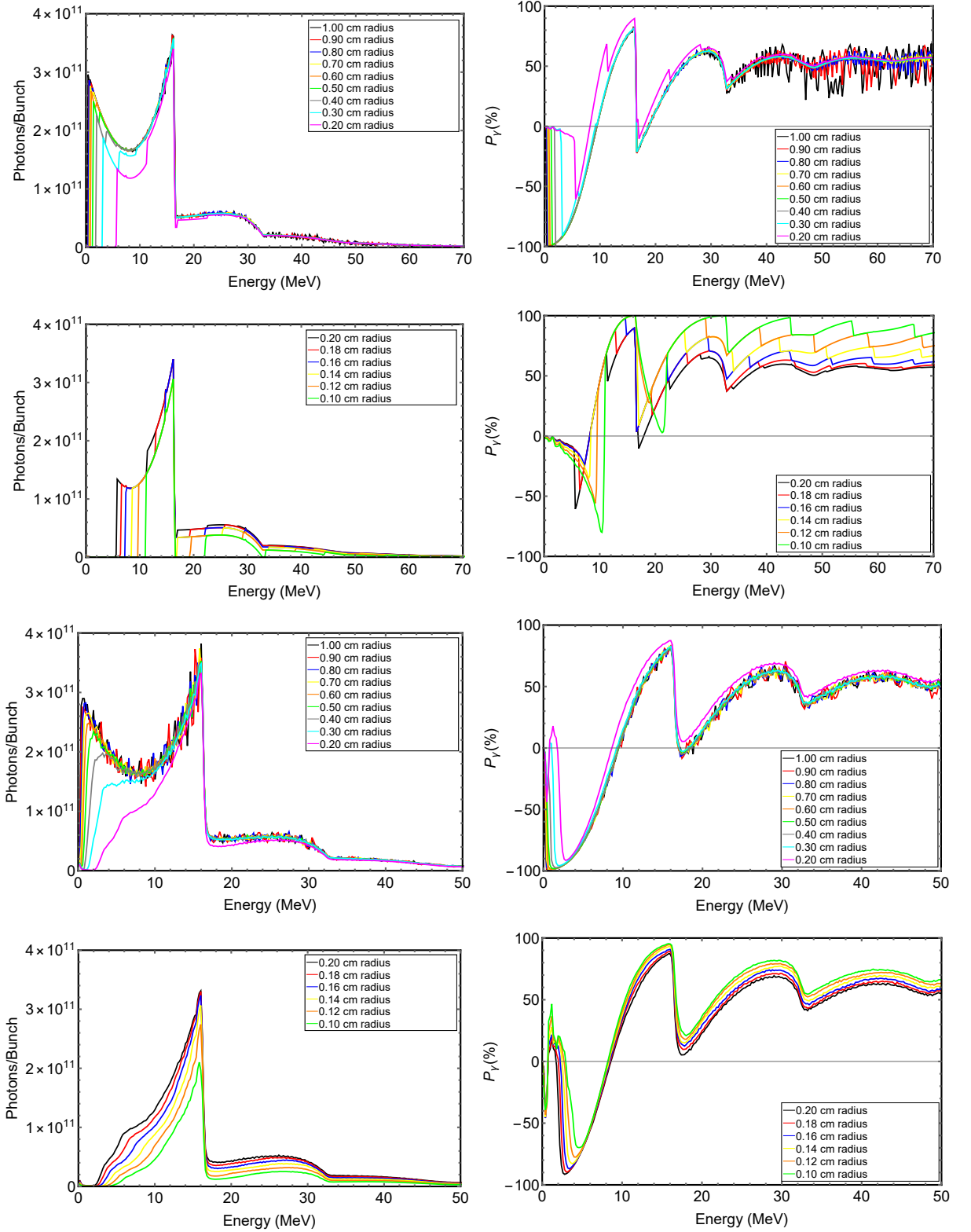


Figure B.2: Ideal (top) and realistic (bottom) spectrum (left) and circular polarization (right) of the photon beam produced by the **ILC-350** undulator with $K = 0.75$ at the target plane with different photon collimator apertures. Each colour represents a different photon collimator aperture.

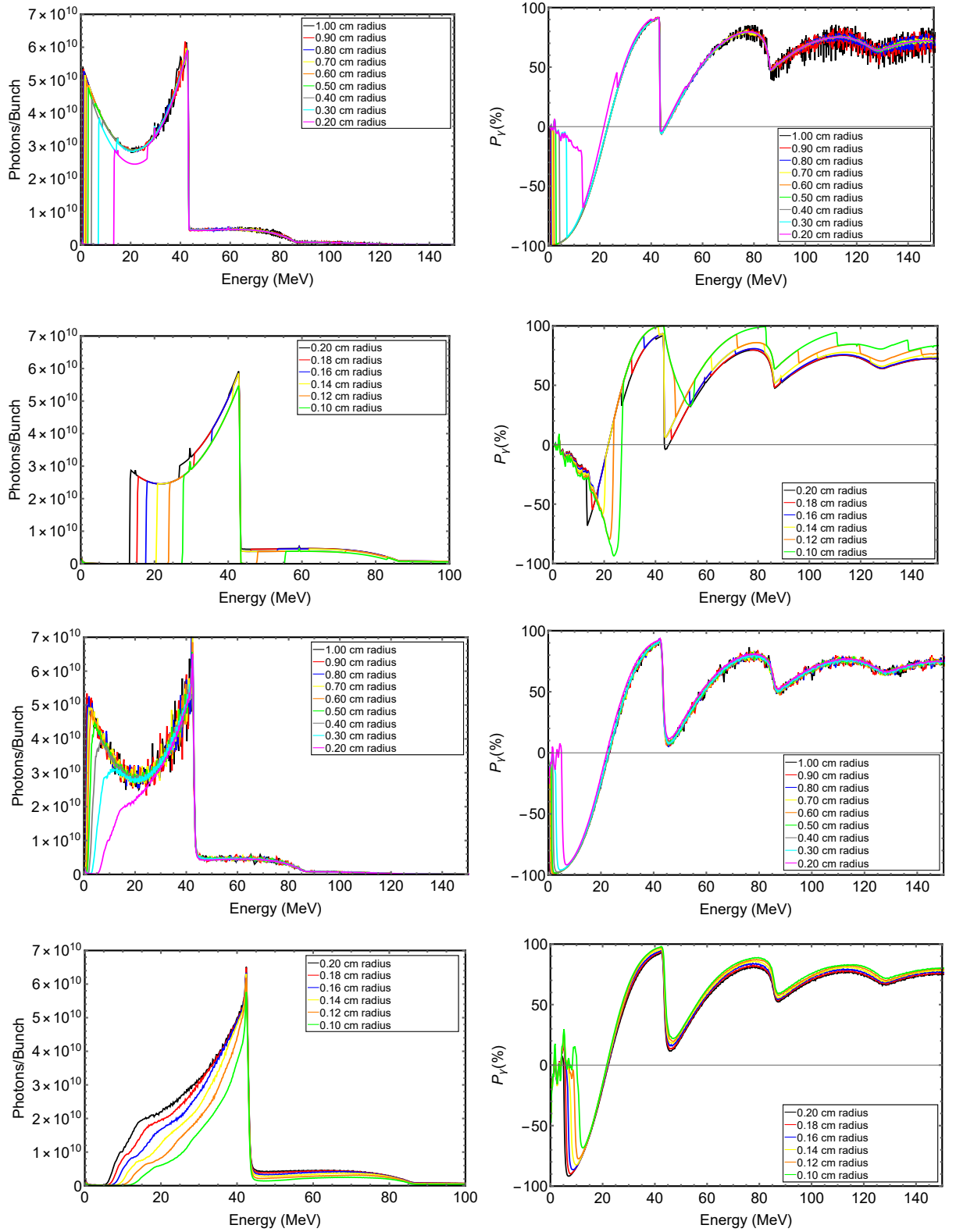


Figure B.3: Ideal (top) and realistic (bottom) spectrum (left) and circular polarization (right) of the photon beam produced by the **ILC-500** with $K = 0.45$ at target plane with different photon collimator apertures. Each colour represents a different photon collimator aperture.

Bibliography

- [1] Moortgat-Pick G, Abe T, Alexander G, Ananthanarayan B, Babich A, Bharadwaj V, et al. Polarized positrons and electrons at the linear collider. *Physics Reports*. 2008;460(4-5):131–243.
- [2] Moortgat-Pick G, Baer H, Battaglia M, Belanger G, Fujii K, Kalinowski J, et al. Physics at the e^+e^- -linear collider. *The European Physical Journal C*. 2015;75(8):371.
- [3] Karl R, List J. Polarimetry at the ILC. arXiv preprint arXiv:170300214. 2017. Available from: <https://arxiv.org/pdf/1703.00214.pdf>.
- [4] Bernardini C. AdA: The first electron-positron collider. *Physics in Perspective*. 2004;6(2):156–183.
- [5] Tigner M. A possible apparatus for electron clashing-beam experiments. *Il Nuovo Cimento* (1955-1965). 1965;37(3):1228–1231.
- [6] Electroweak TS, Groups HF, Collaboration A, Collaboration D, Collaboration L, Collaboration O, et al. Precision electroweak measurements on the Z resonance. *Physics Reports*. 2006;427(5-6):257–454.
- [7] Center SLA. SLAC Linear Collider: Conceptual Design Report. 229. Stanford Linear Accelerator Center, Stanford University; 1980.
- [8] Kulikov A, Ecklund S, Reuter E. SLC positron source pulsed flux concentrator. Stanford Linear Accelerator Center; 1991.
- [9] Phinney N. SLC performance and plans. In: *AIP Conference Proceedings*. vol. 272. American Institute of Physics; 1992. p. 1971–1978.
- [10] Group CS, et al. CEPC Conceptual Design Report: Volume 2-Physics & Detector. arXiv preprint arXiv:181110545. 2018. Available from: <https://arxiv.org/ftp/arxiv/papers/1811/1811.10545.pdf>.
- [11] Adolphsen C. The International Linear Collider Technical Design Report-Volume 3. II: Accelerator Baseline Design. Argonne National Lab.(ANL), Argonne, IL (United States); Thomas

- Jefferson ...; 2013. Available from: <https://arxiv.org/ftp/arxiv/papers/1306/1306.6328.pdf>.
- [12] Yokoya K, Kubo K, Okugi T. Operation of ILC250 at the Z-pole. arXiv preprint arXiv:190808212. 2019. Available from: <https://arxiv.org/pdf/1908.08212.pdf>.
- [13] Bambade P, Barklow T, Behnke T, Berggren M, Brau J, Burrows P, et al. The international linear collider: a global project. arXiv preprint arXiv:190301629. 2019. Available from: <https://arxiv.org/pdf/1903.01629.pdf>.
- [14] Chatrchyan S, Khachatryan V, Sirunyan A, Tumasyan A, Adam W, Bergauer T, et al. Observation of a new boson with mass near 125 GeV in pp collisions at $\sqrt{s} = 7$ and 8 TeV. *Journal of High Energy Physics*. 2013;2013(6):81.
- [15] Behnke T, Brau JE, Foster B, Fuster J, Harrison M, Paterson JM, et al. The international linear collider technical design report-volume 1: Executive summary. arXiv preprint arXiv:13066327. 2013. Available from: <https://arxiv.org/ftp/arxiv/papers/1306/1306.6327.pdf>.
- [16] CLIC T, Charles T, Giansiracusa P, Lucas T, Rassool R, Volpi M, et al. The compact linear collider (cllc)-2018 summary report. arXiv preprint arXiv:181206018. 2018. Available from: <https://arxiv.org/pdf/1812.06018.pdf>.
- [17] Brunner O, Burrows P, Calatroni S, Catalan N, Corsini R, d'Auria G, et al. The CLIC project. arXiv preprint arXiv:220309186. 2022. Available from: <https://arxiv.org/pdf/2203.09186.pdf>.
- [18] Blondel A, Janot P, Tehrani NA, Azzi P, Azzurri P, Bacchetta N, et al. FCC-ee: Your Questions Answered. arXiv preprint arXiv:190602693. 2019. Available from: <https://arxiv.org/pdf/1906.02693.pdf>.
- [19] collaboration F, et al. FCC-ee: The Lepton Collider: Future Circular Collider Conceptual Design Report Volume 2. *European Physical Journal: Special Topics*. 2019;228(2):261–623.
- [20] Zimmermann F, Benedikt M, Burkhardt H, Cerutti F, Ferrari A, Gutleber J, et al. FCC-ee Overview. *Proc HF*. 2014:6–15.
- [21] Hubbell J, Seltzer SM. Cross section data for electron–positron pair production by photons: a status report. *Nuclear Instruments and Methods in Physics Research Section B: Beam Interactions with Materials and Atoms*. 2004;213:1–9.
- [22] NIST. XCOM. Available from: <https://physics.nist.gov/PhysRefData/Xcom/html/xcom1.html>.

- [23] Olsen H, Maximon L. Photon and electron polarization in high-energy bremsstrahlung and pair production with screening. *Physical Review*. 1959;114(3):887.
- [24] Alexander G, Barley J, Batygin Y, Berridge S, Bharadwaj V, Bower G, et al. Undulator-based production of polarized positrons. *Nuclear Instruments and Methods in Physics Research Section A: Accelerators, Spectrometers, Detectors and Associated Equipment*. 2009;610(2):451–487. Available from: <https://arxiv.org/abs/0905.3066v1>.
- [25] V E Balakin AAM. The Conversion system for obtaining high polarized electrons and positrons. Preprint. 1979;460(4-5):79–85.
- [26] DESY. Storage rings as synchrotron radiation sources; 2022. Available from: https://photon-science.desy.de/research/students__teaching/primers/storage_rings__beamlines/index_eng.html.
- [27] Scott DJ. An Investigation into the Design of the Helical Undulator for the International Linear Collider Positron Source. University of Liverpool; 2008.
- [28] Mikhailichenko AA. Optimized parameters of the Helical Undulator for test at SLAC. In: LC02, Proceedings, SLAC-WP-21; 2002. .
- [29] Flöttmann K. Investigations toward the development of polarized and unpolarized high intensity positron sources for linear colliders. vol. 93-161. DESY; 1993.
- [30] K Yokoya (ed) PWGWGea. Report on the ILC Positron Source; 2018.
- [31] Riemann S, Sievers P, Moortgat-Pick G, Ushakov A. Updated status of the undulator-based ILC positron source. arXiv preprint arXiv:200210919. 2020. Available from: <https://arxiv.org/pdf/2002.10919.pdf>.
- [32] Ushakov A, Moortgat-Pick G, Riemann S. Radiation at Photon Dump of Undulator-Based e^+ Source; 2016. Available from: <https://agenda.linearcollider.org/event/7014/contributions/34633/attachments/29960/44797/Ushakov-PhotonDump-ECFALC16.pdf>.
- [33] Morikawa Y. A Photon Dump Study for ILC Undulator Positron Source; October, 2017. Available from: <https://agenda.linearcollider.org/event/7645/contributions/40016/attachments/32407/49219/LCWS2017-ilcphotondump.pdf>.
- [34] Malysheva L, Adeyemi O, Hartin A, Kovalenko V, List B, Moortgat-Pick G, et al. Design of Pre-Dumping Ring Spin Rotator with a Possibility of Helicity Switching for Polarized Positrons at the ILC. arXiv preprint arXiv:160209050. 2016. Available from: <https://arxiv.org/pdf/1602.09050.pdf>.

- [35] Scott D, Clarke J, Baynham D, Bayliss V, Bradshaw T, Burton G, et al. Demonstration of a high-field short-period superconducting helical undulator suitable for future TeV-scale linear collider positron sources. *Physical review letters*. 2011;107(17):174803.
- [36] Bailey I, Clarke J, Scott D, Brown C, Gronberg J, Hagler L, et al. Eddy current studies from the undulator-based positron source target wheel prototype. In: *The 1st International Particle Accelerator Conference*; 2010. p. 4125–4127.
- [37] Seimiya Y, Kuriki M, Takahashi T, Omori T, Okugi T, Satoh M, et al. Positron capture simulation for the ILC electron-driven positron source. *Progress of Theoretical and Experimental Physics*. 2015;2015(10):103G01.
- [38] Kuriki M, S K, Liptak Z, Takahashi T, Omori T, Urakawa J, et al. System integration of ILC E-Driven Positron Source. ILCX21. 2021. Available from: https://agenda.linearcollider.org/event/9211/contributions/49423/attachments/37472/58698/ILCX_MKv1.2.pdf.
- [39] Moortgat-Pick G, et al. The role of polarized positrons and electrons in revealing fundamental interactions at the linear collider. *Phys Rept*. 2008;460:131–243.
- [40] Omori T, Aoki T, Dobashi K, Hirose T, Kurihara Y, Okugi T, et al. Design of a polarized positron source for linear colliders. *Nuclear Instruments and Methods in Physics Research Section A: Accelerators, Spectrometers, Detectors and Associated Equipment*. 2003;500(1-3):232–252.
- [41] Jackson J. *Classical Electrodynamics*, 3rdWiley. New York. 1999.
- [42] Elder F, Gurewitsch A, Langmuir R, Pollock H. Radiation from electrons in a synchrotron. *Physical Review*. 1947;71(11):829.
- [43] Clarke J, Bailey I, Baynham E, Bharadwaj V, Bradshaw T, Brummitt A. The design of the positron source for the International Linear Collider. In: *proceedings of EPAC08*; 2008. Available from: <https://accelconf.web.cern.ch/e08/papers/WE0BG03.pdf>.
- [44] Jackson J. *Classical Electrodynamics Eq.(14.67)*. John Wiley and Sons, New York; 1965.
- [45] Kincaid BM. A short-period helical wiggler as an improved source of synchrotron radiation. *Journal of Applied Physics*. 1977;48(7):2684–2691.
- [46] K Y. Power Distribution on Masks in Undulator Section;. Talk given at Positron Working Group, 2017.6.15. Available from: <https://agenda.linearcollider.org/event/7654/contributions/39096/attachments/31632/47661/PowerDistributionOnMasks.pdf>.
- [47] Tanaka T, Kitamura H. SPECTRA: a synchrotron radiation calculation code. *Journal of synchrotron radiation*. 2001;8(6):1221–1228.

- [48] Newton D, Wolski A. Fast, accurate calculation of dynamical maps from magnetic field data using generalised gradients. Proc PAC09. 2009. Available from: <https://accelconf.web.cern.ch/PAC2009/papers/th6pfp099.pdf>.
- [49] Newton D, et al. The rapid calculation of synchrotron radiation output from long undulator systems. Proceedings of IPAC2010, Kyoto, Japan. 2010. Available from: <https://accelconf.web.cern.ch/IPAC10/papers/wepd045.pdf>.
- [50] Newton D, et al. Modeling synchrotron radiation from realistic and ideal long undulator systems. Proceedings of IPAC2010, Kyoto, Japan. 2010. Available from: <https://accelconf.web.cern.ch/IPAC10/papers/wepd044.pdf>.
- [51] Jenkins M. Novel designs for undulator based positron sources. Lancaster University (United Kingdom); 2015.
- [52] Alrashdi A. Studies in positron and gamma ray production for future facilities. Lancaster University (United Kingdom); 2015.
- [53] Venturini M, Dragt AJ. Accurate computation of transfer maps from magnetic field data. Nuclear Instruments and Methods in Physics Research Section A: Accelerators, Spectrometers, Detectors and Associated Equipment. 1999;427(1-2):387–392.
- [54] Liu W, Gai W, Borland M, Xiao A, Kim KJ, Sheppard J. Emittance Evolution of the Drive Electron beam in a Helical Undulator for the ILC Positron Source. Proceedings of PAC09, Vancouver, BC, Canada. 2009. Available from: <https://accelconf.web.cern.ch/pac2009/papers/we6pfp068.pdf>.
- [55] Toshiyuki OKUGI. Effect to the Positron Generation Yield of Daresbury SC Helical Undulator Integrated Field Error;. Talk at Positron Source Meeting, 17 March 2018.
- [56] Malyshev O, Scott D, Bailey I, Barber D, Baynham E, Bradshaw T, et al. Vacuum Systems for the ILC helical undulator. Journal of Vacuum Science & Technology A: Vacuum, Surfaces, and Films. 2007;25(4):791–801.
- [57] Bungau A, Bailey I, Baynham E, Bradshaw T, Brummitt A, Carr F, et al. Design of the Photon Collimators for the ILC Positron Helical Undulator. EUROTeV-Report-2008-047. 2008. Available from: <https://citeseerx.ist.psu.edu/document?repid=rep1&type=pdf&doi=b7d73f6579c3cb395f538fb035fb4954715ea835>.
- [58] Fasso A, Ferrari A, Ranft J, Sala PR. FLUKA: a multi-particle transport code. CERN-2005-10; 2005.
- [59] Sievers P. Elastic stress waves in matter due to rapid heating by an intense high-energy particle beam. SIS-74-3629; 1974.

- [60] Timoshenko SJG. Theory of elasticity. New York: McGraw-Hill; 1970.
- [61] Science AM. An Introduction to Iron; July, 2023. Available from: <https://www.azom.com/properties.aspx?ArticleID=619>.
- [62] Science AM. An Introduction to Copper; July, 2023. Available from: <https://www.azom.com/properties.aspx?ArticleID=597>.
- [63] Science AM. Tungsten; July, 2023. Available from: <https://www.azom.com/properties.aspx?ArticleID=614>.
- [64] Staufenbiel F, Adeyemi O, Kovalenko V, Moortgat-Pick G, Riemann S, Ushakov A. SIMULATION OF STRESS IN POSITRON TARGETS FOR FUTURE LINEAR COLLIDERS. target. 2013;80(3). Available from: <https://epaper.kek.jp/IPAC2013/papers/tupme006.pdf>.
- [65] Motz J, Olsen HA, Koch H. Pair production by photons. Reviews of Modern Physics. 1969;41(4):581.
- [66] Mikhailichenko A. Collimator for ILC. In: proceedings of EPAC. vol. 6; 2006. Available from: <https://accelconf.web.cern.ch/e06/PAPERS/MOPLS105.PDF>.
- [67] Riemann S, Staufenbiel F, Moortgat-Pick G, Ushakov A. Photon collimator system for the ILC Positron Source. arXiv preprint arXiv:1412.2498. 2014. Available from: <https://arxiv.org/pdf/1412.2498.pdf>.
- [68] Mikhailichenko AA. Use of Undulators at High Energy to Produce Polarized Positrons and Electrons. In: Workshop on new Kinds of Positron sources for Linear Colliders, SLAC; 1997. p. 229–284.
- [69] Liu W, Riemann S, Ushakov A. On the polarization upgrade of ILC undulator-based positron source. In: Proceedings of the 3rd International Particle Accelerator Conference, New Orleans, USA; 2012. p. 20–25. Available from: <https://accelconf.web.cern.ch/IPAC2012/papers/tuppr042.pdf>.
- [70] Walker N. ILC possibilities at Z and W. priv note March. 2016;15. Available from: https://agenda.linearcollider.org/event/7003/attachments/28438/42918/ILC_possibilities_at_Z_and_W.pdf.
- [71] Tanabashi M, Hagiwara K, Hikasa K, Nakamura K, Sumino Y, Takahashi F, et al. Review of particle physics. Physical Review D. 2018;98(3):030001.
- [72] Berger M, Coursey J, Zucker M. ESTAR: Computer Programs for Calculating Stopping-Power and Range Tables for Electrons. National institute of standards and technology (nist);.

- [73] Leo WR. Techniques for nuclear and particle physics experiments: a how-to approach. Springer Science & Business Media; 2012.
- [74] Podgorsak EB, et al. Radiation physics for medical physicists. vol. 1. Springer; 2006.
- [75] McMaster WH. Matrix representation of polarization. Reviews of modern physics. 1961;33(1):8.
- [76] Schalicke A. Polarised Positrons for the ILC. arXiv preprint arXiv:07122340. 2007. Available from: <https://arxiv.org/pdf/0712.2340.pdf>.

Acronyms

ILC	International Linear Collider.	FCC-hh	Proton-Proton collision.
CLIC	Compact Linear Collider.	FCC-ee	Electron-Positron collision.
LHC	Large Hadron Collider.	CEPC	Chinese Circular Electron Positron Collider.
LEP	Large Electron-Positron Collider.	E-driven	Electron driven source.
SLC	Stanford Linear Collider.	TDR	Technical Design Report.
SLAC	Stanford Linear Accelerator Center.	LHeC	Proton-Electron collider.
AdA	Anello di Accumulazione collider.	FCC-he	Proton-Electron collider.
LNF	Frascati National Laboratory.	HUSR code	Helical Undulator Synchrotron Radiation code.
linac	Linear Accelerator.	FluxCalc	A mathematica notebook code.
SR	Synchrotron Radiation.	SPECTRA	A code to simulate the SR spectrum.
FCC	Future Circular Collider.	OMD	Optical Matching Device.
DR	Damping Ring.		

Variables

Collider parameters

N_e	Number of electrons per bunch.
n_b	Number of bunches per pulse.
Δt_b	Bunch separation.
f_{rep}	Pulse repetition rate.
I_{beam}	Beam current.
σ_z	RMS Bunch length.
σ_x (σ_y)	RMS Horizontal (vertical) beam size at IP.
E_e	Electron beam energy.
P_- (P_+)	Electron (Positron) beam polarization.
L	Luminosity.

Material properties

ρ	Density of a material.
λ	Thermal Conductivity.
Y_m	Young's modulus of a material.
α_h	Thermal expansion coefficient.
F_{tu}	Tensile strength of a material.
n_{atom}	Number of atoms per unit volume.
σ_{pair}	Cross section of the pair production process.
H_m	Heat distributes over a distance.
σ_{max}	Maximum instantaneous stress.
C_p	Heat Capacity.

Other parameters

q	Electron charge.
m_o	Rest mass of the particle.
E_0	Electron rest energy.
f	Frequency of the emitted light at rest.
β	Relative velocity of electron.

Undulator variables

B_o	Undulator B-field.
λ_u	Undulator period.
$\sigma_B(z)$	Errors in the undulator B-field.
$\sigma_\lambda(z)$	Error in the undulator period.
K	Undulator deflection parameter.
d_u	Undulator aperture.
E_{loss}	Electron energy loss in undulator.
L_u	Total active undulator length.
X_0	Radiation length.
γ	Photon.
θ_{Max}	Maximum opening angle included in the study.
N	Number of the undulator periods.
$J_n(x)$	Bessel function.
n	Harmonic number of the photon spectrum.
ω_0	Circular frequency of the electron's helical orbit.
ω	Radiation frequency.
P_3	Circular polarization rate.
N_γ	Photon number.
E_{ave}^γ	Average energy of photon beam.
P_γ	Polarization of the photon beam at the target.
N_l	Number of left handed circular polarized photons.
N_r	Number of right handed circular polarized photons.
L_m	Distance between photon masks.
d_m	Inner diameter of the photon mask.
d_u	Inner diameter of the undulator.
P_{mask}	Deposited power at a mask.
N_{mask}^γ	Incident photon number at a mask.
ΔT_{max}	Maximum temperature rise at a mask.
P_{stop}^{mask}	Power stopped by a mask.
E_{max}	Maximum deposited energy (GeV/cm ³ /photon) along a mask.
PEDD	Peak Energy Deposition Density at a mask.
L_{mask}	Mask length.
r_o	Outer radius of the mask.
r_i	Inner radius of the mask.
P_{wall}	Total deposited power per meter into the undulator wall.
P_{target}	Power of the photon beam at the target.
E_{1st}	Energy cutoff of the first harmonic of the photon spectrum.
U	Energy radiated per unit angular frequency (ω) per unit solid angle (Ω) emitted by one relativistic charged particle in a magnetic field.
$\frac{dW}{d\Omega}$	Angular power distribution produced by a helical undulator calculated by integrating equation 5.26 over all frequencies.

Acknowledgments

First, and most importantly, thanks to my parents, who have continually supported me throughout my life and instilled in me a life long love of learning from primary school up to now. I would also like to give special thanks to my wife, Shuruq, for her continuous support and understanding when undertaking my research and writing my PhD project. None of this would have been possible without them.

Thanks to my children, my daughter, Alanoud, my son, Abdulaziz, and my little daughter, Albatul. I know how the time was difficult for you all for missing me most of the time. Thanks my children!

Thanks to my brothers, sisters and friends for their support and constant encouragement. To my maternal uncle, Muhammad, who passed away recently, I will never forget your support and constant encouragement since I was a child. Thanks Dear Muhammad D Alharbi!

There are many other people who have helped me over the years I have been studying for this PhD and deserve mention. First, thanks to Prof. Dr. Gudrid Moortgat-Pick who kindly gave me the opportunity to do my PhD work in Hamburg University and allow me to join her research group and provided helpful advice at all times. Massive thanks Prof. Dr. Gudrid!

However, there is no word that can describe my gratitude to Dr. Sabine Riemann. I must record my enormous thanks for her here, for her supervision, advice, and guidance from the very early stage of this research. I thank her continuous support over the years. Many thanks for her remarks on several draft of this thesis which were beneficial. Her professional explanations were there since my first step in my PhD project. Dr. Sabine Riemann was more than just a best supervisor, she was a friend and a mentor. It has been a honor to be one of her PhD student. Thanks Dr. Sabine!

Special thanks to Dr. Ayash Alrashdi and his good wishes and continuous support before I started the PhD research and up to now. Thanks to him for giving me the access to use HUSR software and his help with setting up this powerful tool in the early stage of this work. Thanks Dr. Ayash!

I am extremely grateful to Dr. Andriy Ushakov for his priceless assistance in the simulation part in FLUKA. Thanks to all members of the ILC positron source group, especially, Peter Sievers, Kaoru Yokoya, Masao Kuriki. Toshiyuki Okugi. I


Finally, thanks for King Abdulaziz City for Science and Technology (KACST) for giving me the chance and supported me financially to do my PhD.

Eidesstattliche Erklärung / Declaration on oath

Hiermit versichere ich an Eides statt, die vorliegende Dissertation selbst verfasst und keine anderen als die angegebenen Hilfsmittel und Quellen genutzt zu haben. Die eingereichte schriftliche Fassung entspricht der auf dem elektronischen Speichermedium. Die Dissertation wurde in der vorgelegten oder einer ähnlichen Form nicht schon einmal in einem früheren Promotionsverfahren eingereicht.

I hereby affirm, that I wrote the present dissertation myself and that I have not used any other sources than those given. The written version submitted corresponds to that on the electronic storage medium. The dissertation was not submitted in the present or in a similar form in an earlier doctoral procedure.

Hamburg, den 15. Nov, 2023


Khaled Snad R Alharbi
15.11.2023